Andreas Lesch, BSc

Quantification of T_1, T_2 and Pseudo Spin Density ρ_0 using bSSFP with Correction for Non-Ideal Flip Angle Profiles

Master's Thesis

Institute for Medical Engineering
Graz University of Technology
Kronesgasse 5, A - 8010 Graz
Head: Univ.-Prof. Dipl.-Ing. Dr.techn. Rudolf Stollberger

Supervisor:
Dipl.-Ing. Andreas Petrovic

Evaluator:
Univ.-Prof. Dipl.-Ing. Dr.techn. Rudolf Stollberger

Graz, April 2014

EIDESSTATTLICHE ERKLÄRUNG

Ich erkläre an Eides statt, dass ich die vorliegende Arbeit selbstständig verfasst, andere als die angegebenen Quellen/Hilfsmittel nicht benutzt und die den benutzten Quellen wörtlich und inhaltlich entnommenen Stellen als solche kenntlich gemacht habe.

Graz, am ....
Name

STATUTORY DECLARATION

I declare that I have authored this thesis independently, that I have not used other than the declared sources/resources and that I have explicitly marked all material which has been quoted either literally or by content from the used sources.

....
date Name

Abstract

The quantification of T_1 (longitudinal relaxation time) and T_2 (transverse relaxation time) has become an important issue in the field of MRI during the last decades in many clinical and scientific applications. Conventional methods for relaxometry suffer from very long acquisition times in the order of several hours. A very promising approach to quantify both relaxation parameters and the pseudo spin density ρ_0 by sampling the transient of an IR-bSSFP sequence was shown in previous works. The RF-pulses used in slice selective bSSFP sequences are usually very short, which results in rather non-ideal flip angle profiles far away from the desired rectangular shape. Hence, the quantification accuracy, especially of T_2, is altered significantly by these non-ideal profiles. The aim of this work was to investigate the influence of non-ideal flip angle profiles on the quantification accuracy and to implement an algorithm which is able to correct the flip angle profile effects. Further, this algorithm should be included in an existing framework to perform the quantification of under-sampled data.

For this purpose the real slice profile of the exciting RF-pulse had to be determined. This was done by simulations according to the Bloch-equations and by measurements inside a phantom. A forward model was established, based on rotation and relaxation matrices as a result of the Bloch-equations, which models the magnetization vector recursively over one period of TR. Two correction algorithms were implemented, one performs pixel wise quantification based on already reconstructed images, and the second algorithm performs the quantification of k-space data, which is also known as the model-based nonlinear inverse reconstruction. This approach is able to reconstruct under-sampled data.

The algorithms were tested on simulated data, on measured data inside a phantom and on in vivo measurements inside the human brain of healthy volunteers. The results achieved on simulated data and on phantom measurements are very promising. The quantification error, which is most dominant in T_2, could be significantly reduced. However these promising results could not be reproduced for the in vivo measurements. It turned out that the reasons for that are on-resonant magnetization transfer effects. Further investigations are necessary to prove if it is possible to either correct these effects or to gain more information about the magnetization transfer out of the transient time decay.

Keywords: relaxometry; bSSFP; slice profile correction; under-sampling, on-resonant magnetization transfer

Zusammenfassung

Die Quantifizierung der Relaxationsparameter T_1 (longitudinale Relaxationszeit) und T_2 (transversale Relaxationszeit) hat sich zu einem sehr wichtigen Thema in der Quantitativen MR-Bildgebung für diverse klinische und wissenschaftliche Anwendungen entwickelt. Konventionelle Relaxometrieverfahren haben den Nachteil einer extrem langen Aufnahmezeit im Bereich von Stunden. Ein sehr vielversprechender Ansatz um beide Relaxationsparameter und die Pseudo-Spindichte ρ_0 über die Messung der Transiente einer IR-bSSFP Sequenz wurde in vorangegangenen Arbeiten vorgestellt. Üblicherweise sind die HF-Impulse die zur schichtselektiven Anregung in bSSFP Sequenzen verwendet werden sehr kurz, was zu hochgradig nicht idealen Kippwinkelprofilen weit entfernt von der gewünschten rechteckigen Form führt. Die Genauigkeit der Quantifizierung wird jedoch sehr stark von der Form des Kippwinkelprofiles beeinflusst, der Fehler geht am stärksten in T_2 ein. Ziel dieser Arbeit war es nun den Einfluss von nicht idealen Schichtprofilen auf die Quantifizierung zu untersuchen und einen Algorithmus zu Korrektur dieser Einflüsse zu implementieren. Dieser Algorithmus sollte in weiterer Folge in ein bestehendes Framework integriert werden um eine Quantifizierung auf Basis unterabgetasteter Daten zu ermöglichen.

Für diesen Zweck mussten die tatsächlichen Schichtprofile des anregenden HF-Pulses bestimmt werden. Dazu wurden Simulationen basierend auf den Bloch Gleichungen und eine Messung in einem Phantom herangezogen. Es wurde ein Vorwärtsmodell basierend auf Rotations- und Relaxationsmatrizen als Lösung der Bloch Gleichungen aufgestellt, dass den Magnetisierungsvektor rekursive über eine TR Periode modelliert. Zwei Korrekturalgorithmen wurden implementiert. Der erste nimmt die Quantifizierung Pixelweise auf Basis bereits rekonstruierter Bilder vor, wohingegen der andere die Quantifizierung auf Basis von Rohdaten (k-Raum Daten) vornimmt (Modell-basierte nichtlineare inverse Rekonstruktion) und dadurch auch unterabgetastete Messdaten rekonstruiert werden können.

Die Algorithmen wurden anhand simulierter Messdaten, Phantommessungen und in vivo Messungen im Gehirn von gesunden Probanden getestet. Die Ergebnisse aus den simulierten Daten, sowie jene aus den Phantommessungen konnten eine signifikante Verbesserung des Messfehlers, welcher sich am stärksten in T_2 niederschlägt, zeigen. Diese vielversprechenden Ergebnisse konnten jedoch in vivo nicht reproduziert werden. Es hat sich herausgestellt, dass on-resonante Magnetisierungstransfer Effekte der Grund dafür sind. Weitere Untersuchungen sind notwendig, um zu prüfen ob diese Effekte ebenfalls korrigiert werden können, oder ob es möglich ist auch Magnetisierungstransfer Parameter aus dem Verlauf der Transiente zu quantifizieren.

Schlüsselwörter: Relaxometrie; bSSFP; Schichtprofilkorrektur; Unterabtastung; on-resonanter Magnetisierungstransfer

Acknowledgment

First of all I would like to thank my both supervisors Prof. Rudolf Stollberger and Dipl.-Ing. Andreas Petrovic for their support and many hours of inspiring discussion.

Furthermore I would like to thank my colleagues at the Institute Dr. Markus Kraiger, Dipl.-Ing. Peter Opriessnig, Dipl.-Ing. Christoph Aigner, Dipl.-Ing. Johannes Strasser, Dipl.-Ing. Clemens Diwoky and Dipl.-Phys. Matthias Schlögl for their help and many hours of interesting discussions.

I also would like to thank Prof. Christian Clason for the contribution of some mathematical background to the solution of this problem.

My gratitude is also to Dipl.-Ing. Lukas Pirpamer for his help and expertise concerning magnetization transfer.

My thanks go also to our radiology technology assistants Alexandra Lipfert and Thomas Zussner for their support concerning the practical measurements on the scanner.

Last but not least I would like to thank my parents Anna and Walter Lesch, without their support during the last couple of years it would not have been possible to finish my studies.

Contents

List of Abbreviations

ADC	analog to digital converter
B_0-field	static magnetic field of the MR-Scanner
B_1-field	RF-field of the MR-Scanner
bSSFP	balanced steady-state free precession
CG	conjugated gradients
CPU	central processing unit
CSF	cerebrospinal fluid
CUDA	compute unified device architecture
DAM	double angle method
DESPOT1	driven equilibrium single pulse observation of T_1
DESPOT2	driven equilibrium single pulse observation of T_2
DICOM	digital imaging and communications in medicine
ECG	electrocardiogram
FA	flip angle
FFE	fast field echo
FID	free induction decay
FIESTA	fast imaging employing steady state acquisition
FLASH	fast low angle shot
FOV	field of view
Gd	gadolinium
Gd-conc.	gadolinium concentration
GM	gray matter in brain
GPU	graphics processing unit
GRAPPA	generalized auto-calibrating partially parallel acquisition
GRE	gradient echo
IR	inversion recovery
IR-SE	inversion recovery spin-echo
MOLLI	modified Look-Locker inversion recovery
MR	magnetic resonance
MRI	magnetic resonance imaging
MSE	multi echo spin-echo
MT	magnetization transfer
ODE	ordinary differential equation
OpenCL	Open Computing Language
Quant. Res.	quantification results
RF	radio frequency

ROI	region of interest
SAR	specific absorption rate
SE	spin echo
SNR	signal to noise ratio
SPGR	spoiled gradient recalled-echo
SR	saturation recovery
T_1	longitudinal relaxation time
T_2	transverse relaxation time
TE	echo time
TI	inversion time
TR	repetition time
TrueFISP	true fast imaging with steady state free precession
TrueFISP_CV .	Siemens TrueFISP sequence for cardiovascular imaging
TSE	turbo spin echo
VNr.	volunteer number
WM	white matter in brain

List of Variables

α	flip angle	$^\circ$
α_j	flip angle for j^{th} excitation pulse	$^\circ$
$\alpha_{j,k}$	flip angle for j^{th} excitation at sub-slice position k	$^\circ$
α_{max}	flip angle with the highest steady state signal	$^\circ$
α_{nom}	nominal flip angle	$^\circ$
α_{true}	true flip angle due to B_1 inhomogeneity	$^\circ$
$\alpha(z)$	flip angle profile	$^\circ$
γ	gyromagnetic constant	$\frac{MHz}{T}$
δ	under-sampling factor	
$\Delta\omega$	angular precession frequency in the rotating frame	$\frac{rad}{s}$
$\Delta\omega_z$	angular precession frequency offset due to gradient field	$\frac{rad}{s}$
ΔB_0	static field inhomogeneities	T
Δf	off-resonance frequency	Hz
ΔS_{MT}	attenuation coefficient due to MT	
$\Delta S_{MT_{GM}}$	attenuation coefficient due to MT in GM	
$\Delta S_{MT_{WM}}$	attenuation coefficient due to MT in WM	
ΔS_{tissue}	factor comparing attenuation in GM and WM	
Δt	time between inversion and first readout	ms
Δz	discrete element in z-direction	m
ϵ	quantification error	%
Θ	precession angle around the direction of the effective field	$^\circ$
λ	eigenvalues of the transition matrix	
λ_1	positive eigenvalue of the transition matrix	
ρ_0	pseudo spin density	$a.u.$
ϕ	acquired off-resonance precession angle during one TR period	$^\circ$
φ	angle of B_e to the x-axis for off-resonant excitation	$^\circ$
ω	angular frequency of RF-field/rotating coordinate system	$\frac{rad}{s}$
ω_0	angular precession frequency of the spins (Larmor frequency)	$\frac{rad}{s}$
ω_1	angular precession frequency due to B_1	$\frac{rad}{s}$
A	parameter for the Schmitt-approach	
$\mathbf{A}(\vec{T})$	complete implicit function transformation matrix	$a.u.$
$\mathbf{A}_j(\vec{T})$	implicit function transformation matrix at excitation j	$a.u.$
B	parameter for the Schmitt-approach	
B_0	static magnetic field of the MR-Scanner	T

B_1	RF-field of the MR-Scanner	mT
$\vec{B}_e$	effective magnetic field in the rotating frame	T
$\vec{B}_{ext}$	external magnetic field	T
c	coil index	
c_{ap}	apparatus constant relating M_t and S_{meas}	$a.u.$
$\mathbf{C}$	factor considering sign-alternation at the readout	
$\mathbf{C}_c$	coil sensitivity of coil c	
$\vec{d}(\vec{T})$	complete implicit transformation vector	$a.u.$
$\vec{d}_j(\vec{T})$	implicit function transformation vector at excitation j	$a.u.$
$\mathbf{D}(t)$	exchange matrix between bound and restricted pool	
$\vec{e}_z$	unit vector in z-direction	
$\vec{e}_{Tx}$	relaxation vector concerning longitudinal relaxation for time Tx	
E_1	decay rate for longitudinal relaxation	
E_1^*	decay rate for bSSFP transient	
E_2	decay rate for transverse relaxation	
$\mathbf{E}_{Tx}$	relaxation matrix for time Tx	
f_α	factor considering flip angle variation due to B_1 inhomogeneity	
f_{inv}	factor considering inversion imperfections	
F	bound pool fraction	%
$\vec{F}(\vec{T},\vec{M})$	implicit formulation of the complete forward model	
$\vec{F}_j$	implicit formulation of the forward model at excitation j	
$G(\Delta\omega)$	absorption line shape function	s
G_z	gradient of the magnetic field in z-direction	$\frac{T}{m}$
i	imaginary unit	
I_1	image intensity at α	$a.u.$
I_2	image intensity at 2α	$a.u.$
INV	parameter describing dependency of S_{stst} and S_0	
j	time index of the excitation pulses	
J	cost function	$a.u.$
k	index of sub-slice	
k_f	first order transfer rate constant from free to restricted pool	s^{-1}
k_r	first order transfer rate constant from restricted to free pool	s^{-1}
K	number of sub-slices	
K_{recon}	slice profile resolution for reconstruction	
K_{sim}	slice profile resolution to generate simulated data	
m	dimension of the parameter space	
$\vec{M}$	magnetization vector	$a.u.$
$\vec{M}'$	magnetization vector in the rotating frame	$a.u.$
M_0	longitudinal magnetization in thermal equilibrium	$a.u.$
$M_{0,f}$	longitudinal thermal equilibrium magnetization free pool	$a.u.$
$M_{0,r}$	longitudinal thermal equilibrium magnetization restricted pool	$a.u.$
$\vec{M}_0$	initial magnetization vector	$a.u.$
$\vec{M}_0(\vec{x})$	parameter map of M_0 written column-wise into a vector	$a.u.$
$\vec{M}_j$	magnetization vector after j^{th} excitation pulse	$a.u.$
$\vec{M}_{j,k}$	magnetization vector after j^{th} excitation in sub-slice k	$a.u.$
M_{ss}	magnitude of transverse steady state magnetization	$a.u.$
$\vec{M}_t$	transverse magnetization vector	$a.u.$

M_x	x-component of the magnetization vector	$a.u.$
$M_{x'}$	x-component of the magnetization vector in the rotating frame	$a.u.$
$M_{x,f}$	x-component of the magnetization vector in free pool	$a.u.$
$M_{x,j,k}$	x-component of $\vec{M}_{j,k}$	$a.u.$
$M_{x,r}$	x-component of the magnetization vector in restricted pool	$a.u.$
M_y	y-component of the magnetization vector	$a.u.$
$M_{y'}$	y-component of the magnetization vector in the rotating frame	$a.u.$
$M_{y,f}$	y-component of the magnetization vector in free pool	$a.u.$
$M_{y,j,k}$	y-component of $\vec{M}_{j,k}$	$a.u.$
$M_{y,r}$	y-component of the magnetization vector in restricted pool	$a.u.$
$\mathbf{M}_{y,n,k}(\vec{x})$	transverse magnetization in each pixel	$a.u.$
M_z	z-component of the magnetization vector	$a.u.$
$M_{z,f}$	z-component of the magnetization vector in free pool	$a.u.$
$M_{z,j,k}$	z-component of $\vec{M}_{j,k}$	$a.u.$
$M_{z,r}$	z-component of the magnetization vector in restricted pool	$a.u.$
n	index of acquired images after one inversion	
N_{coil}	number of receiver coils	
N_{max}	total number of RF-pulses after one inversion	
N_{phase}	number of acquired images	
N_{ramp}	number of preparation pulses	
N_{seg}	number of k-space lines acquired in each image after one inversion	
N_{TE}	number of echo times	
N_{TI}	number of inversion times	
N_{trig}	number of trigger pulses between two inversions	
$\mathbf{P}$	binary mask of under-sampling scheme	
$\vec{Q}(j)$	transient part of the magnetization	$a.u.$
Q_x	x-component of the transient magnetization	$a.u.$
Q_y	y-component of the transient magnetization	$a.u.$
R	exchange rate constant	$a.u.$
$R_{1,f}$	longitudinal relaxation rate of the free pool	s^{-1}
$R_{1,r}$	longitudinal relaxation rate of the restricted pool	s^{-1}
$R_{RF,f}$	saturation rate of the free pool	s^{-1}
$R_{RF,r}$	saturation rate of the restricted pool	s^{-1}
$\mathbf{R}_x$	rotation matrix around the x-axis	
$\mathbf{R}_x(\alpha, t)$	modified rotation matrix around the x-axis including saturation of the bound pool	
$\mathbf{R}_y$	rotation matrix around the y-axis	
$\mathbf{R}_z$	rotation matrix around the z-axis	
S_0	signal after $\alpha/2$ preparation	$a.u.$
$S(t)$	time response of the signal	$a.u.$
S_{IR}	steady for inversion recovery	$a.u.$
S_{meas}	measured signal	$a.u.$
$S_{meas,ss}$	steady state of measured signal	$a.u.$
$\mathbf{S}_{meas}$	measured under-sampled k-space	$a.u.$
S_{sim}	simulated signal	$a.u.$
$S_{sim,ss}$	steady state of simulated signal	$a.u.$
$\mathbf{S}_{sim}$	forward simulated images	$a.u.$
S_{SR}	signal for saturation recovery	$a.u.$

S_{ss}	steady state signal	$a.u.$
$\vec{T}$	parameter vector	
$\mathbf{T}$	transition matrix between two successive magnetization states	
T_1	longitudinal relaxation time	ms
T_2	transverse relaxation time	ms
$\vec{T}_1(\vec{x})$	parameter map of T_1 written column-wise into a vector	ms
$\vec{T}_2(\vec{x})$	parameter map of T_2 written column-wise into a vector	ms
T_1^*	time constant of bSSFP transient	ms
T_2^*	transverse relaxation time including local inhomogeneities	ms
$T_{1,f}$	longitudinal relaxation time in free pool	ms
$T_{2,f}$	transverse relaxation time in free pool	ms
$T_{1,r}$	longitudinal relaxation time in restricted pool	ms
$T_{2,r}$	transverse relaxation time in restricted pool	ms
$T_{1_{max}}$	longest longitudinal relaxation time expected	ms
$\overline{T}_{1,2_{quant}}$	mean of quantified relaxation time inside a ROI	ms
$\overline{T}_{1,2_{ref}}$	mean of reference relaxation time inside a ROI	ms
TE	echo time	ms
TI	inversion time	ms
TR	repetition time	ms
T_{RF}	duration of the RF-pulse	ms
t	time	ms
t_{acq}	acquisition time	ms
t_{acqMSE}	acquisition time for multi spin echo sequence	ms
t_{acqSE}	acquisition time for spin echo sequence	ms
t_{acq_total}	total acquisition time for all N_{phase} images	ms
t_{prep}	time required for preparation	ms
t_{wait}	waiting time between last readout and the following inversion	ms
u	integration variable for the absorption line	
U_{coil}	voltage applied to the transmit coil	V
$W(\Delta\omega)$	saturation rate of the restricted pool	s^{-1}
W_{ph}	resolution in phase-encoding direction	$pixel$
$\vec{x}$	spatial coordinate in the image plane	$pixel$

1 Introduction

1.1 Background

The quantification of the longitudinal relaxation time T_1 and the transverse relaxation time T_2 has become an important issue in magnetic resonance imaging (MRI). There are many clinical and scientific applications where the quantified relaxation times are important diagnostic parameters for different diseases. For example for the diagnosis of Multiple Sclerosis [1, p. 132] a significant increase in T_1 and T_2 values in white matter (WM) of the brain can be measured. More examples for the diagnostic relevance of relaxometry are intracranial tumors [1, p. 133], epilepsy, stroke or dementia [1, p. 134]. Some other examples for other parts of the body are described in [2].

Another important issue for relaxometry is synthetic MRI [3]. One of the most important features of MRI is the wide range of different adjustable contrasts, depending on the diagnostic question and the examined part of the body. Sometimes it is necessary to acquire images with different contrasts to get the relevant diagnostic information. Since different contrasts require different measurements, the scan time is elongated and the risk of inter scan motion increases, which leads to miss-registered images. As described in [4], it is possible to measure the three important contrast parameters T_1, T_2 and ρ_0 by one single scan. These values are used to generate images with different contrasts synthetically, as it is described in [3]. The main advantages of this technique are the reduced acquisition time which leads to an improved patient comfort as well as perfectly registered images and the possibility of manual contrast adjustment in retrospect by a physician as it is necessary to get the relevant diagnostic information.

Conventional sequences for determining the relaxation parameters are based on spin echo (SE) sequences with different inversion times (TI) or echo times (TE) for T_1 and T_2 quantification, respectively. However, these sequences suffer from very long acquisition times, because as long repetition times (TR) are required to ensure completely relaxed tissue before the next excitation. Despite some acceleration techniques like turbo spin echo (TSE), partial Fourier and parallel imaging methods, conventional relaxometry especially

for T_1 is in most cases not practicable in clinical applications. T_2 can be measured in an acceptable time using a multi spin echo (MSE) sequence, but T_2 is systematically overestimated due to stimulated echos and the quantification error can be up to 30% as shown in [5] and [6]. Nevertheless, SE-based quantification methods are the most accurate way to perform relaxometry and they are used as a reference measure for all other methods to determine their accuracy.

To overcome the problem of slow acquisition, several fast methods for T_1 quantification based on gradient echo sequences (GRE) were proposed during the last decades. As described in [7], a Fast Low Angle Shot (FLASH) sequence and a balanced steady-state free precession (bSSFP) sequence can be used to sample the transient recovery of the longitudinal magnetization after a single inversion pulse to quantify T_1 . In [8], a similar sequence is described to apply T_1 measurement inside the heart. An electrocardiogram (ECG) triggered modified Look-Locker inversion recovery (MOLLI) experiment is used to sample the recovery curve during the heart cycle.
Another method for measuring either T_1 or T_2 called DESPOT1 and DESPOT2 (driven equilibrium single pulse observation of T_1 and T_2 , respectively) is described in [9]. T_1 is determined by using a "series of spoiled gradient recalled-echo (SPGR) images acquired over a range of flip angles with constant repetition time (TR)" [9]. For the calculation of T_2 a series of fully bSSFP sequences with different flip angles is used. The drawback of these previously described methods is that they are typically very sensitive to variations in B_1 and non-ideal slice profiles. Furthermore, it is only possible to determine one parameter per measurement and for the T_2 quantification using DESPOT2 T_1 has to be known.

A promising approach was proposed by Schmitt [4] which uses the transient time response of the transverse magnetization of a bSSFP sequence after an inversion pulse to determine both T_1 and T_2 and the pseudo spin density ρ_0 in a single measurement. ρ_0 is called pseudo spin density, because it is not only proportional to the number of spins in a certain volume, but also to the local coil sensitivity, it is actually no real quantitative measure. Furthermore, it is proportional only to the number of free protons. Referring to [4], the quantification accuracy lies in a very good range of several percent compared to standard reference measurements in phantoms. Also in vivo measurements seem to be very accurate in gray matter (GM) and WM in the brain. The scan time for the acquisition of all three parameter maps in a single slice with a resolution of 252 x 256 pixels is in the range of about 2 minutes, which is very fast compared to conventional methods.
The bSSFP sequence is highly sensitive to off-resonances, which could lead to so called banding artifacts, as described in [10, p. 589-595]. If an off-resonance precession angle

of around 180° is accumulated during one TR interval, the signal decreases significantly. To avoid this effect, the TR of bSSFP sequences is desired to be as low as possible and therefore very short radio frequency (RF)-pulses are used. However, these short RF-pluses suffer from a very bad flip angle profile across the slice, which is far from the desired rectangular shape. It is shown in [11] that a variation of the true flip angle and non-ideal slice profiles have a significant influence on the quantification accuracy of T_1 and T_2. As a correction strategy an extension of the bSSFP acquisition from single slice to 3D is proposed [11]. In contrast to that, in this work we focused on the correction of non-ideal slice profiles during the reconstruction using mathematical methods to increase the quantification accuracy with single slice acquisition, because 3D acquisition suffers from other disadvantages like increased acquisition time, truncation artifacts and Gibbs ringing in slice direction and increased motion sensitivity [10, p. 425–433].
The approach of Schmitt can also be used for ultra-fast T_1 and T_2 quantification. It is shown in [12], that the bSSFP transient response can be sampled after a single inversion pulse and therefore the total acquisition time can be reduced to about 5 seconds. In [13], a similar approach is proposed, which uses a radial readout of the bSSFP sequence and a special echo-sharing based filter method to sample the full transient after one inversion pulse.

1.2 Objective

The objective of this thesis was to investigate the influences of non-ideal flip angle profiles and other parameters like the nominal flip angle, off-resonances, different ratios of T_2/T_1 or different absolute values of T_1 and T_2 with and without noise on the quantification accuracy of T_1 and T_2 using the approach of Schmitt [4].

On Siemens Scanners, there is a bSSFP sequence implemented which is optimized for cardiovascular imaging called TrueFISP_CV sequence. The idea was to use this sequence without any modifications to perform relaxometry. Therefore, it was necessary to develop and implement an algorithm which is able to correct the effects of non-ideal slice profiles. For this purpose, the real slice profile of the used RF-pulse had to be determined by simulations and measurements. The simulated and measured data had to be compared to each other. The quantification accuracy of the slice profile correction algorithm had to be evaluated on simulated and measured data too.

The correction algorithm had to be integrated in a further step in an existing framework, which allows the reconstruction and quantification of under-sampled measurement data. This framework is based on a reconstruction approach proposed in [14]. The performance of this correction algorithm had to be evaluated, comparing the accuracy of the quantification compared to the uncorrected method of Schmitt.

2 Theory

2.1 Balanced Steady-State Free Precession (bSSFP)

In this section the bSSFP sequence is described in detail, referring to [10].

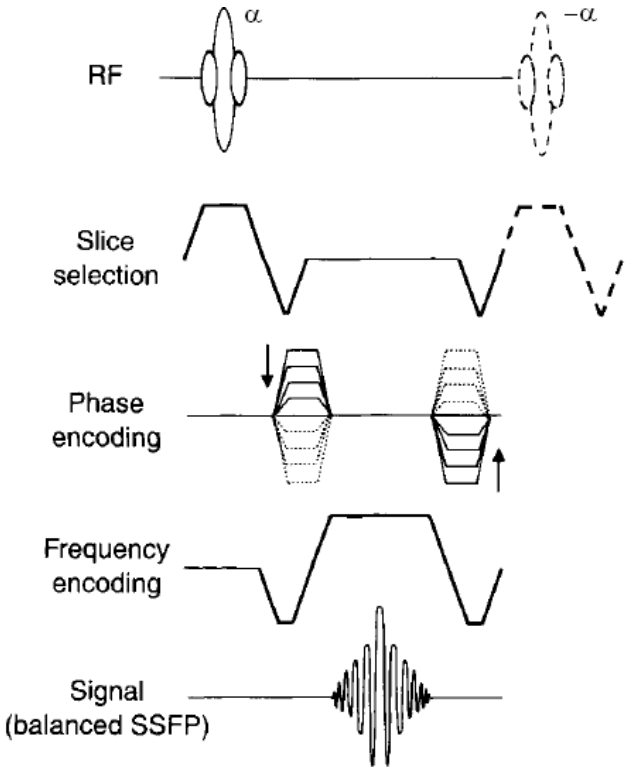

Figure 2.1: Pulse sequence for the bSSFP acquisition for one TR period. All gradients are rephased such that the net area is zero and the echo is rephased exactly at the center between two excitation pulses. This diagram is taken from [10].

The bSSFP sequence belongs to the class of GRE sequences and is also known as true fast imaging with steady-state free precession (TrueFISP), fast imaging employing steady state acquisition (FIESTA) or balanced fast field echo (FFE). This sequence provides a very high steady state signal compared to other GRE sequences, because as much signal as possible is refocused. The signal consists of all possible components, the refocused free induction decay (FID), a SE due to the previous RF-pulse and stimulated echoes because

of former RF-pulses. To achieve this, two conditions have to be satisfied. Firstly, it is necessary that no phase is accumulated due to the imaging gradients, so all gradients have to be compensated by a negative gradient with exactly the same area under the curve, such that the net gradient moment is zero during one TR period along all axes. This is the reason why it is called balanced. The second condition is that the gradients are symmetric around the readout, such that the spins are rephased exactly at the center between two excitation pulses ($TE = TR/2$). If these conditions are met, the FID, the echo and the stimulated echo component of the signal are refocused at the same time and the resulting signal is the coherent sum of these components. However, this increase in signal leads to a decrease in contrast. The corresponding sequence diagram is shown in Figure 2.1.

The excitation can be sign alternating or non-sign alternating. Typically sign alternation is applied, because of the achieved signal is higher. Sign alternating excitation can be reached by a phase shift of the RF-pulse of 180°. This causes that the flip angle changes from $+\alpha$ to $-\alpha$ at each excitation. Because of this special excitation scheme, the magnetization is partially forced back into the thermal equilibrium direction and the saturation of the longitudinal magnetization decreases [10, p. 593] (see Figure 2.3(a)). Because of that and the additionally established steady state in transverse magnetization the achieved signals are very high compared to other GRE sequences, even for a very short TR (in the order of some ms) and high flip angles. The steady-state signal for sing alternating excitation can be calculated by Eq. 2.1, where M_{ss} is the transverse steady state magnetization and α is the nominal flip angle. E_1 and E_2 are the decay rates for longitudinal and transverse relaxation respectively, M_0 is the longitudinal magnetization in thermal equilibrium and TE is the echo time, which is equal to the half of the repetition time ($TE = TR/2$). For non-sign alternating excitation a much lower steady state is reached, because of the stronger saturation of the longitudinal magnetization. This fact is shown in Figure 2.3(b). The derivation of Eq. 2.1 is described in Appendix A.1.

$$\begin{aligned} M_{ss} &= M_0 \sin(\alpha) \frac{1 - E_1}{1 - (E_1 - E_2)\cos(\alpha) - E_1 E_2} e^{-\frac{TE}{T_2}} \\ E_{1,2} &= e^{-\frac{TE}{T_{1,2}}} \end{aligned} \tag{2.1}$$

Note, that the signal decays with T_2 rather than T_2^* as it is common for spoiled GRE sequences, which is described in [15]. This is only true, if the echo is rephased exactly at TR/2. If the gradient waveform is not symmetric, TE deviates from TR/2 and there is additionally T_2^* decay. For short TR ($TR \ll T_2 < T_1$) Eq. 2.1 can be simplified to

$$M_{ss} = \frac{M_0 \sin(\alpha)}{\frac{T_1}{T_2}(1 - \cos(\alpha)) + (1 + \cos(\alpha))} e^{-\frac{TE}{T_2}}. \tag{2.2}$$

Sometimes the bSSFP sequence is said to have T_2/T_1 contrast, because of the T_1/T_2 term in the denominator of Eq. 2.2, so the signal is proportional to the ratio of T_2/T_1. The flip angle α_{max} with the maximum signal depends on T_1 and T_2 and can be calculated using Eq. 2.3, which is derived from setting the first derivative of Eq. 2.2 with respect to α to zero.

$$\alpha_{max} = \arccos\left(\frac{T_1 - T_2}{T_1 + T_2}\right) \tag{2.3}$$

The bSSFP sequence is very sensitive to off-resonance effects. In Figure 2.2 the off-resonance dependence of the steady state signal for sign alternating excitation is shown for different flip angles. If the acquired off-resonance precession angle ϕ during one TR period is in the order of 180°, the signal decreases significantly. The case of $\phi = 180°$ is equivalent to the on-resonant excitation without sign alternation. In Figure 2.3(c) the effect is shown in detail. These signal losses are called "Banding-Artifacts". To avoid this kind of artifacts, the off-resonance precession angle has to be kept as low as possible. This can be achieved by using a short TR and a very homogeneous static magnetic field B_0, which requires a very high shimming quality.

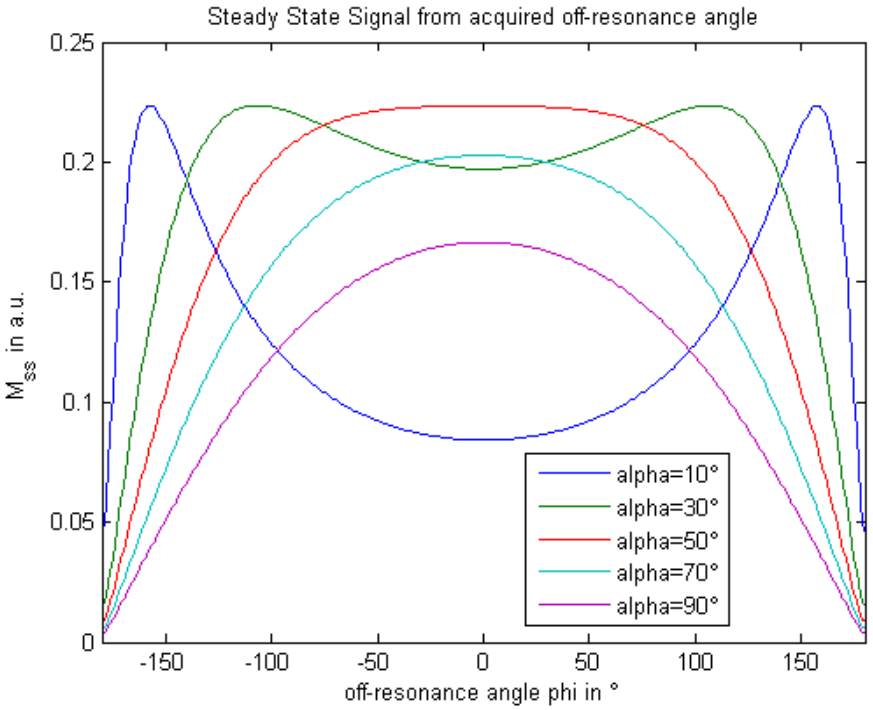

Figure 2.2: Transverse steady state magnetization M_{ss} of the bSSFP sequence against the off-resonance precession angle ϕ acquired during one TR interval for different flip angles α. The plot was simulated with sign alternating excitation and the following parameters: $T_1 = 500ms$, $T_2 = 100ms$, $TR = 4ms$. The longitudinal magnetization in thermal equilibrium M_0 is normalized to one.

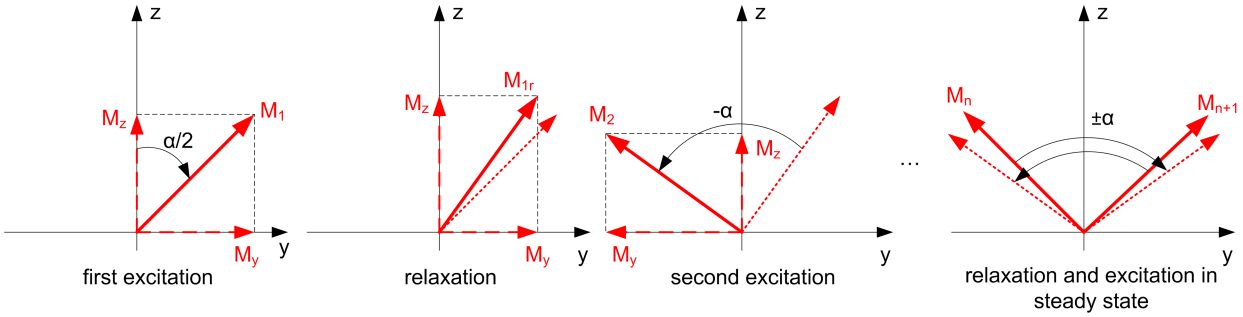

(a) Magnetization vector for sign alternating excitation with $\alpha/2$ preparation.

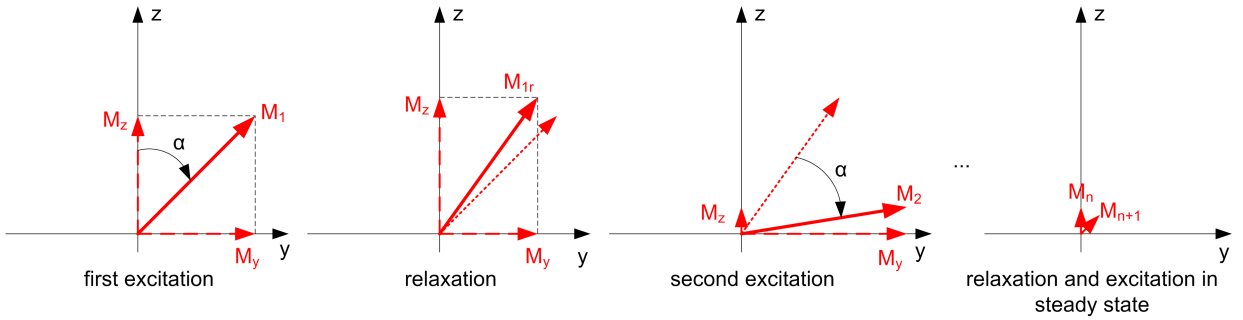

(b) Magnetization vector for non-sign alternating excitation without preparation.

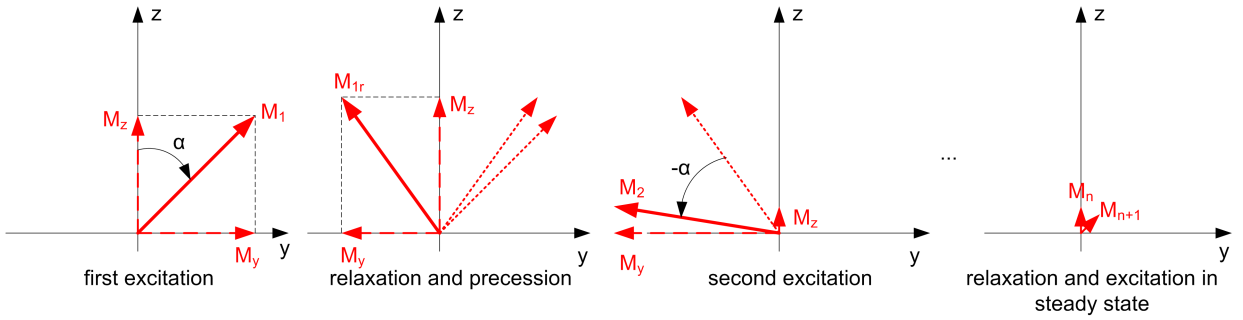

(c) Magnetization vector for sign alternating excitation and an acquired off-resonance angle of $\phi = 180°$ during one TR interval without preparation.

Figure 2.3: Evolution of the magnetization vector for sign alternating excitation with $\alpha/2$ preparation (a), non-sign alternating excitation (b) and sign alternating excitation with an off-resonance precession angel of $\phi = 180°$.

For the application of T_1 and T_2 mapping it is important to consider the transient behavior of the signal. Usually the time required to reach the steady state is in the order of four to five times T_1 [10]. If the sequence starts with the the full flip angle α (with or without sign alternation), the transient is altered by massive oscillations until the steady state is reached. Typically imaging is done in the steady state, but for some applications (for example sampling the transient time response or triggered imaging of the heart) it is necessary to acquire images during the transient as well. Due to these oscillations the resulting images suffer from heavy artifacts. To reduce these artifacts several techniques to get a smooth transient were published ([16], [17], [18] and [19]). All of them try to

push the magnetization vector into the direction of the final steady state through preparation pulses. One of the simplest approaches is to apply a RF-pulse with a flip angle of $\alpha/2$ exactly TR/2 before the first α-pulse. With this simple preparation, the steady state direction is reached immediately and only the magnitude changes. The tip of the magnetization vector during the transient is always located on a $\pm\alpha/2$-cone [16] and a totally smooth transient appears, if relaxation could be neglected. This approach and its mathematical formulation are described in detail in [16] and it is also investigated in [17]. Another approach, unfortunately less intuitive, is described in [18] using a series of preparation pulses, where the flip angle is linearly increased from α/N_{ramp} to α, where $\mathrm{N_{ramp}}$ is the number of used preparation pulses. The advantage of this ramp-up preparation approach is, that it is much more robust against variations in B_1 and off-resonances than $\alpha/2$-preparation [18] and [17]. Other methods for magnetization preparation and speeding up the progression to steady state are described with their mathematical background in [19] and [17], but for this thesis only the $\alpha/2$ and the ramp-up preparation are of interest.

Figure 2.3 shows the evolution of the magnetization vector for different important conditions. In Figure 2.3(a) sign alternating excitation and $\alpha/2$-preparation is applied. After the first RF-pulse, the magnetization is deflected out of its thermal equilibrium and starts to relax. The second RF-pulse flips the magnetization to the opposite side a little bit farther than the steady state direction due to relaxation. This leads to a little oscillation around the $\alpha/2$-cone as described in [16]. After a few pulses, the oscillations vanish when relaxation exactly balances excitation and the magnetization vector lies on the described $\alpha/2$-cone and is flipped from one side to the other. If the condition $TR \ll T_2 < T_1$ is satisfied, these oscillations can be neglected without influencing the accuracy. The steady state is reached, if the magnetization vector reaches its steady state magnitude due to relaxation.

Figure 2.3(b) shows the situation for non-sign alternating excitation without preparation. Due to flipping always in the same direction (in this case clockwise around the x-axis) the longitudinal component is saturated much more. After a train of RF-pulses, the magnetization can be rotated several times around the x-axis until the steady state is reached. This is the reason for the strongly oscillating transient when using non-sign alternating excitation. The steady state magnetization, which is established using non-sign alternating excitation is much lower compared to the sign alternating case. The reason for this is that nothing is forced back into the thermal equilibrium direction and the available magnetization before an excitation pulse becomes very low. Figure 2.3(c) shows the situation for sign alternating excitation, if an off-resonance angle of $\phi = 180°$ is acquired during one TR interval. The magnetization precesses around the z-axis to the opposite side and gets excited there, with a flip angle of opposite sign. This situation is equivalent to on-resonant non-sign alternating excitation described above.

2.2 Quantification of T_1, T_2 and Spin Density using bSSFP (Schmitt approach)

As already mentioned the transient response of an inversion recovery (IR-)bSSFP experiment can be used to determine the three contrast relevant parameters in standard MRI sequences T_1, T_2 and the pseudo spin density ρ_0 simultaneously during one measurement. This approach was described first by Schmitt [4] and it is the basis for this thesis. Because the spin density ρ_0 and the magnetization in thermal equilibrium M_0 are proportional to each other and ρ_0 can only be determined relatively, it is not distinguished between these two quantities any more, both are denoted as M_0. The derivation in [4] is done for a $\alpha/2$ prepared IR-bSSFP sequence, but it can be easily modified to fit for a ramp-up prepared sequence as well.

It is shown in [4], that the transient response of an IR-bSSFP experiment can be modeled by a three parameter mono-exponential function given in Eq. 2.4, assuming that the first readout can be acquired at time TR after the $\alpha/2$ preparation pulse and that the time between inversion and preparation (TI) is zero.

$$S(t) = S_{ss}\left(1 - INV \cdot e^{-\frac{t}{T_1^*}}\right) \tag{2.4}$$

It is shown in [16] that the decay rate of the transient of a $\alpha/2$ prepared bSSFP sequence E_1^*, assuming zero off-resonance dephasing, can be written in a simplified version as a weighted sum of the longitudinal and transverse decay rates E_1 and E_2.

$$E_1^* = E_1 \cos^2\left(\frac{\alpha}{2}\right) + E_2 \sin^2\left(\frac{\alpha}{2}\right) \tag{2.5}$$

Using $TR \ll T_2 < T_1$ Eq. 2.5 can be simplified and rewritten to get an equation for the transient time constant T_1^* as shown in the appendix.

$$T_1^* = \left(\frac{1}{T_1}\cos^2\left(\frac{\alpha}{2}\right) + \frac{1}{T_2}\sin^2\left(\frac{\alpha}{2}\right)\right)^{-1} \tag{2.6}$$

The parameter INV in Eq. 2.4 is defined by Eq. 2.7, which can be easily proved by calculating the $\lim_{t\to 0} S(t)$ in Eq. 2.4.

$$INV = 1 - \frac{S_0}{S_{ss}} \tag{2.7}$$

Due to the $\alpha/2$ preparation and neglecting the T_1 relaxation between the inversion and the preparation pulse, the signal at time zero can be calculated by:

$$S_0 = -M_0 \sin\left(\frac{\alpha}{2}\right) \tag{2.8}$$

The steady state signal is calculated according to Eq. 2.9, which is a simplified version of Eq 2.1. The derivation of the exact formula and its simplified version is shown in the appendix (Eq. A.1 – A.10).

$$S_{ss} = \frac{M_0 \sin(\alpha)}{\left(\frac{T_1}{T_2}+1\right) - \cos(\alpha)\left(\frac{T_1}{T_2}-1\right)} \tag{2.9}$$

As described in the appendix, Eq. 2.6, 2.7, 2.8 and 2.9 are used to derive equations for T_1, T_2 and M_0 using only the three parameters of the mono-exponential fit in Eq. 2.4 (S_{ss}, INV, T_1^*) and the flip angle α, where A and B are auxiliary quantities.

$$T_1 = T_1^* \left(\cos^2\left(\frac{\alpha}{2}\right) + (A \cdot INV + B)\sin^2\left(\frac{\alpha}{2}\right)\right) \tag{2.10}$$

$$T_2 = T_1^* \left(\sin^2\left(\frac{\alpha}{2}\right) + (A \cdot INV + B)^{-1}\cos^2\left(\frac{\alpha}{2}\right)\right) \tag{2.11}$$

$$M_0 = \frac{S_{ss}(INV-1)}{\sin\left(\frac{\alpha}{2}\right)} \tag{2.12}$$

$$A = 2(1-\cos(\alpha))^{-1}\cos\left(\frac{\alpha}{2}\right) \tag{2.13}$$

$$B = \left(1+2\cos\left(\frac{\alpha}{2}\right)+\cos(\alpha)\right) - (\cos(\alpha)-1)^{-1} \tag{2.14}$$

To extend this approach to a sequence with ramp-up preparation, it was assumed, that the transient time response from that time point on when preparation has finished, is equal for both preparation strategies. This assumption could be justified referring to [18], where the ramp-up preparation is described to be a method for stabilizing the SSFP sequence in general. No oscillations occur after stabilizing and therefore it can be assumed, that the magnetization vector is on the $\alpha/2$ cone.

In the ramp-up prepared sequence the first readout is done after the $(N_{ramp}+1)^{th}$ RF-pulse, which means N_{ramp} times TR later as in the $\alpha/2$ prepared case. This is considered in the fitting procedure by simply shifting the time scale by Δt in Eq. 2.4 and the time response is extrapolated until zero, which leads to the following formula:

$$S(t) = S_{ss}\left(1 - INV \cdot e^{-\frac{t+\Delta t}{T_1^*}}\right) \tag{2.15}$$

$$\Delta t = N_{ramp} \cdot TR \tag{2.16}$$

Moreover, the assumed TI of zero is unfortunately not true, a typical minimum TI for the used sequence is in the order of 20 – 30ms. To consider a real occurring TI as well, Δt is simply extended by the amount of TI. For $\alpha/2$ preparation the influence of TI is considered in the same way.

$$\Delta t = N_{ramp} \cdot TR + TI \tag{2.17}$$

2.3 Reference Measurements

To determine the accuracy of the quantified values for both T_1 and T_2 it is necessary, to get a reference value, which can be seen as ground truth. In this section the used methods to acquire these reference values are described.

2.3.1 Determination of T_1 Reference Values

To get an accurate reference value for T_1, the recovery curve of the longitudinal magnetization as shown in Figure 2.4 has to be sampled. This can either be done by an IR or a saturation recovery (SR) sequence. The longitudinal recovery curve in Figure 2.4 is plotted for an IR-sequence, where the longitudinal magnetization M_0 is normalized to 1. The curve of a SR-sequence looks similar, but it starts at zero instead of -1. Due to the wider dynamic range and therefore a better signal to noise ratio (SNR) mostly an IR-SE sequence is used in practice.

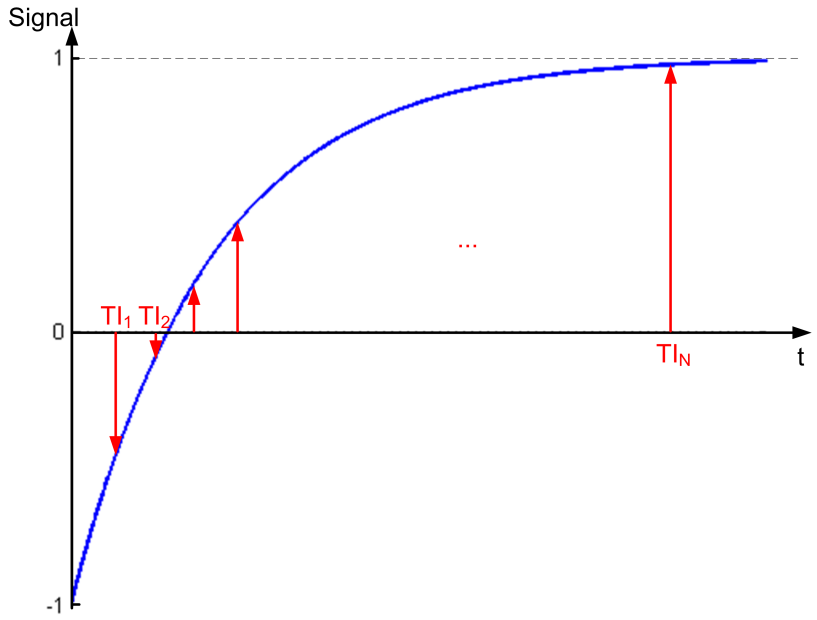

Figure 2.4: Time response for the recovery of the longitudinal magnetization after an inversion pulse, which is sampled at different inversion times. The recovery curve for a SR sequence looks similar, but it starts at zero instead of -1.

The sequence diagram for the IR-SE acquisition is shown in Figure 2.5. To get the relaxation curve in every pixel, several images have to be acquired at different inversion times. Each echo represents one single k-space line. To acquire a full image, the sequence in Figure 2.5 has to be applied W_{ph} times, where W_{ph} is the resolution in phase-encoding direction. To measure the longitudinal magnetization M_z, TE is desired to be as low as possible, to increase the SNR. Furthermore, full relaxation before the next inversion pulse

is desired. Therefore the condition $TR > 5T_{1_{max}}$ should be satisfied, where $T_{1_{max}}$ is the T_1 value of the tissue with the longest expected T_1. T_1 is typically in the range of 1 – 2s in tissue, which requires a minimum TR of about 10s. It is important to keep in mind, that for some tissues like cerebrospinal fluid (CSF) T_1 could be much longer and therefore the required TR, too. The acquisition time t_{acq} can be calculated by Eq. 2.18, where N_{TI} is the number of different inversion times used for the acquisition.

$$t_{acq} = N_{TI} \cdot W_{ph} \cdot TR \tag{2.18}$$

For a TR of 10s and a matrix size of 128x128 and 10 different inversion times, an acquisition time of 3.5 hours would be needed. The required long TR is the main reason for this extremely long duration. Due to some acceleration methods like parallel imaging, partial Fourier or a TSE acquisition, the required time can be reduced into the order of less than one hour with similar accuracy.

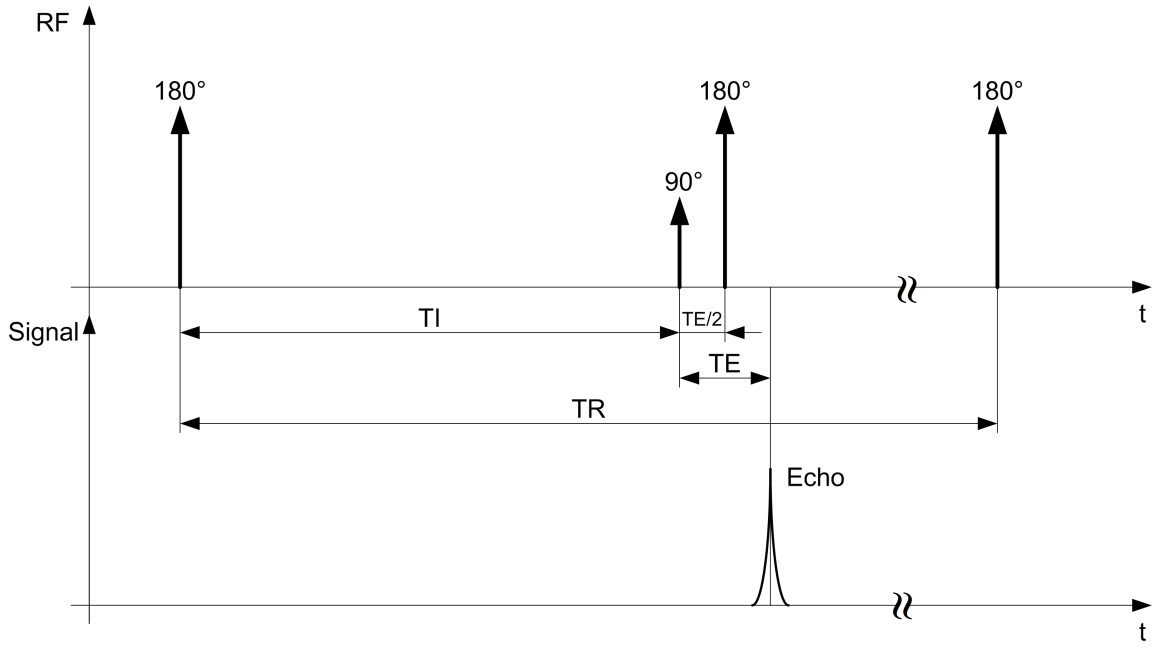

Figure 2.5: Sequence diagram for an IR-SE sequence to determine a reference value for T_1 at different inversion times. The corresponding SR-sequence looks similar, but the initial inversion pulse (180°) is replace by an saturation pulse (90°). TE is chosen as low as possible to avoid T_2 influences and TR is chosen as high, that the condition $TR > 5T_{1_{max}}$ is satisfied to ensure full relaxation before the next inversion.

The time response of SR and IR can be described by a mono-exponential behavior as stated in Eq. 2.19 and 2.20, respectively.

$$S_{SR}(TI) = M_0 \left(1 - e^{-\frac{TI}{T_1}}\right) \tag{2.19}$$

$$S_{IR}(TI) = M_0 \left(1 - 2e^{-\frac{TI}{T_1}}\right) \tag{2.20}$$

To get a value for T_1, a two parameter fit (M_0 and T_1 in Eq. 2.19 and 2.20) is performed on the acquired recovery curve in each pixel. The T_1 quantification using IR-SE can be improved using a three parameter fit according to Eq. 2.21, to consider inversion imperfections by the parameter f_{inv} as well.

$$S_{IR}(TI) = M_0 \left(1 - f_{inv} \cdot e^{-\frac{TI}{T_1}}\right) \tag{2.21}$$

Using this method for determining T_1 allows to measure the physical effect described by T_1 very accurately and is therefore used as reference measure.

2.3.2 Determination of T_2 Reference Values

The idea to get an accurate reference value for T_2 is similar to that for T_1. The difference is that the time response of the transverse magnetization after an excitation pulse is sampled by refocusing an echo by a SE-sequence at different values of TE. This can be done either with a SE or a MSE sequence. A sample T_2 relaxation curve is shown in Figure 2.6.

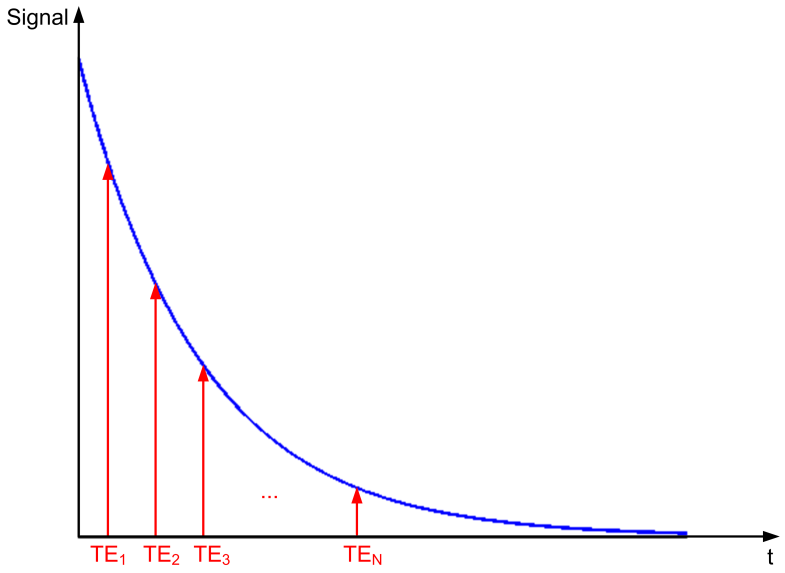

Figure 2.6: Time response of the transverse magnetization after an excitation pulse, sampled at different TEs.

The difference between SE and MSE is that the SE-sequence only acquires one echo per excitation and the MSE sequence refocuses the magnetization several times after one excitation. Therefore, the whole decay can be acquired after one single excitation by the MSE sequence and the scan time is reduced by the factor N_{TE}, which is the number of acquired echoes. The corresponding sequence diagrams for SE and MSE are depicted in Figure 2.7 and 2.8, respectively. The disadvantage of the MSE acquisition is that the relaxation curve is distorted by stimulated echoes. In general stimulated echoes occur, if

three or more arbitrary RF-pulses ($\alpha \neq 180°$) are applied. After the second RF-pulse, the transverse magnetization is partially forced back to the longitudinal direction, but their phase information is kept. The following RF-pulse flips the magnetization back to the transverse plane where a rephasing occurs. This kind of echo is called stimulated echo (see [20, p. 489 – 497]) and is responsible for an increase in the measured signal. If the 90°- and the 180°-pulses were perfect, no stimulated echoes would occur, because the magnetization would stay in the transverse plane. Due to imperfections in the scanner hardware, flip angle variations along the slice profile and B_1 variation across the imaging plane, stimulated echoes are unavoidable. A typical relaxation curve using MSE acquisition is illustrated in Figure 2.9. To correct this influence, the first echo, which does not fit into the mono-exponential decay, is skipped for the fitting procedure, such that only samples containing stimulated echoes are used. The quantification of T_2 can be improved by that, but nevertheless T_2 is systematically overestimated by the MSE acquisition. In spite of that, MSE is mostly used in literature as a reference measure for T_2 because of the massive time reduction, especially for in vivo measurements. A more sophisticated correction strategy was proposed recently in [6], which uses a closed form of the complete signal equation of the MSE sequence to perform the correction. The error compared to SE measurements can be reduced from up to 30% to lower than 5%.

The image acquisition scheme for the SE measurement is the same as for the IR-SE to determine T_1. The acquisition time for SE measurements is calculated analogous to Eq. 2.18, where N_{TI} is replaced by N_{TE}, the number of acquired echo times. The acquisition time for the MSE sequence is accelerated by the factor N_{TE}.

$$t_{acqSE} = N_{TE} \cdot W_{ph} \cdot TR \tag{2.22}$$

$$t_{acqMSE} = W_{ph} \cdot TR \tag{2.23}$$

The signal decay for SE-sequence with a 90° excitation can be modeled by Eq. 2.24. This assumes again full relaxation before the excitation, such that the condition $TR > 5T_{1_{max}}$ is satisfied. Determining of T_2 is done by a mono-exponential two parameter fit for both acquisition strategies (SE and MSE), but the first echo is skipped when using MSE.

$$S(TE) = M_0 e^{-\frac{TE}{T_2}} \tag{2.24}$$

The determination of T_2 using pure SE acquisition is one of the most accurate ways doing this, because the physical effect described by T_2 is measured as accurate as possible.

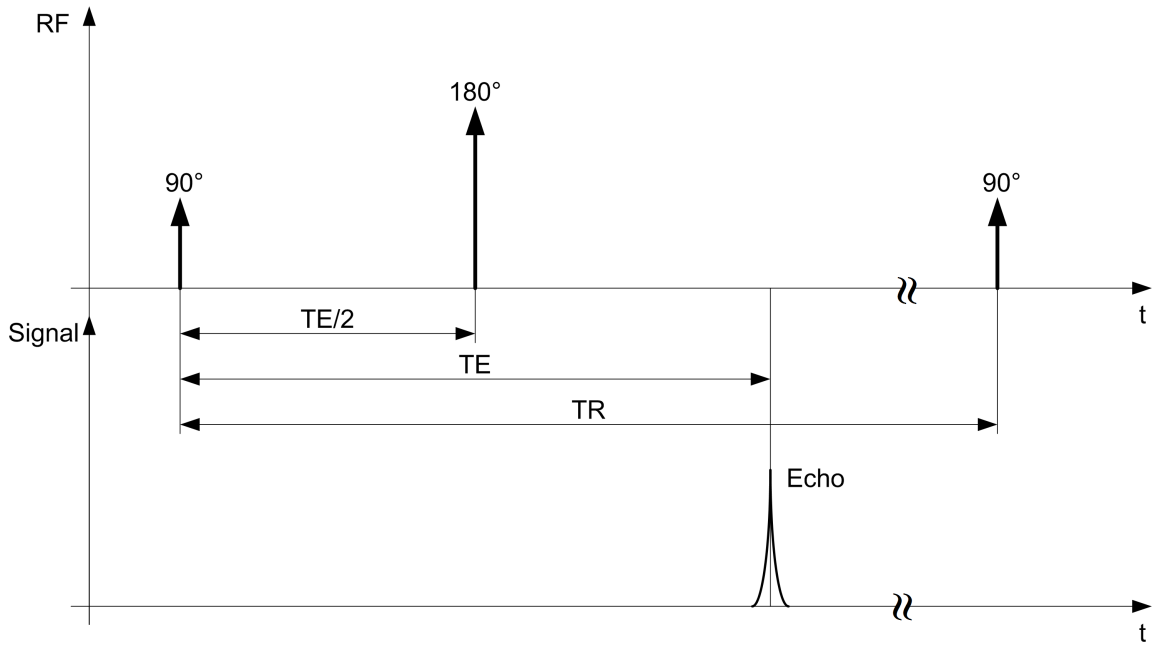

Figure 2.7: Sequence diagram for a SE sequence to determine a reference value for T_2 at different echo times. TR is required to be very long ($TR > 5T_{1_{max}}$) to ensure full relaxation before the next excitation pulse.

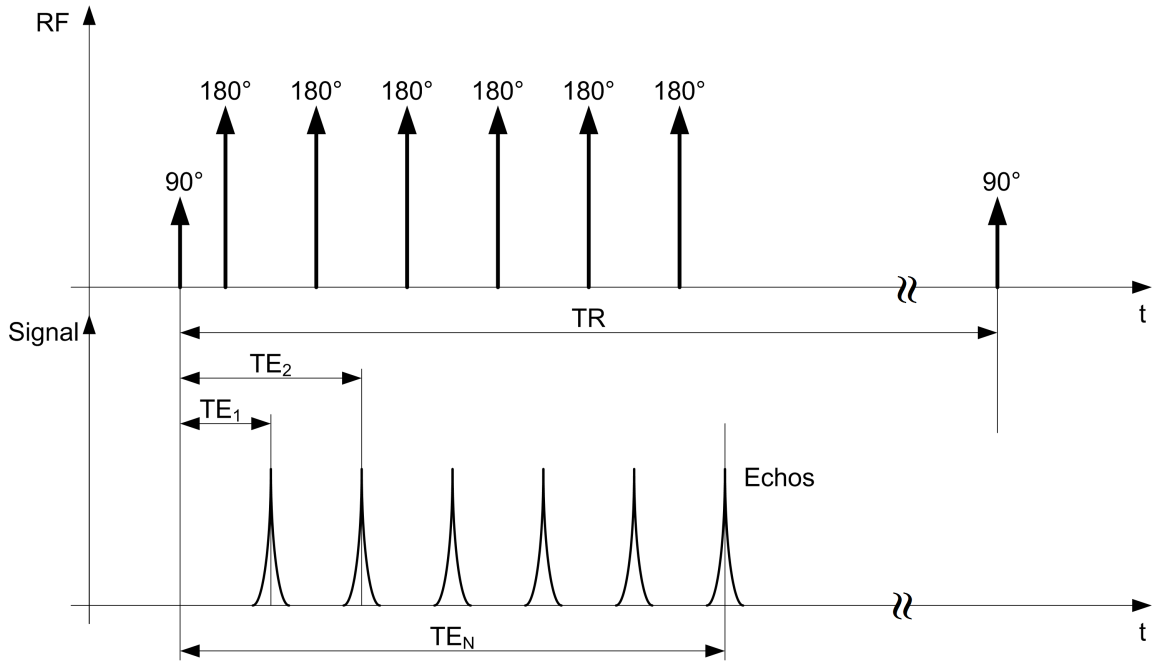

Figure 2.8: Sequence diagram for a MSE sequence to determine a reference value for T_2 at different echo times. The echo is refocused several times to speed up the measurement. TR is required to be very long ($TR > 5T_{1_{max}}$) to ensure full relaxation before the next excitation pulse.

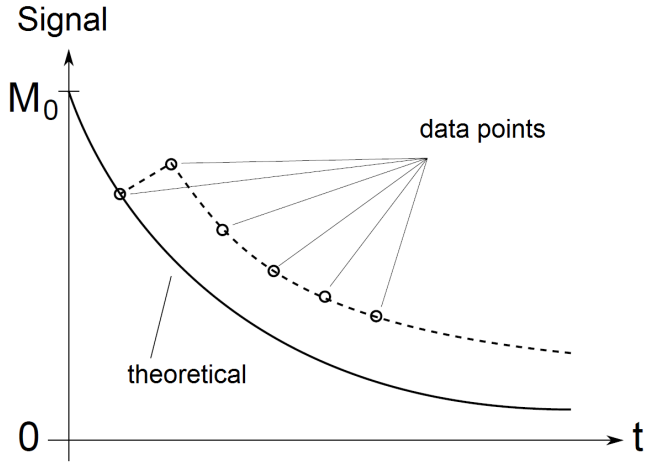

Figure 2.9: Typical relaxation curve for a MSE acquisition. From the second echo on the signal magnitude is higher than it would be expected due to the influence of stimulated echos. To achieve a better fit, the first echo is skipped for the quantification. This figure is taken from [21].

2.4 Bloch Equations

The propagation of the magnetization vector due to external field and relaxation can be described by the Bloch equations, which are a macroscopic model to describe the resulting magnetization vector in a 2 level spin system. The Bloch equations are a set of ordinary differential equations (ODE), which describe the relation between the applied magnetic field $\vec{B}_{ext}$ and the resulting magnetization vector $\vec{M}$. The information in this section is taken from [20, p. 58–63] and [22]. The vector $\vec{M}_t$ represents the transverse magnetization, which is defined as $\vec{M}_t = (M_x, M_y, 0)^T$, the vector $\vec{e}_z$ describes the unit vector in z-direction and γ represents the gyromagnetic ratio.

$$\frac{d\vec{M}}{dt} = \gamma \vec{M} \times \vec{B}_{ext} + \frac{1}{T_1}(M_0 - M_z)\,\vec{e}_z - \frac{1}{T_2}\vec{M}_t \tag{2.25}$$

The external magnetic field $\vec{B}_{ext}$ can be described as a sum of the static field B_0 in z-direction, inhomogeneities of the static field ΔB_0 and the RF-field in the transverse plane B_1.

$$\vec{B}_{ext} = \begin{pmatrix} B_1 \cos(\omega t) \\ B_1 \sin(\omega t) \\ B_0 + \Delta B_0 \end{pmatrix} \tag{2.26}$$

Normally, the magnetization vector is described in a rotating coordinate system, which rotates with the angular frequency ω, the frequency of the RF-pulse. The Bloch equations in the rotating frame change that the external magnetic field $\vec{B}_{ext}$ is replaced by an effective magnetic field $\vec{B}_e$ (see Eq. 2.28). This effective field consists of a resulting

magnetic field ΔB_0, which is zero, if the local Larmor frequency ω_0 equals the angular frequency of the RF-pulse ω. The transverse component has a fixed direction in the transverse plane. Let us assume that the B_1 vector points along the x-axis. The primed coordinates in the following formulas refer to the rotating coordinate system. In general, the magnetization is formulated in the rotating frame and therefore this explicit reference is skipped mostly in literature, as it is done in the following chapters, too.

$$\left(\frac{d\vec{M}}{dt}\right)' = \gamma\vec{M}' \times \vec{B}_e + \frac{1}{T_1}\left(M_0 - M_z\right)\vec{e}_z - \frac{1}{T_2}\vec{M}'_t \tag{2.27}$$

$$\vec{B}_e = \begin{pmatrix} B_1 \\ 0 \\ B_0 - \frac{\omega}{\gamma} \end{pmatrix} = \begin{pmatrix} B_1 \\ 0 \\ \frac{\Delta\omega}{\gamma} \end{pmatrix} \tag{2.28}$$

After calculating the cross-product in Eq. 2.27 the Bloch equations can be written in a system of differential equations for each component of the magnetization. The quantity $\Delta\omega$ describes the angular off-resonance precession frequency in the rotating coordinate system.

$$\left(\frac{dM_{x'}}{dt}\right)' = \Delta\omega M_{y'} - \frac{M_{x'}}{T_2} \tag{2.29}$$

$$\left(\frac{dM_{y'}}{dt}\right)' = -\Delta\omega M_{x'} + \omega_1 M_z - \frac{M_{y'}}{T_2} \tag{2.30}$$

$$\left(\frac{dM_z}{dt}\right)' = -\omega_1 M_{y'} + \frac{M_0 - M_z}{T_1} \tag{2.31}$$

$$\omega_0 = \gamma B_0 \tag{2.32}$$

$$\omega_1 = \gamma B_1 \tag{2.33}$$

$$\Delta\omega = \omega_0 - \omega \tag{2.34}$$

The Bloch equations in the form stated in Eq. 2.29 to 2.31 are used to derive expressions to model processes like excitation, relaxation and off-resonant precession.

Excitation: Normally, the duration of the RF-pulse used for excitation T_{RF} is very short compared to the relaxation times ($T_{RF} \ll T_2 < T_1$). Therefore the relaxation during excitation can be neglected. Furthermore, it is assumed that $\omega = \omega_0$, which is the case for on-resonant excitation, and therefore $\Delta\omega = 0$. Solving the Bloch equations lead to following expressions, which can be rewritten in vector matrix notation, where $\mathbf{R}_x$ is a rotation matrix.

$$M_{x'}(t) = M_{x'}(0) \tag{2.35}$$
$$M_{y'}(t) = -M_{z'}(0)\sin(\omega_1 t) + M_{y'}(0)\cos(\omega_1 t) \tag{2.36}$$
$$M_{z'}(t) = M_{z'}(0)\cos(\omega_1 t) + M_{y'}(0)\sin(\omega_1 t) \tag{2.37}$$

$$\overrightarrow{M'}(t) = \mathbf{R}_x(\omega_1 t)\,\overrightarrow{M'}(0) \tag{2.38}$$

Off-resonant excitation is modeled similar, but the rotation has to performed around two different axes, but the idea is the same and can be determined using the Bloch equations as well (see Section 3.4.1 on page 35).

Relaxation and precession: If no RF-field is applied, the magnetization vector precesses around the z-axis, depending on the degree of off-resonance and the relaxation forces the magnetization back to thermal equilibrium. If the local Larmor frequency ω_0 equals the angular frequency of the rotating frame ω, the direction of the transverse magnetization is fixed and only relaxation occurs. A mathematical expression for this condition can be achieved by solving the Bloch equations with $\omega_1 = 0$. This expression can be rewritten into vector and matrix notation.

$$M_{x'}(t) = e^{\frac{-t}{T_2}}\left(M_{x'}(0)\cos(\Delta\omega t) - M_{y'}(0)\sin(\Delta\omega t)\right) \tag{2.39}$$
$$M_{y'}(t) = e^{\frac{-t}{T_2}}\left(M_{y'}(0)\cos(\Delta\omega t) + M_{x'}(0)\sin(\Delta\omega t)\right) \tag{2.40}$$
$$M_{z'}(t) = M_0(0)\,e^{\frac{-t}{T_1}} + M_0\left(1 - e^{\frac{-t}{T_1}}\right) \tag{2.41}$$

$$\overrightarrow{M'}(t) = \mathbf{E}_t \cdot \mathbf{R}_z(\Delta\omega t)\,\overrightarrow{M'}(0) + \overrightarrow{e}_t \tag{2.42}$$

The rotation matrices around all three axis are given by Eq. 2.43 – 2.45. The matrix $\mathbf{E}_t$ and the vector $\overrightarrow{e}_t$ modeling the longitudinal and transverse relaxation are given by Eq. 2.46 and 2.47, respectively.

$$\mathbf{R}_x(\alpha) = \begin{pmatrix} 1 & 0 & 0 \\ 0 & \cos(\alpha) & -\sin(\alpha) \\ 0 & \sin(\alpha) & \cos(\alpha) \end{pmatrix} \tag{2.43}$$

$$\mathbf{R}_y(\alpha) = \begin{pmatrix} \cos(\alpha) & 0 & \sin(\alpha) \\ 0 & 1 & 0 \\ -\sin(\alpha) & 0 & \cos(\alpha) \end{pmatrix} \tag{2.44}$$

$$\mathbf{R}_z(\alpha) = \begin{pmatrix} \cos(\alpha) & -\sin(\alpha) & 0 \\ \sin(\alpha) & \cos(\alpha) & 0 \\ 0 & 0 & 1 \end{pmatrix} \tag{2.45}$$

$$\mathbf{E}_t = \begin{pmatrix} e^{-\frac{t}{T_2}} & 0 & 0 \\ 0 & e^{-\frac{t}{T_2}} & 0 \\ 0 & 0 & e^{-\frac{t}{T_1}} \end{pmatrix} \tag{2.46}$$

$$\vec{e}_t = \begin{pmatrix} 0 \\ 0 \\ 1 - e^{-\frac{t}{T_1}} \end{pmatrix} \cdot M_0 \tag{2.47}$$

2.5 Flip Angle Mapping using Double Angle Method (DAM)

In general, the effective B_1-field for excitation is not constant over the imaged object, because of RF-eddy currents and displacement currents [23]. The double angle method (DAM) is a technique to determine the real flip angle, which is achieved due to variations in B_1 based on image intensities introduced by [23]. The image intensities for SE-sequences are a function of various parameters, like coil sensitivity, spin density, TE, TR, flip angle, etc. In [23] it is shown that the intensity ratio I_1/I_2 acquired at different flip angles is independent of all other parameters except the two flip angles. This is only true, if both images are acquired with identical scan parameters and $TR > 5T_{1_{max}}$ to ensure complete relaxation before the following excitation. If $\alpha_2 = 2\alpha_1$ the relation I_1/I_2 can be rewritten to get an expression for the true flip angle α_{true}, where $\vec{x}$ is the spatial coordinate of the considered pixel in the image plane. The image intensity I_1 is acquired with the flip angle α_1 and the image intensity I_2 is acquired with the flip angle $2\alpha_1$.

$$\alpha_{true}\left(\vec{x}\right) = \arccos\left(\frac{I_2\left(\vec{x}\right)}{2I_1\left(\vec{x}\right)}\right) \tag{2.48}$$

For the derivation of Eq. 2.48 a linear relationship between B_1-field and flip angle α is assumed. Therefore, Eq. 2.48 is only valid for on-resonant excitation without slice selective gradients. As it is shown in [23], the relation of Eq. 2.48 can also be used as an approximation for slice selective excitation up to a flip angle of about 140°. For higher flip angles, the deviation from the linear relation has to be considered. This also depends on the flip angle profile. For non-ideal slice profiles achieved for example by a Gaussian pulse, the deviation becomes significant already at lower flip angles. This approach was used for the proposed reconstruction technique to consider B_1-variations and to improve the quality of the parameter maps.

3 Methods

3.1 Forward Model

This section contains the mathematical description of the forward model of the bSSFP sequence including the flip angle profile simulation. A complete model is described, which is used to generate simulated measurement data and also a simplified model is presented here, which is used for the reconstruction.

3.1.1 Complete Model

The bSSFP sequence can be modelled recursively over one TR interval using the results of the Bloch equations, without preparation and flip angle profile influence by Eq. 3.1. For the initial magnetization $\vec{M}_0$, it was assumed that the longitudinal magnetization M_0 is inverted completely, such that only a negative z-component appears (Eq. 3.2). This assumption is justified, because if transverse components remain after inversion, they are spoiled away as it is shown in the sequence diagram depicted in Figure 3.4 (z-gradient). M_0 can only be quantified relatively, therefore it does not matter, if the inversion is not perfect. The only condition which had to be satisfied is that always the same fraction of the true M_0 has to be flipped into the negative direction. The model in Eq. 3.1 consists mainly of rotation and relaxation matrices, which are described in Eq. 2.43 – 2.47. The excitation was modelled by a rotation around the x-axis by the flip angle α. Off-resonances were modelled by an rotation around the z-axis by the off-resonance angle ϕ acquired during one TR period. To ensure coherent data, the sign alternation had to be considered not only at the excitation, but also at the readout. Because the excitation was performed around the x-axis, the sign of the y-component of the resulting magnetization had to be changed at every second readout. This is represented by the vector $\mathbf{C}$ (Eq. 3.3). $\vec{M}_j$ denotes the magnetization vector after the j$^{\text{th}}$ excitation pulse.

$$\vec{M}_j = \left(\mathbf{E}_{TR/2} \mathbf{R}_z \left(\frac{\phi}{2} \right) \mathbf{R}_x \left(\alpha \cdot (-1)^{j-1} \right) \left(\mathbf{E}_{TR/2} \mathbf{R}_z \left(\frac{\phi}{2} \right) \vec{M}_{j-1} + \vec{e}_{TR/2} \right) + \vec{e}_{TR/2} \right) \mathbf{C} \tag{3.1}$$

$$\vec{M}_0 = \begin{pmatrix} 0 \\ 0 \\ -M_0 \end{pmatrix} \tag{3.2}$$

$$\mathbf{C} = \begin{pmatrix} 1 & 0 & 0 \\ 0 & (-1)^{j-1} & 0 \\ 0 & 0 & 1 \end{pmatrix} \tag{3.3}$$

As described in Section 2.1 and [10, p.593], the sign alternation can be modelled by an additional rotation around the z-axis by 180° and leaving the sign of the flip angle α unchanged. To include preparation as well, the flip angle is not modelled constant any more, it can vary from excitation to excitation, which is denoted as α_j. For $\alpha/2$ preparation only the first flip angle α_1 is different from the nominal one, for the ramp-up preparation the first N_{ramp} flip angles vary.

$$\vec{M}_j = \mathbf{E}_{TR/2}\mathbf{R}_z\left(\frac{\phi}{2}\right)\mathbf{R}_x\left(\alpha_j\right)\mathbf{R}_z\left(\pi\right)\left(\mathbf{E}_{TR/2}\mathbf{R}_z\left(\frac{\phi}{2}\right)\vec{M}_{j-1} + \vec{e}_{TR/2}\right) + \vec{e}_{TR/2} \tag{3.4}$$

To consider non-ideal slice profiles as well, the slice was divided into K sub-slices. The flip angle varies from sub-slice to sub-slice according to the measured flip angle profile. It was assumed, that the sub-slices are independent of each other and the forward model can be calculated separately for each of them. The resulting magnetization $\vec{M}_{j_{total}}$ is the vectorial sum of all sub-slice magnetization vectors. The length of the resulting magnetization was normalized by the number of sub-slices K.

$$\vec{M}_{j,k} = \mathbf{E}_{TR/2}\mathbf{R}_z\left(\frac{\phi}{2}\right)\mathbf{R}_x\left(\alpha_{j,k}\right)\mathbf{R}_z\left(\pi\right)\left(\mathbf{E}_{TR/2}\mathbf{R}_z\left(\frac{\phi}{2}\right)\vec{M}_{j-1,k} + \vec{e}_{TR/2}\right) + \vec{e}_{TR/2} \tag{3.5}$$

$$\vec{M}_{j_{total}} = \frac{1}{K}\sum_{k=1}^{K}\vec{M}_{j,k} \tag{3.6}$$

The relaxation was modelled by the relaxation matrix $\mathbf{E}_{TR/2}$ with the relaxation rates of T_1 and T_2 in its diagonal, and the vector $\vec{e}_{TR/2}$ to model the increase in longitudinal magnetization due to relaxation. The excitation and off-resonance precession were modelled by a rotation around the corresponding axis as described in Section 2.4.

$$\mathbf{E}_{TR/2} = \begin{pmatrix} e^{-\frac{TR/2}{T_2}} & 0 & 0 \\ 0 & e^{-\frac{TR/2}{T_2}} & 0 \\ 0 & 0 & e^{-\frac{TR/2}{T_1}} \end{pmatrix} \tag{3.7}$$

$$\vec{e}_{TR/2} = \begin{pmatrix} 0 \\ 0 \\ 1 - e^{-\frac{TR/2}{T_1}} \end{pmatrix} \cdot M_0 \tag{3.8}$$

Non-zero inversion times were model by an additional relaxation term after the inversion pulse by applying $\mathbf{E}_{TI}$ and $\vec{e}_{TI}$. Because of the spoiled transverse magnetization, only the z-component was calculated.

3.1.2 Simplified Model

The complete forward model described in Section 3.1.1 considers off-resonances, excitation, relaxation and non-ideal flip angle profiles, but it is computationally very expensive. Because of the iterative reconstruction scheme, the forward operation has to be calculated very often and therefore it was tried to simplify the forward model as much as possible to speed up the reconstruction.

The simplification starts with the complete forward model described in Eq. 3.5. Because it is difficult to determine the off-resonance precession angle ϕ, especially due to phase wraping and the required user interaction for unwraping algorithms and the massive increase of the calculation effort, we decided to neglect the off-resonance effects in the reconstruction and so ϕ is set to zero. The rotation matrices $\mathbf{R}_z\left(\frac{\phi}{2}\right)$ reduce to the identity matrix and can be skipped in Eq. 3.5. The remaining matrix operations were carried out analytically and the resulting expression was simplified as much as possible. For this purpose, the software package Mathematica (Wolfram Research, UK) in the version 9.0.1 was used.
Because the B_1-field was applied along the x-axis of the rotating frame and no off-resonances were considered, the x-component does only change due to relaxation. Due to the spoiling gradient after the inversion pulse, the initial transverse magnetization was assumed to be zero. Therefore, the x-component of the magnetization was not calculated explicitly, it was set to zero all the time. The resulting update equation for the magnetization vector between two readouts is shown in Eq. 3.9.

$$\vec{M}_{j,k} = \begin{pmatrix} 0 \\ -E_2 M_{y,j-1,k} \cos(\alpha_{j,k}) + \sqrt{E_2}\left(\left(-1+\sqrt{E_1}\right) M_0 - \sqrt{E_1} M_{z,j-1,k}\right) \sin(\alpha_{j,k}) \\ M_0 - \sqrt{E_1} M_0 + \left(\sqrt{E_1} M_0 + E_1\left(-M_0 + M_{z,j-1,k}\right)\right) \cos(\alpha_{j,k}) - \sqrt{E_1 E_2} M_{y,j-1,k} \sin(\alpha_{j,k}) \end{pmatrix} \tag{3.9}$$

3.2 Acquisition Scheme

To understand the reconstruction algorithms in Section 3.3, it is necessary to describe the acquisition scheme of the transient bSSFP response. To sample the transient time response of the bSSFP sequence after an inversion pulse, the Siemens TrueFISP_CV sequence was used. This sequence is a standard sequence for cardiovascular imaging. Cardiovascular imaging is usually performed in a triggered way, where N_{phase} images are acquired during one ECG period. On the Siemens software, these images are denoted as different cardiac phases of the ECG cycle, not to be confused with the number of phase encoding steps. In general, it is not possible to acquire the whole k-space of all cardiac phases (N_{phase}) images at once, therefore the acquisition is split up over several ECG cycles. The parameter N_{seg} defines the number of phase encoding steps (k-space lines) acquired in each of the cardiac phase images during one ECG cycle. Exactly this acquisition scheme was used to sample the transient response as well. The only difference was that the ECG signal was replaced by a simulated trigger signal with defined length. The sampling scheme of the transient time response including ramp-up preparation is illustrated in Figure 3.1 in detail for one trigger period, 6 preparation pulses ($N_{ramp} = 6$), 10 phase encoding steps ($N_{seg} = 10$) and 10 different contrasts ($N_{phase} = 10$). The index j counts the number of excitation pulses and their following readouts. It starts at the first preparation pulse (excluding the inversion pulse) and ends at the last excitation where $j = N_{max} = N_{phase}N_{seg} + N_{ramp}$. The index n counts the number of acquired images with different contrasts during the transient with a maximum at N_{phase}.

To get the complete transient behaviour, the length of one acquisition period (acquisition window, t_{acq}) should be in the order of four to five times T_1 to reach the steady state. If the number of phase encoding steps is one, the number of images with different contrasts is equal to the number of excitation pulses (neglecting preparation), which means that the echo of each excitation belongs to its own image. The transient is sampled as accurate as possible for a given TR. However, this acquisition has to be repeated for each phase encoding step until the complete k-space is filled to get full sampled data. This would lead to a very long total acquisition time t_{acq_total}. Therefore, number of phase encoding steps is in the order of 8 – 20 in practice, which is a trade-off between sampling accuracy and acquisition time. The total acquisition time can be reduced by the number of phase encoding steps. For the reconstruction, where a comparison between the simulated forward signal and the measured signal is necessary, this acquisition scheme leads to an uncertainty in time. The problem is that one image cannot be assigned to one single time point, it is a kind of average over N_{seg} time points. It turned out to work best, if one image was assigned to the time point of the first echo, because as you can see in Figure 3.3 the central k-space line, which is responsible for the main contrast, is acquired

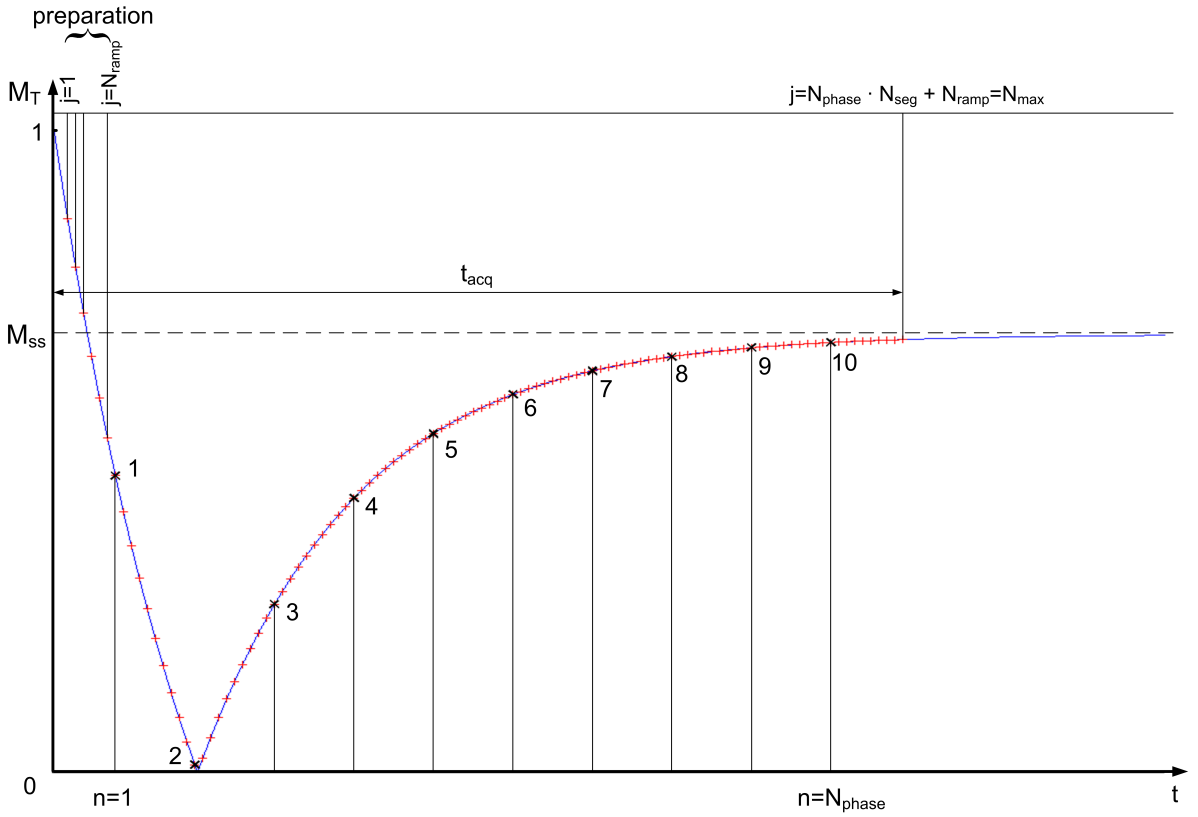

Figure 3.1: Acquisition scheme to sample the transient time response of the bSSFP sequence after an inversion pulse, where N_{seg} is the number of phase encoding steps acquired in each of the N_{phase} images with different contrast after one inversion.

at first. The number of acquired images with different contrast N_{phase} is a result of the acquisition window t_{acq}, the number of phase encoding steps N_{seg}, the time necessary for the inversion and preparation t_{prep} and the used repetition time TR:

$$N_{phase} = \frac{t_{acq} - t_{prep}}{TR \cdot N_{seg}} \tag{3.10}$$

After the last acquired echo, a sufficiently long time t_{wait} has to be waited, to ensure full relaxation before the next inversion. This can be done by choosing a sufficient number of trigger pulses N_{trig} between two inversions. t_{wait} should be in the range of four to five T_1, too. In Figures 3.2 – 3.4 a sequence diagram for the acquisition of a 64x64 matrix, with 16 phase encoding steps ($N_{seg} = 16$), 3 different contrasts ($N_{phase} = 3$) and an acquisition window of 303ms ($t_{acq} = 303ms$) is shown at different zoom levels. The figures were generated by a simulation of the Siemens TrueFISP_CV sequence using the sequence development environment MultiIDEA in the version VB17a. Figure 3.2 shows the complete sequence. During the first acquisition window no signal is measured (analog to digital converter (ADC) signal is zero), so there is an overhead of one acquisition window in this sequence. The reason for that is maybe an additional preparation strategy concerning

cardiovascular imaging. To get full sampled data, the transient has to be sampled four times in this case (4x16=64), plus one more for additional preparation. Normally, every inversion pulse is applied N_{trig} trigger pulses after the previous inversion. The Multi-IDEA simulation cannot be triggered, so the inversion pulse is applied directly after the last readout of the previous acquisition window. This is the only difference to the real implementation on the scanner.

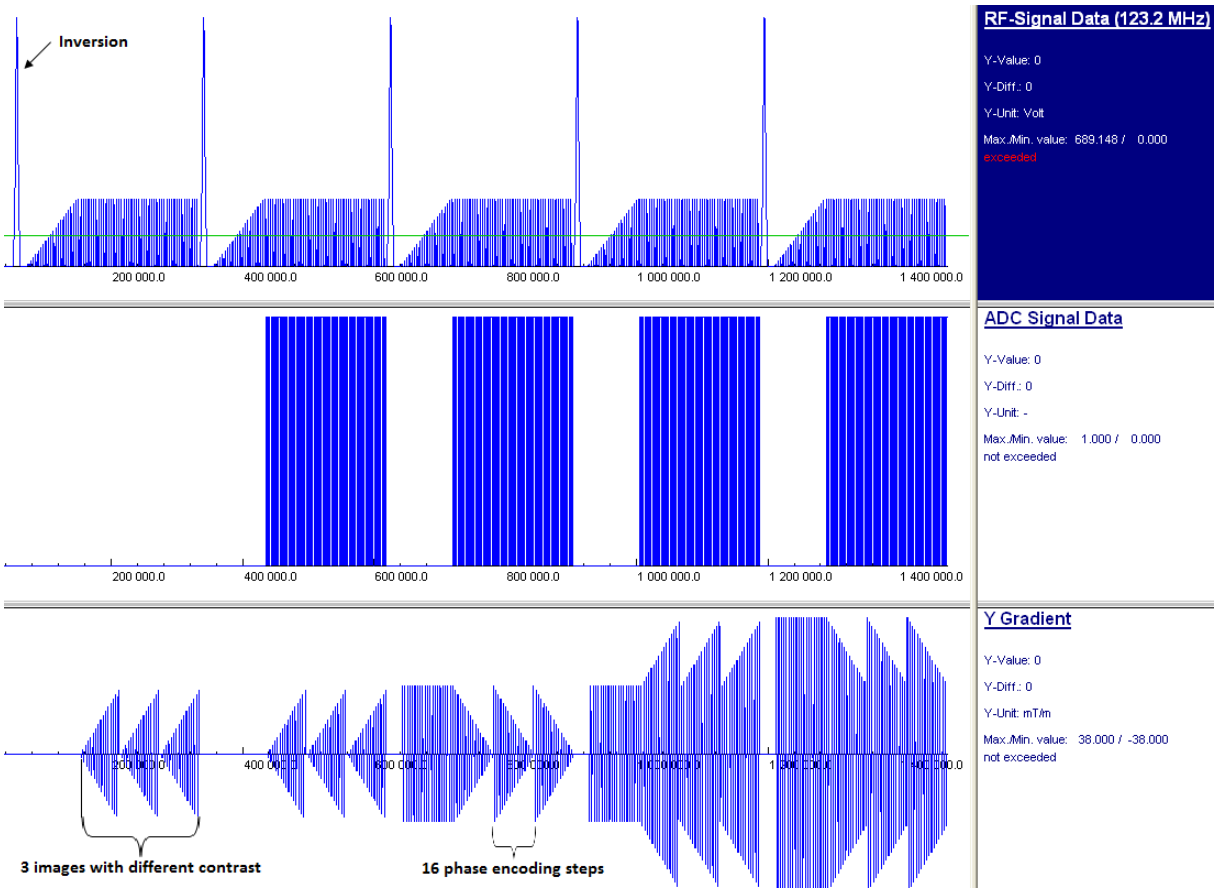

Figure 3.2: Sequence diagram for the acquisition of 16 phase encoding steps and 3 different contrasts for the TrueFISP_CV sequence in a Siemens VB17a environment. The RF-pulses, the phase encoding gradient and the ADC signal are illustrated for the whole acquisition.

Figure 3.3 depicts the first acquisition window where data is acquired. After the preparation pulses, you can see the center k-space line is acquired first, followed by the first 15 lines with negative phase encoding gradient. This is done in the same way in all N_{phase} images with different contrast. In Figure 3.4, only the preparation period is illustrated. The preparation is done by a linear ramp of 20 preparation pulses, before the first readout occurs. Furthermore, you can see that every gradient is balanced by a negative gradient of the same area. After the inversion pulse, a relative strong and long gradient in z-direction is applied to spoil transverse magnetization due to imperfect inversion.

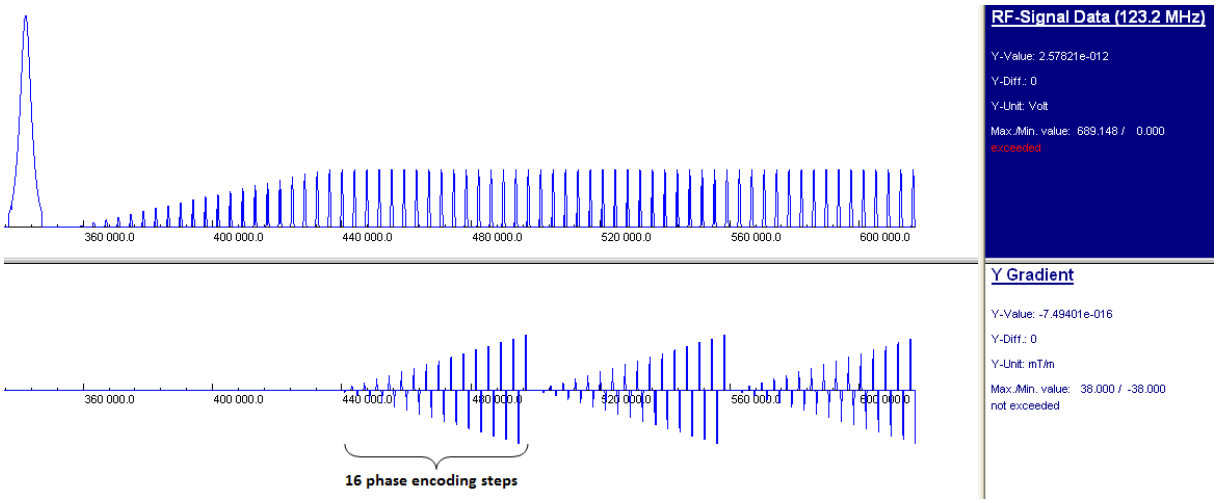

Figure 3.3: Sequence diagram for the acquisition of 16 phase encoding steps and 3 different contrasts for the TrueFISP_CV sequence in a Siemens VB17a environment. The RF-pulses and the phase encoding gradient are illustrated for one acquisition period after a trigger pulse.

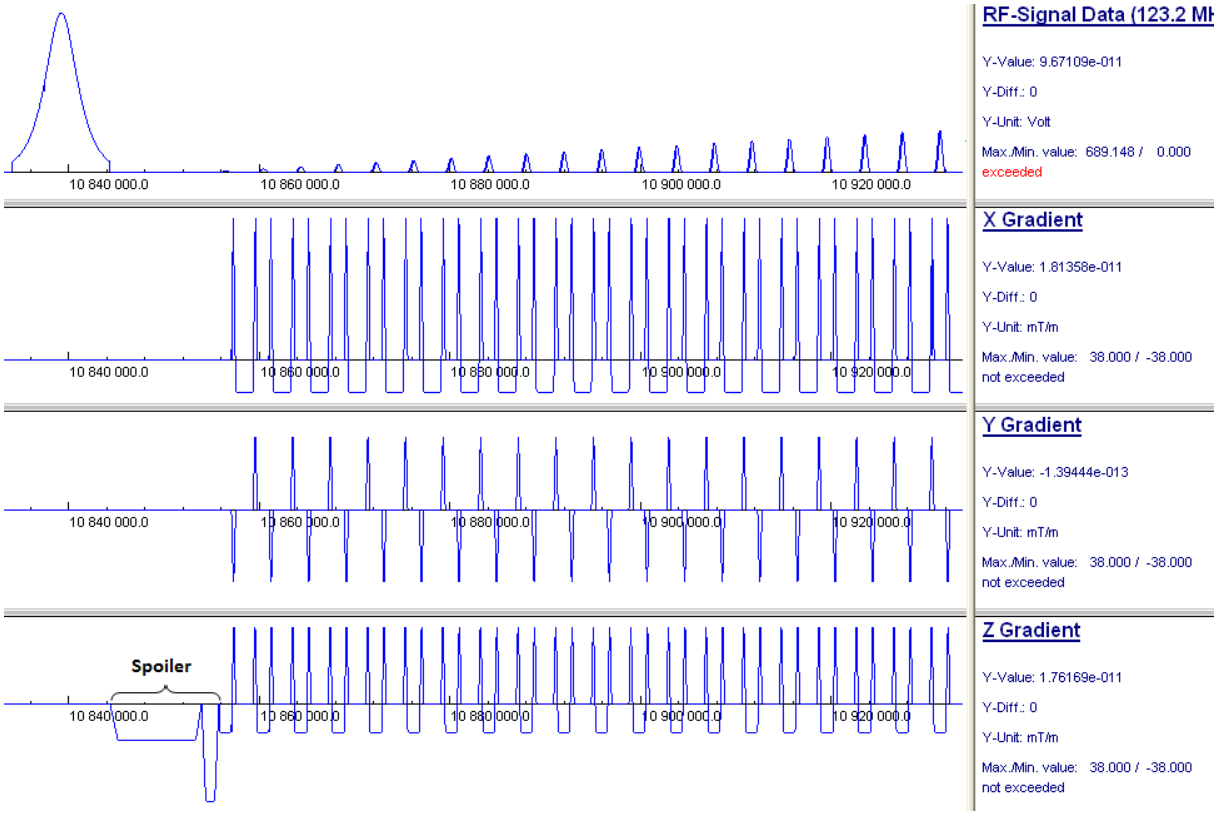

Figure 3.4: Sequence diagram for the TrueFISP_CV sequence in a Siemens VB17a environment during the preparation period. The RF-pulses and all gradients are illustrated. It can be seen that all gradients are rephased and the spoiling gradient after the inversion pulse in z-direction.

3.3 Reconstruction

Two different reconstruction algorithms were implemented to reconstruct the parameter maps. For the first algorithm, all voxels were seen as independent and the reconstruction is performed on the basis of their individual transient response out of already reconstructed images. The second algorithm performs the reconstruction on k-space data to allow a reconstruction of under-sampled data. The details of both algorithms are described in this section.

3.3.1 Pixel by Pixel Reconstruction

The pixel wise reconstruction algorithm is mainly based on the algorithm proposed in [24]. The parameter map can be calculated by minimizing the difference between the forward model and the measured data in a least square sense (Eq. 3.11), where $\vec{T}$ is the 3 dimensional parameter vector in each pixel.

$$\vec{T}\left(\vec{x}\right) = \underset{T_1,T_2,M_0}{\operatorname{argmin}} \sum_{n=1}^{N_{phase}} \left(S_{meas}\left(n,\vec{x}\right) - S_{sim}\left(n,\vec{x},T_1,T_2,M_0,\alpha\right)\right)^2 \tag{3.11}$$

$$\vec{T}\left(\vec{x}\right) = \begin{pmatrix} T_1\left(\vec{x}\right) \\ T_2\left(\vec{x}\right) \\ M_0\left(\vec{x}\right) \end{pmatrix} \tag{3.12}$$

The simulated signal S_{sim} is proportional to the sum over the transverse components of the magnetization in all sub-slices, which were calculated by the simplified forward model stated in Eq. 3.9. The complete transverse magnetization is calculated as the vectorial sum of the magnetization vectors in each sub-slices as stated in Eq. 3.6, which can be reduced to the sum over the y-components of the magnetization, because the x-components are always zero due to the excitation scheme and the on-resonance assumption. The resulting magnetization was normalized by the number of sub-slices K. The factor c_{ap} is a proportionality factor between the magnetization and the measured signal, including coil sensitivities, gain factors, etc. However, c_{ap} is only stated for mathematical correctness due to normalization of both signals, it has no practical relevance. S_{meas} is the measured signal which is proportional to the image intensity.

$$S_{sim}\left(n,T_1,T_2,M_0,\alpha\right) = \frac{c_{ap}}{K}\sqrt{\left(\sum_{k=1}^{K} M_{x,n,k}\right)^2 + \left(\sum_{k=1}^{K} M_{y,n,k}\right)^2} = \frac{c_{ap}}{K}\sum_{k=1}^{K} M_{y,n,k} \tag{3.13}$$

$$M_{xy,n,k} = M_{xy,j,k}, \quad \text{if} \quad (j - N_{ramp}) \bmod N_{seg} = 0 \quad \text{and} \quad n = \frac{j - N_{ramp}}{N_{seg}} \tag{3.14}$$

Eq. 3.14 considers the acquisition scheme shown in Figure 3.1 mathematically. The transverse magnetization was only used at time point n when the acquisition of a new image starts. $M_{xy,n,k}$ is the x or the y-component of the magnetization vector at time point n and sub-slice k. The cost function of Eq. 3.11 was solved by a so called "Simplex Solver" proposed by Nelder and Mead [25]. The advantage of this solver is that no gradient has to be calculated. The idea is that an initial simplex is built up in the parameter space. The number of vertices of this simplex is $m + 1$ where m is the dimension of the parameter space. The cost function is evaluated at all vertices and the vertex with the highest value is projected into the direction of the others. This is repeated until a convergence criterion is met.

To consider B_1 variations as well, the flip angle profile was multiplied by a factor f_α, which is derived by the DAM described in Section 2.5, referring to [23]. The real flip angle can be calculated by Eq. 2.48, where I_2 is the image intensity acquired with a flip angle of 2α, I_1 is the image intensity acquired with flip angle α and x the spatial coordinate in the imaging plane. The correction factor f_α was calculated as the relation between the real flip angle α_{true} and the nominal flip angle α_{nom}.

$$f_\alpha = \frac{\alpha_{true}}{\alpha_{nom}} \tag{3.15}$$

Implementation: The reconstruction algorithm as well as the forward simulation were implemented in MATLAB (Mathworks Inc., Natick, USA) in the version 7.12.0. To evaluate the performance and the quantification accuracy of the algorithm, the pixel wise reconstruction algorithm was applied to simulated data. To generate the simulated data, the complete forward model (Eq. 3.5 and 3.6) and the measured flip angle profile with a slice thickness of 20mm was used. The slice profile was sampled 251 times ($K_{sim} = 251$) over the range where the flip angle lay above the noise level. Depending on the investigated parameters, the generated data was corrupted with a certain amount of Gaussian white noise. The preparation was sourced out into a particular function, calculating the magnetization vector after the last preconditioning pulse. The preconditioning scheme ($\alpha/2$ or ramp-up preparation) can be selected by a flag. The minimization of the cost function was done by the MATLAB implementation of the Nelder-Mead simplex solver (*fminsearch()*). This solver needs beside the cost function an initial value for the parameters to estimate. These initial values were determined by applying the Schmitt-approach to the data of interest. This ensured that the solver is initialized near the minimum. The initial value for M_0 was set to one. The solver could also be initialized arbitrary by a typical value, but this would unnecessarily elongate the reconstruction time. Furthermore, an accurate initial value is important for the convergence of the minimizer. The forward model calculated in the cost function at each iteration of the minimizer used the

simplified forward model and a slice profile measured with a slice thickness of 5mm, which was sampled 18 times ($K_{recon} = 18$) in the important range.

The pixel wise reconstruction is based on DICOM files, where the image intensity is proportional to the magnitude of the transverse magnetization in a value range of 0 to 4096, which was normalized to a range between 0 and 1. Because all pixels are seen as independent of each other, the reconstruction can be easily parallelized. This is done by reconstructing each pixel in its own thread using the Parallel Computing Toolbox of MATLAB. To decrease the calculation effort, background pixels were suppressed by using a binary mask generated by a simple threshold operation. The threshold value has to be adjusted to the measured object. An automatic determination of an accurate threshold would be useful here. For further acceleration, as many things as possible were precalculated, for example the sine and cosine of the flip angle profile. The DAM correction factor $f_\alpha(\vec{x})$ in each pixel was calculated before the actual reconstruction starts. If no DAM measurement was performed, the correction factor was set to one.

To compare the improvement achieved by the slice profile correction, all parameter maps were reconstructed with the Schmitt-approach as well. For considering different influences on the quantification accuracy of the Schmitt approach, it was applied to simulated data, too. The method of Schmitt was implemented by fitting the absolute value of the three parameter mono-exponential function from Eq. 2.4 to the transient in each pixel or the simulated data using the Curve Fitting Toolbox of MATLAB. The parameters were calculated by Eq. 2.10 – 2.14.

3.3.2 Under-Sampled Reconstruction in k-Space

To reduce the scan time, a novel reconstruction scheme for T_2 mapping using highly under-sampled SE data, based on model-based nonlinear inverse reconstruction was proposed by [14]. Normally, T_2 mapping is done by fitting a mono-exponential decay into the measured signal at different values of TE, based on a series of already reconstructed images as described in Section 2.3.2. The approach of [14] uses under-sampled data, where a conventional Fourier reconstruction is not possible, because the Nyquist criterion is violated. Therefore, the data fit is done directly using k-space data. This model-based nonlinear inverse reconstruction scheme was already expanded to reconstruct parameter maps of under-sampled data using the "Schmitt approach". In this section, the reconstruction scheme of [14] is described and its expansion to enable the reconstruction of T_1, T_2 and M_0 including non-ideal slice profiles.

3.3.2.1 Model-Based Nonlinear Inverse Reconstruction

The parameter maps obtained by the model-based nonlinear inverse reconstruction scheme of [14] are also the result of minimizing a cost function, which is stated in Eq. 3.16. The idea is the same as in the pixel wise reconstruction. It is tried to reduce the squared error between the simulated model and the measured data during the transient of the bSSFP sequence, but the way of doing this is completely different. The main difference is that the whole image is considered at once. In every iteration step of the minimizer, the forward model of the whole transient has to be calculated in every pixel $\vec{x}$. Therefore, the simplified forward model stated in Eq. 3.9, 3.13 and 3.14 was used. This results in $\mathbf{S}_{sim}$, which can be seen as a stack of simulated forward images considering the complete transient at every sample point from 1 to N_{phase}. These simulated images were transferred to an artificial k-space using the discrete Fourier transform and multiplied by the matrix $\mathbf{P}$, which is a binary mask representing the applied under-sampling pattern. $\mathbf{S}_{meas}$ are the measured under-sampled k-spaces for all N_{phase} images with different contrast acquired during the transient. The dimension of the parameter vector $\vec{T}$ increases to three times the number of pixels (T_1, T_2 and M_0 in each pixel).

$$\vec{T} = \underset{\vec{T}}{\operatorname{argmin}}\, J\left(\vec{T}\right) = \underset{\vec{T}}{\operatorname{argmin}}\, \frac{1}{2} \sum_{n=1}^{N_{phase}} \left\| \mathbf{P} \cdot \mathrm{DFT}\left\{ \mathbf{S}_{sim}\left(n, \vec{T}\right)\right\} - \mathbf{S}_{meas}\left(n\right)\right\|_2^2 \tag{3.16}$$

$$\vec{T} = \begin{pmatrix} \vec{T}_1\left(\vec{x}\right) \\ \vec{T}_2\left(\vec{x}\right) \\ \vec{M}_0\left(\vec{x}\right) \end{pmatrix} \tag{3.17}$$

If multichannel receiver coils are used, the cost function $J\left(\vec{T}\right)$ has to be extended by their individual coil sensitivities $\mathbf{C}_c$, and an additional sum over all N_{coil} channels.

$$J\left(\vec{T}\right) = \frac{1}{2} \sum_{c=1}^{N_{coil}} \sum_{n=1}^{N_{phase}} \left\| \mathbf{P} \cdot \mathrm{DFT}\left\{ \mathbf{S}_{sim}\left(n, \vec{T}\right) \cdot \mathbf{C}_c\right\} - \mathbf{S}_{meas}\left(n, c\right)\right\|_2^2 \tag{3.18}$$

The coil sensitivities were estimated based on the under-sampled k-space data using an algorithm proposed by [26]. The cost function was minimized by a conjugated gradient solver described in [27], which needs the gradient of the cost function. The idea of gradient calculation for this sort of cost functions was taken from the original paper [14], and generalized to any kind of signal equations. The main part is the calculation of the derivative of the signal equation, which is much more complicated as in the original model, because the signal equation is only stated recursively.

Implementation: The implementation of this algorithm is based on the original MATLAB implementation of [14], which was already extended to perform parameter quan-

tification using the Schmitt approach. It includes the coil sensitivity estimation, initial parameter estimation, the solver and a powerful framework combining all elements. The coil sensitivity estimation was only performed, if more than one coil is detected, because for a single channel measurement the algorithm is not able to separate image information and variations in intensity due to varying coil sensitivities. In this case, the coil sensitivity was set to one over the whole image. The sequence implemented on the scanner is not able to generate under-sampled data, so the desired under-sampling pattern is generated artificially after reading the raw-data file. The DAM correction was performed exactly the same as for the pixel wise reconstruction. To create an initial guess to initialize the solver, a parameter map was calculated by applying the Schmitt-approach. This was not that easy as it is in pixel wise reconstruction. To perform this, the N_{phase} under-sampled k-spaces at each time point of the transient were combined in such a way, that N_{phase}/δ full sampled k-spaces were available, where δ is the under-sampling factor. Now it was possible to reconstruct each of them to get a coarser sampling of the transient. However, these images are corrupted by massive back-folding artefacts due to the inconsistent k-spaces, but it could be used to create an initial guess for the parameter map using the Schmitt-approach. It turned out to work best, if the M_0 map was initialized with zero. The gradient in M_0 dominated during the first few iterations and a practicable value for M_0 was reached after a few iterations.

To reduce the effort of calculating the forward model and the gradient in each iteration step of the solver, background pixels which give no information beside noise were neglected by using a binary mask. This mask was generated by using the last δ k-spaces acquired during the transient to get one full sampled k-space. If the steady state has reached already, nothing changes any more and a complete undistorted image can be reconstructed. The mask was generated out of this image by a threshold operation, where the threshold had to be adjusted to the investigated object. The mask was refined by morphological operations to get a closed mask.

The cost function was minimized by a conjugate gradient solver, which is an original implementation of [27] and was written in C. It is attached to the MATLAB framework by the internal C-compiler *mex*. Beside the initial parameter maps, the solver needs the functions names of the gradient and the cost function. The cost function and the gradient calculation were implemented according to the formulas described in this section. The complete gradient expressions are shown in the Appendix A.3. Unfortunately, the minimization procedure cannot be parallelized, but the cost function and gradient calculations are partially independent, and can be split up into an own thread for each pixel. This is done using the Parallel Computing Toolbox of MATLAB.

3.3.2.2 Gradient of the Cost Function

The gradient of Eq. 3.18 can be calculated as stated in Eq. 3.19, which is a generalized version out of [14].

$$\begin{aligned}
\nabla J\left(\vec{T}\right) &= \begin{pmatrix} \frac{dJ}{dT_1} \\ \frac{dJ}{dT_2} \\ \frac{dJ}{dM_0} \end{pmatrix} \\
\frac{dJ}{dT_1}\left(\vec{x}\right) &= \sum_{c=1}^{N_{coil}} \sum_{n=1}^{N_{phase}} \frac{\partial \mathbf{S}_{sim}\left(n, \vec{x}\right)}{\partial T_1} \cdot \mathbf{K}_{c,n}\left(\vec{x}\right) \\
\frac{dJ}{dT_2}\left(\vec{x}\right) &= \sum_{c=1}^{N_{coil}} \sum_{n=1}^{N_{phase}} \frac{\partial \mathbf{S}_{sim}\left(n, \vec{x}\right)}{\partial T_2} \cdot \mathbf{K}_{c,n}\left(\vec{x}\right) \\
\frac{dJ}{dM_0}\left(\vec{x}\right) &= \sum_{c=1}^{N_{coil}} \sum_{n=1}^{N_{phase}} \frac{\partial \mathbf{S}_{sim}\left(n, \vec{x}\right)}{\partial M_0} \cdot \mathbf{K}_{c,n}\left(\vec{x}\right) \\
\mathbf{K}_{c,n} &= \overline{\mathbf{C}}_c \cdot \mathrm{DFT}^{-1}\left\{\mathbf{P} \cdot \mathrm{DFT}\left\{\mathbf{S}_{sim}\left(n\right) \cdot \mathbf{C}_c\right\} - \mathbf{S}_{meas}\left(n\right)\right\}
\end{aligned} \tag{3.19}$$

Because of Eq. 3.13, the simulated signal at time point n is proportional to the transverse magnetization at time point n. The transverse magnetization is the vectorial sum of the transverse magnetization in every sub-slice (Eq. 3.13). Due to the excitation scheme and the on-resonance assumption, the x-component of the transverse magnetization is zero at any time point. Therefore, the simulated signal is proportional to the sum over the y-components of the magnetization in each sub-slice (Eq. 3.13), so the derivative of the simulated signal can be calculated by the sum of the derivatives of the magnetization in the sub-slices and a constant factor (Eq. 3.20). All sub-slices are seen as completely independent of each other, so the following calculations are performed for each sub-slice separately and the sub-slice index k is skipped due to clarity.

$$\frac{\partial \mathbf{S}_{sim}\left(n, \vec{x}\right)}{\partial \vec{T}} = \frac{c_{ap}}{K} \sum_{k=1}^{K} \frac{\partial \mathbf{M}_{y,n,k}\left(\vec{x}\right)}{\partial \vec{T}} \tag{3.20}$$

The transverse magnetization is calculated iteratively by Eq. 3.9, so the calculation of the derivative is not as trivial as in [14]. For this purpose the "implicit function theorem" described in [28, p. 286 – 299] was used. The idea was to rewrite the iterative scheme of Eq. 3.9 in an implicit scheme. Therefore, Eq. 3.9 had to be rewritten into the form

$$\vec{M}_{j+1} = \mathbf{A}_j\left(\vec{T}\right)\vec{M}_j + \vec{d}_j\left(\vec{T}\right), \quad \vec{M}_j = \begin{pmatrix} M_{y,j} \\ M_{z,j} \end{pmatrix} \tag{3.21}$$

$$\mathbf{A}_j = \begin{pmatrix} -E_2\cos\left(\alpha_j\right) & -\sqrt{E_1E_2}\sin\left(\alpha_j\right) \\ -\sqrt{E_1E_2}\sin\left(\alpha_j\right) & E_1\cos\left(\alpha_j\right) \end{pmatrix} \tag{3.22}$$

$$\vec{d}_j = \begin{pmatrix} -\left(1-\sqrt{E_1}\right)\sqrt{E_2}M_0\sin\left(\alpha_j\right) \\ \left(1-\sqrt{E_1}\right)M_0\left(1+\sqrt{E_1}\cos\left(\alpha_j\right)\right) \end{pmatrix} \tag{3.23}$$

$$\vec{T} = \begin{pmatrix} T_1 \\ T_2 \\ M_0 \end{pmatrix}. \tag{3.24}$$

The implicit form of Eq. 3.21 could be written as:

$$\vec{F}_j = -\mathbf{A}_j\left(\vec{T}\right)\vec{M}_j + \vec{M}_{j+1} - \vec{d}_j\left(\vec{T}\right) = 0 \tag{3.25}$$

The whole transient can be written in the implicit form using vector and matrix notation

$$\vec{F}\left(\vec{T},\vec{M}\right) = \begin{pmatrix} I & 0 & 0 & ... & 0 & 0 \\ -\mathbf{A}_1 & I & 0 & ... & 0 & 0 \\ 0 & -\mathbf{A}_2 & I & ... & 0 & 0 \\ \vdots & \vdots & \vdots & & \vdots & \vdots \\ 0 & 0 & 0 & ... & -\mathbf{A}_{N_{max}} & I \end{pmatrix} \begin{pmatrix} \vec{M}_0 \\ \vec{M}_1 \\ \vec{M}_2 \\ \vdots \\ \vec{M}_{N_{max}} \end{pmatrix} - \begin{pmatrix} \vec{d}_0 \\ \vec{d}_1 \\ \vec{d}_2 \\ \vdots \\ \vec{d}_{N_{max}} \end{pmatrix} = \vec{0}, \tag{3.26}$$

or in condensed form:

$$\vec{F}\left(\vec{T},\vec{M}\right) = \mathbf{A}\left(\vec{T}\right)\cdot\vec{M} - \vec{d}\left(\vec{T}\right) = \vec{0} \tag{3.27}$$

The derivatives of $\vec{F}$ can be calculated directly using standard algebra.

$$\frac{\partial\vec{F}}{\partial\vec{T}} = \begin{pmatrix} \frac{\partial\vec{F}_1}{\partial T_1} & \frac{\partial\vec{F}_1}{\partial T_2} & \frac{\partial\vec{F}_1}{\partial M_0} \\ \frac{\partial\vec{F}_2}{\partial T_1} & \frac{\partial\vec{F}_2}{\partial T_2} & \frac{\partial\vec{F}_2}{\partial M_0} \\ \vdots & \vdots & \vdots \\ \frac{\partial\vec{F}_{N_{max}}}{\partial T_1} & \frac{\partial\vec{F}_{N_{max}}}{\partial T_2} & \frac{\partial\vec{F}_{N_{max}}}{\partial M_0} \end{pmatrix}, \quad \frac{\partial\vec{F}}{\partial\vec{M}} = \mathbf{A} \tag{3.28}$$

The derivative of $\vec{M}$ can be calculated using the relation stated in [28, p. 299].

$$\frac{\partial\vec{M}}{\partial\vec{T}} = -\left(\frac{\partial\vec{F}}{\partial\vec{M}}\right)^{-1}\frac{\partial\vec{F}}{\partial\vec{T}} = -\mathbf{A}^{-1}\frac{\partial\vec{F}}{\partial\vec{T}} \tag{3.29}$$

Because of the huge calculation effort, especially for inverting the matrix $\mathbf{A}$, the derivative was calculated iteratively by an numerically equivalent scheme. The basis for it was the simplified forward model in Eq. 3.9. The complete expressions for the derivatives are stated in Section A.3 of the Appendix.

$$\frac{\partial\vec{M}_{j+1}}{\partial\vec{T}} = \frac{\partial\mathbf{A}_j}{\partial\vec{T}}\vec{M}_j + \mathbf{A}_j\frac{\partial\vec{M}_j}{\partial\vec{T}} + \frac{\partial\vec{d}_j}{\partial\vec{T}} \tag{3.30}$$

3.4 Real Flip Angle Profiles

In this section, two methods of determining the real flip angle profile along the excited slice for the RF-pulse types used in the TrueFISP_CV sequence are described. The first one is to simulate the flip angle profile based on the envelope of the RF-pulse in time domain using solutions of the Bloch equations. The second one is to measure the flip angle distribution directly in a phantom. Both methods were compared to each other.

3.4.1 Slice Profile Simulation using Bloch Equations

For on-resonant excitation (non-slice selective excitation) the flip angle can be described by a linear relation between the gyromagnetic constant γ and the applied B_1-field. α is proportional to the area under the B_1 RF-envelope, referring to [10, p.69]. T_{RF} is the excitation time, where the RF-field is switched on and B_1 is the RF modulation envelope of the RF-field. The derivation of Eq. 3.31 is given in [10, p.69–71]

$$\alpha = \gamma \int_{t=0}^{T_{RF}} B_1(t)\, dt \tag{3.31}$$

For slice selective excitation, as it is used in the TrueFISP_CV sequence, on-resonant excitation only holds for spins located exactly at the center of the slice, because the applied gradient is zero there. All other spins are excited off-resonant. In this case the slice profile can be approximated by the Fourier transform of the B_1-envelop, which is known as the "small flip angle approximation". This approximation is based on a solution of the Bloch equations out of [10, p.72] with the complex transverse magnetization $M_t = M_x + iM_y$:

$$M_t(T_{RF}) = i\gamma e^{-i\Delta\omega T_{RF}} \int_{t=0}^{T_{RF}} M_z(t)\, B_1(t)\, e^{i\Delta\omega t} dt \tag{3.32}$$

Eq. 3.32 is simplified by the assumption, that $M_z(t) \approx M_0$, which is only valid for small flip angles. The limits of the integral can be extended to $-\infty$ to ∞ because the B_1-field is only switch on during the excitation and Eq. 3.32 approximates to:

$$M_t(T_{RF}) \approx i\gamma M_0 e^{-i\Delta\omega T_{RF}} \int_{t=-\infty}^{\infty} B_1(t)\, e^{i\Delta\omega t} dt \tag{3.33}$$

Eq. 3.33 is the inverse Fourier transform of the applied B_1-field, which is also a linear relationship between α and B_1. As stated in [10, p.73], this approximation holds for flip angles up to about $\alpha = 30°$. Phenomenologically, the Fourier approximation can be explained using signal theory. Due to the linear gradient field, the resonance frequency varies linearly along the slice and the flip angle profile can be seen as the spectrum of the RF-pulse. Nevertheless, the relation between flip angle profile and B_1-field becomes

more and more nonlinear with increasing flip angle α. This phenomenon is described as the non-linearity of the Bloch equations [10]. Unfortunately, this expression is a little bit confusing, because the Bloch equations are linear and only the relationship between flip angle α and B_1 becomes non-linear.

Hard Pulse Approximation: To model slice selective excitation exactly, a much more sophisticated model is needed. In Figure 3.5, the field configuration for off-resonant excitation is depicted. The precession of the magnetization vector takes place around a effective magnetic field B_e, which is the vectorial sum of B_1 and ΔB_0 in the rotating frame. Due to simplicity and without loss of generality let us assume the excitation takes place in the x-y plane, so a gradient along the z-direction is applied. For any other slice, the coordinate system is rotated, such that the excited slice lies in the x-y plane and the expressions below are valid again. Furthermore, it is assumed that the change in the static field ΔB_0 only comes from the applied gradient. Local field inhomogeneities are neglected.

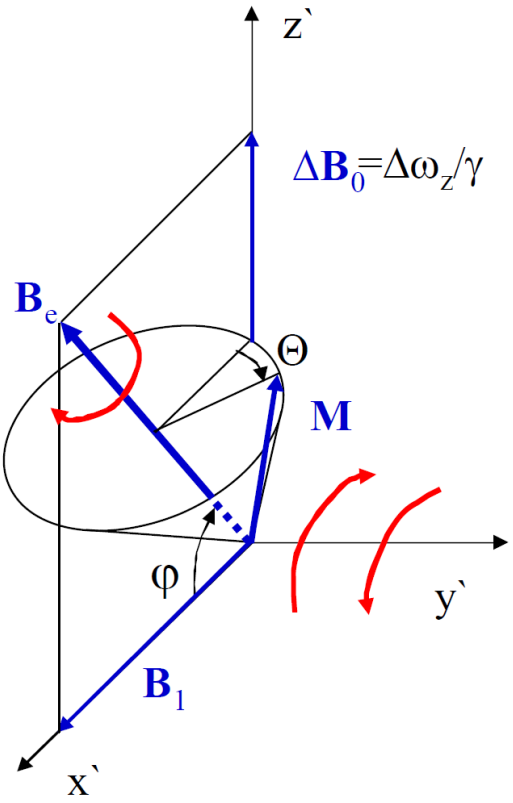

Figure 3.5: Field configuration for an off-resonant excitation. The precession of the magnetization vector is performed around an effective magnetic field which is the vecotrial sum of B_1 and ΔB_0. The precession angle around B_e is given by Θ and the direction of B_e is given by the angle φ to the transverse plane. This figure is taken from [22].

The value of ΔB_0 and the resonance offset $\Delta\omega_z$ changes linearly along the z-direction according to the applied gradient.

$$\Delta B_0(z) = z \cdot G_z \tag{3.34}$$

$$\Delta\omega_z(z) = \gamma \cdot \Delta B_0 = \gamma \cdot z \cdot G_z \tag{3.35}$$

φ describes the angle between the direction of the effective field B_e and the x-axis. This assumes that the B_1-field is applied along the x-axis of the rotating frame. This can be assumed without loss of generality, because the coordinate system can be rotated in a way, so that the B_1-field is really in the direction of the x-axis. The angle φ and the effective magnetic field $|B_e|$ are calculated by:

$$\varphi = \arctan\left(\frac{\Delta B_0}{B_1}\right) \tag{3.36}$$

$$|B_e| = \sqrt{\Delta B_0^2 + B_1^2} \tag{3.37}$$

The precession angle Θ around the effective field can be calculated according to Eq. 3.31, assuming constant B_e in the time interval Δt.

$$\Theta = \gamma |B_e(t)| \Delta t \tag{3.38}$$

To calculate a flip angle profile with this approach, the so called "hard pulse approximation" is used ([10, p. 44]). For this it is necessary to discretize the RF-envelope in constant time steps Δt and assuming the amplitude is constant during each time step. The change in the static field $\Delta B_0(z)$ is also discretized into sub-slices with a width of Δz and a constant value of ΔB_0. The sub-slices are assumed to be independent of each other and the following calculations are performed for each of them separately. Let us consider the magnetization vector for only one sub-slice with a certain value of ΔB_0 and a resulting $\Delta\omega$. The calculation starts with an arbitrary orientation of the magnetization vector. For the flip angle profile calculations in Section 4.1, magnetization starts in thermal equilibrium. The progression of the magnetization vector during excitation can be described, by applying Eq. 3.39 iteratively for each step of Δt. Normally, B_1 is not constant and the values for φ and Θ have to be recalculated in every time step. The idea behind Eq. 3.39 is to rotate the effective field B_e into the x-direction, perform the rotation by Θ around the x-axis and rotate back to the initial direction of B_e. This is a standard procedure to perform a rotation around an arbitrary axis by applying standard rotation matrices.

$$\vec{M}_{n+1} = \mathbf{R}_y(-\varphi) \cdot \mathbf{R}_x(-\Theta) \cdot \mathbf{R}_y(\varphi) \cdot \vec{M}_n \tag{3.39}$$

The resulting flip angel $\alpha(z)$ can be easily determined by calculating the angle of the

resulting magnetization vector in each sub-slice with respect to the positive z-direction.

The RF-envelope can be exported out of the sequence development environment Multi-IDEA, which is already discretized with a Δt of $1\mu s$. This is the same way as it is applied on the scanner. As you can see in Figure 3.6, the RF-signal is given as the voltage U_{coil} which is applied to the transmit coil generating the desired B_1-field. The real B_1-field can be calculated using Eq. 3.40, assuming on-resonance in the center of the slice (no gradient) and that the B_1-field is directly proportional to the applied voltage.

$$B_1 = \alpha_{nom} \frac{U_{coil}(t)}{\gamma \int_{t=0}^{T_{RF}} U_{coil}(t)\, dt} \tag{3.40}$$

For the calculation, a gradient of $10mT/m$ was assumed and the z-direction was simulated from $-20mm$ to $+20mm$ with a thickness Δz of $10\mu m$. The TrueFISP_CV sequence used for parameter estimation allows adjusting three different types of RF-pulses ("Fast", "Normal" and "Low SAR"). The slice profiles for all three types were simulated and compared to each other.

3.4.2 Slice Profile Measurement

The sequence to measure the flip angle profile was developed at the institute and is based on a GRE-sequence. The sequence diagram is depicted in Figure 3.6. The main difference to standard imaging sequences is that the slice selection gradient and the readout gradient are applied in the same direction, in this particular case it is the z-direction. The phase encoding steps are performed as usual. Furthermore, the sequence was modified, such that the same RF-pulse is used as in the TrueFISP_CV sequence. With this special acquisition scheme, the intensity along the slice direction was imaged.
The slice profile was measured in a homogeneous phantom to avoid intensity modulations due to different relaxation times or different spin densities in tissue. It was measured in a cylindrical phantom filled with distilled water doped with 3.75g $NiSO_4$ x $6H_2O$ + 5g NaCl per 1000g H_2O. The phantom has a T_1 of about $107ms$ and a T_2 of about $77ms$. The TR was set to $500ms$ to reach complete relaxation before each excitation. The measurements were performed for different flip angles form 10° to 180° and with a slice thickness of 5mm, 8mm and 20mm, on a Siemens MAGNETOM Skyra 3T System, Erlangen Germany. The 20 channel head and neck coil from Siemens was used.

Unfortunately, the complete magnetization vector cannot be measured, only a signal proportional to the magnitude of the transverse magnetization, the intensity profile $S_{meas}(z)$, which is proportional to the sine of the actual flip angle $\alpha(z)$, is measured.

Figure 3.6: Sequence diagram for a GRE based sequence to measure the intensity profiles along the slice direction over two TR-periods. To achieve this, the readout and slice selection gradient are applied in the same direction. Furthermore, the same RF-pulse is used as in the TrueFISP_CV sequence. The diagram was generated by the sequence development environment MultiIDEA in the version VD13.

This intensity profile was reconstructed out of the central k-space line in frequency encoding direction using the one dimensional Fourier transform. The flip angle profile $\alpha(z)$, for nominal flip angles $\alpha_{nom} < 90°$, can be easily calculated by the arcsin operation and normalizing the intensity profile to the nominal flip angle at the intensity maximum:

$$\alpha(z) = \arcsin\left(\frac{S_{meas}(z)}{\max(S_{meas}(z))}\sin(\alpha_{nom})\right) \tag{3.41}$$

Another more accurate method would be to normalize the intensity profile to the true flip angle $\alpha_{max,true}$ at the maximum of $S_{meas}(z)$ due to variations in B_1. The true flip angle can be determined using the DAM. Both methods were implemented, but the flip angle profiles used for the reconstruction are normalized to the nominal flip angle α_{nom}, because flip angle variations due to B_1 depend on the load of the coil and cannot be pre-estimated [23]. Therefore, B_1-correction can only be applied individually for each measurement in the reconstruction procedure.

For nominal flip angles $\alpha_{nom} > 90°$ some assumptions are necessary to calculate the flip angle profile, because $S_{meas}(z)$ reaches a local minimum around the point with the maximum flip angle due to the $\sin(\alpha(z))$ dependency. Therefore, the intensity profile $S_{meas}(z)$ was split into four regions, the region to the left of the first maximum (1), the region between the first maximum and the local minimum (2), the region between the minimum and the second maximum (3) and the region to the right of the second maximum (4), as it is shown in Figure 3.7. The first and the second maximum were normalized such that the flip angle is 90° there. Because of the knowledge that the nominal flip angle has to be $\alpha_{nom} > 90°$, regions 1 and 4 are assumed to have a flip angle profile $\alpha(z) < 90°$ and region 2 and 3 are assumed to have a flip angle profile $\alpha(z) > 90°$. The flip angle profiles were calculated according to Eq. 3.42 – 3.45.

$$\alpha(z \leq z_1) = \arcsin\left(\frac{S_{meas}(z \leq z_1)}{S_{meas}(z_1)}\right) \tag{3.42}$$

$$\alpha(z_1 < z \leq z_2) = 180° - \arcsin\left(\frac{S_{meas}(z_1 < z \leq z_2)}{S_{meas}(z_1)}\right) \tag{3.43}$$

$$\alpha(z_2 < z \leq z_3) = 180° - \arcsin\left(\frac{S_{meas}(z_2 < z \leq z_3)}{S_{meas}(z_3)}\right) \tag{3.44}$$

$$\alpha(z > z_3) = \arcsin\left(\frac{S_{meas}(z > z_3)}{S_{meas}(z_3)}\right) \tag{3.45}$$

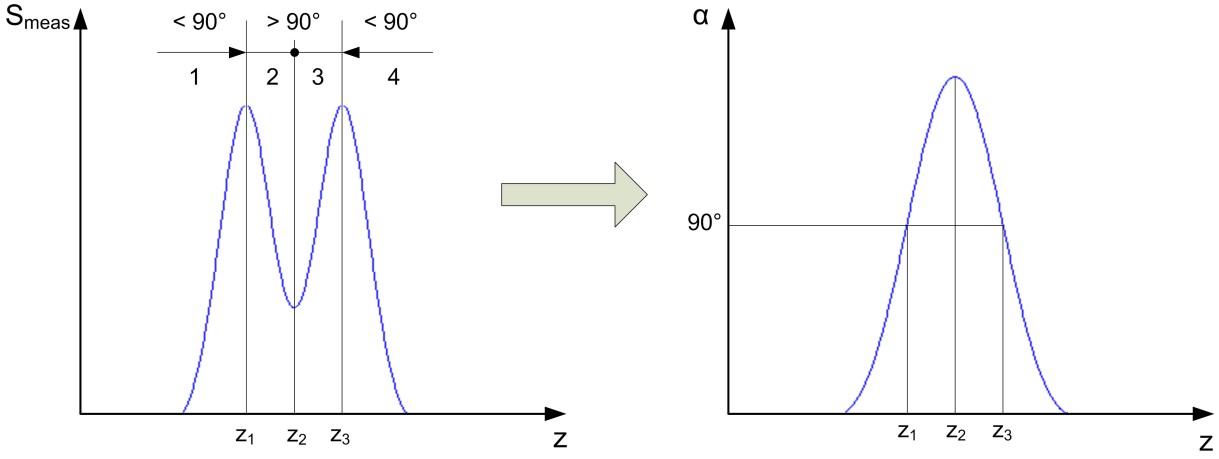

Figure 3.7: Left: Measured intensity profile with two maxima. To the left of the first maximum and to the right of the second maximum the flip angle profile $\alpha(z) < 90°$, between the two maxima the flip angle profile $\alpha(z) > 90°$. Right: Complete flip angle profile out of the measured intensity profile

3.5 Modeling of Magnetization Transfer Effects

In comparison to water phantoms, hydrogen atoms appear in biological tissue in different chemical compounds. Beside the hydrogen bound in water (free pool), hydrogen atoms are also bound in macromolecules, like proteins or lipids and proteins usually are covered by a hydration layer. Macromolecules and hydration layer are summarized as bound or restricted pool fraction. Depending on this chemical surroundings, or better, the mobility of the bounded molecules the specific relaxation times are completely different. Usually, spins of hydrogen atoms in the restricted pool have a much broader absorption spectrum as it appears in the free pool. This broader spectrum leads to a much shorter T_2 value. However, the dynamics of these different spins cannot be modelled independently, because there is an exchange between them. Therefore, the observed effects of signal attenuation are called magnetization transfer (MT). The effects of MT can be described using a two pool model as it is shown in Figure 3.8 ([29]).

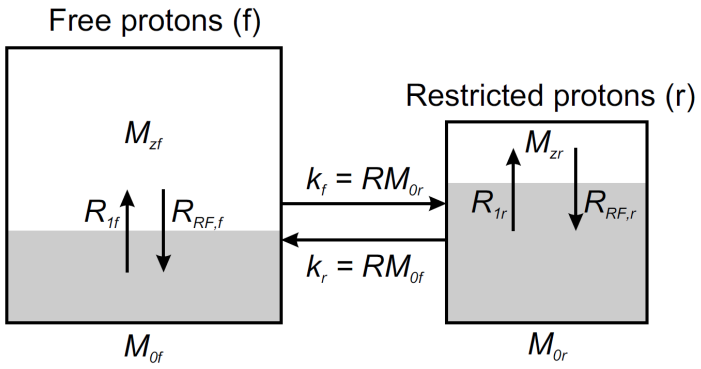

Figure 3.8: Schematic illustration of the two pool model, where the shaded areas represent the saturated part of the particular pool, out of [29].

Referring to [29], the mathematical description of this model can be done using coupled Bloch equations. Therefore, the previously described Bloch equations are set up for both pools, extended by a coupling term using first order exchange kinetics in each component of the magnetization, which is described by the fundamental rate constant R. The directional exchange is modelled by first order rate constants k_r and k_f. The index f refers to the free and the index r to the restricted pool.

$$k_f = RM_{0,r} \tag{3.46}$$

$$k_r = RM_{0,f} \tag{3.47}$$

This yields 6 coupled ODEs, one for each magnetization component in each pool. Because of the very short T_2 value in the restricted pool ($T_{2,r} \approx 10\mu s$ [29]) its transverse magnetization ($M_{x,r}$ and $M_{y,r}$) is assumed to be zero all the time. Also the exchange in the

transverse magnetization can be neglected, because any coherence is destroyed due to the very short T_2 time [29]. This will simplify the set of equations to 4 coupled ODE, where it is assumed that the RF-pulse is applied along the x-direction and no off-resonances appear. $R_{1,r}$ and $R_{1,f}$ are the relaxation rates of the bound and free pool respectively ($R_{1,r,f} = 1/T_{1,r,f}$).

$$\frac{dM_{x,f}}{dt} = -\frac{M_{x,f}}{T_{2,f}} \tag{3.48}$$

$$\frac{dM_{y,f}}{dt} = -\frac{M_{y,f}}{T_{2,f}} + \omega_1(t) M_{z,f} \tag{3.49}$$

$$\frac{dM_{z,f}}{dt} = \frac{M_{0,f} - M_{z,f}}{T_{1,f}} - k_f M_{z,f} + k_r M_{z,r} - \omega_1(t) M_{y,f} \tag{3.50}$$

$$\frac{dM_{z,r}}{dt} = \frac{M_{0,r} - M_{z,r}}{T_{1,r}} + k_f M_{z,f} - k_r M_{z,r} - W(\Delta\omega \to 0, t) M_{z_r} \tag{3.51}$$

With each excitation the restricted pool is also affected, thus partially saturated. The saturation in the restricted pool is modelled by a time dependent mean saturation rate $\langle W(\Delta\omega)\rangle$ according to [30]. ω_1 is the angular frequency due to B_1 and T_{RF} is the duration of the RF-pulse.

$$\langle W(\Delta\omega)\rangle = \frac{\pi}{T_{RF}} \int_0^{T_{RF}} \omega_1^2(t)\, dt G(\Delta\omega) \tag{3.52}$$

The function $G(\Delta\omega)$ represents the absorption line shape. According to [30] the Super-Lorentzian line is most appropriate to describe absorption in tissue.

$$G(\Delta\omega) = \int_0^1 \sqrt{\frac{2}{\pi}} \frac{T_{2,r}}{\mid 3u^2 - 1 \mid} e^{-2\left(\frac{2\pi\Delta\omega T_{2,r}}{3u^2-1}\right)^2} du \tag{3.53}$$

Due to the singularity for $\Delta\omega = 0$, the function was solved by an asymptotic approximation with $T_{2,r} = 12\mu s$ in [30]. This yields to a value of $G(0) = 1.4 \cdot 10^{-5} s$. An analytic solution of the coupled Bloch equations (Eq. 3.48 – 3.51) would be very complex. In [30], a simplified solution for the bSSFP sequence is presented and its validity has been proved. This solution is based on the assumption that relaxation and exchange can be neglected during excitation as it is done by modelling the bSSFP without MT. Furthermore, it is assumed that the exchange can be decoupled from the relaxation, which is only true, if the size of both fractions does not change during one interval of TR. If these conditions are satisfied, the exchange can be described by an additional matrix operation $\mathbf{D}(t)$. Furthermore, it is assumed, that the x-component of the magnetization is zero, because of the RF-pulse in x-direction and the on-resonance assumption. The magnetization vector can be reduced to the dimension of three, describing the y-component of the free pool and the z-components of both pools.

$$\vec{M} = \begin{pmatrix} M_{y,f} \\ M_{z,f} \\ M_{z,r} \end{pmatrix} \tag{3.54}$$

However, the rotation and relaxation matrices have to be adapted as it is shown in Eq. 3.57 – 3.60. The saturation term of the bound pool is included to the rotation matrix $\mathbf{R}_x(\alpha, T_{ex})$ which models the excitation as a rotation around the x-axis in the free pool. According to Eq. 3.4, the magnetization update can be written as:

$$\vec{M}_{j+1} = \mathbf{D}(TE)\left(\mathbf{E}_{TE}\mathbf{R}_x(\alpha, T_{ex})\,\mathbf{R}_z(\pi)\,\mathbf{D}(TE)\left(\mathbf{E}_{TE}\vec{M}_j + \vec{e}_{TE}\right) + \vec{e}_{TE}\right) \tag{3.55}$$

$$\mathbf{D}(TE) = \frac{1}{F+1}\begin{pmatrix} F+1 & 0 & 0 \\ 0 & 1+Fe^{-(F+1)k_r \cdot TE} & 1-e^{-(F+1)k_r \cdot TE} \\ 0 & F-Fe^{-(F+1)k_r \cdot TE} & F+e^{-(F+1)k_r \cdot TE} \end{pmatrix} \tag{3.56}$$

$$\mathbf{E}_{TE} = \begin{pmatrix} e^{-\frac{TE}{T_{2,f}}} & 0 & 0 \\ 0 & e^{-\frac{TE}{T_{1,f}}} & 0 \\ 0 & 0 & e^{-\frac{TE}{T_{1,r}}} \end{pmatrix} \tag{3.57}$$

$$\vec{e}_{TE} = \begin{pmatrix} 0 \\ M_{0,f}\left(1-e^{-\frac{TE}{T_{1,f}}}\right) \\ M_{0,f}\left(1-e^{-\frac{TE}{T_{1,r}}}\right) \end{pmatrix} \tag{3.58}$$

$$\mathbf{R}_x(\alpha, T_{RF}) = \begin{pmatrix} \cos(\alpha) & -\sin(\alpha) & 0 \\ \sin(\alpha) & \cos(\alpha) & 0 \\ 0 & 0 & e^{-\langle W(\Delta\omega \to 0)\rangle T_{RF}} \end{pmatrix} \tag{3.59}$$

$$\mathbf{R}_z(\pi) = \begin{pmatrix} -1 & 0 & 0 \\ 0 & 1 & 0 \\ 0 & 0 & 1 \end{pmatrix} \tag{3.60}$$

F is defined as the ration between the whole restricted and the whole free pool magnetization in %.

$$F = \frac{M_{0,r}}{M_{0,f}} \tag{3.61}$$

The rate constants k_r and k_f are related by:

$$k_r = \frac{k_f}{F} \tag{3.62}$$

3.6 Data Acquisition and Analysis

3.6.1 Measurements

The measurements were performed on 6 different phantoms, and in vivo. One of the used phantoms consists of agar gel which has a ratio of T_2/T_1 in a practicable range. The other five phantoms were water phantoms doped with 0.125, 0.25, 0.5, 1 and 2mM Gadolinium, which is a contrast agent and reduces T_1 and T_2. Furthermore, the ratio of T_2/T_1 of these phantoms is very close to one and the higher Gd concentrations result in a very short value of T_1. Therefore, these phantoms were used to demonstrate the limitations of the quantification method. In vivo measurements were performed in the brain of 3 healthy volunteers. All measurements were performed on a Siemens MAGNETOM Skyra 3T System, Erlangen Germany. The agar phantom was measured by a single channel ^{1}H 123MHz mouse coil from RAPID Biomedical GmbH, Rimpar/Germany with a diameter of ⌀3.5cm, which uses the Siemens Tim Coil Interface 3T for the connection to the scanner. The Gd-doped water phantoms and the in vivo measurements were performed using the 20 channel Siemens Head/Neck 20 A 3T Tim Coil, Erlangen Germany.

All phantom measurements were performed using a resolution of 64x64 pixel with a FOV of 70mm for the agar phantom and a rectangular FOV of 100mm and only 60% in phase encoding direction to reduce scan time for the Gd-doped phantoms. For the in vivo measurements, a resolution of 128x128 with a FOV of 200mm was used. The TrueFISP_CV sequence was applied in a single slice acquisition with a slice thickness of 5mm. A Cartesian acquisition trajectory and the "Normal"-type RF-pulse was used for all measurements. To enable the inversion recovery, it is necessary to choose the option "Cine = On" and "TI Scout" as magnetization preparation. The sequence was triggered using the external trigger mode and using the trigger simulator provided by the *IDEA cmd tool*, where the trigger period was set to 4000ms. The acquisition window was set to $t_{acq} = 3900ms$ and the number of trigger pulses between two inversions N_{trig} was set to 3, which led to a waiting time between the last excitation and the following inversion of 8.1s. All acquisitions were performed with 8 or 16 phase encoding steps (N_{seg}). For the complete acquisition of a 128x128 matrix and 16 phase encoding steps, 8 IR-experiments have to be performed. One experiment needs 12 seconds for $N_{trig} = 3$ which lead to a total acquisition time of 96s. If only 8 phase encoding steps are acquired after one inversion, the total acquisition time doubles to 192s. The TR cannot be adjusted manually, the sequence uses the minimal possible TR depending on the used RF-pulse type and the FOV (duration of the gradient). It is typically in the range of 3.5–5ms. The number of images with different contrast (N_{phase}) depends on the achieved TR and the chosen number of segments.

All reference measurements for T_1 were performed using an IR-SE sequence with a TR of 10s, a TE of 7.7ms and 12 different inversion times (50, 100, 200, 400, 800, 1200, 1600, 2000, 2400, 3000, 4000, and 5000ms). To accelerate the measurement, a turbo factor of 5 and the iPat mode GRAPPA with an acceleration factor of 2 was used. The reference measurements for T_2 in phantoms were performed using a SE sequence with a TR of 10s and different echo times (15, 30, 70, 100, 130, 160, 190, 220, 250, 300, 400, 500, 700 and 1000ms). To accelerate the measurement, a partial Fourier acquisition of 5/8 was selected. The reference measure for T_2 was determined in vivo using a MSE sequence with a TR of 10s and 32 echos were acquired every 10ms starting with a first TE of 10ms. As acceleration method a partial Fourier acquisition of 5/8 was used too.

3.6.2 Data Analysis

The complete data analysis was done with the software package MATLAB (Mathworks Inc., Natick, USA) in the version 7.12.0.

Simulations: The results of the parameter estimation based on simulated data were shown as the error compared to the true value in % for T_1 and T_2, the value of M_0 was normalized to one. The noise analysis was done by adding Gaussian white noise to the simulated signal with zero mean and a standard deviation of 5 or 10% of the highest signal appearing in the simulated transient. The results were plotted as mean and standard deviation over 2000 repetitions for the method of Schmitt. The number of repetitions was reduced to 1000 for the slice profile correction due to the much higher calculation effort.

Measurements: The data analysis for the reconstructed parameter maps was done inside of ROIs which were drawn by hand. The values presented in Section 4 were always calculated as mean and standard deviation inside a particular ROI. It is important that massive outliers were excluded of these ROIs to ensure a meaningful determination of mean and standard deviation. The ROIs especially for the in vivo measurements were not necessarily connected, they were drawn inside the particular tissue, which can be spread over the whole brain. The errors ϵ were always stated as the deviation of the mean inside a particular ROI to the mean inside the same ROI of the corresponding reference measurement.

$$\epsilon = \frac{\overline{T}_{1,2_{quant}} - \overline{T}_{1,2_{ref}}}{\overline{T}_{1,2_{ref}}} \tag{3.63}$$

The data analysis concerning MT-effects was done on the basis of the transient in a single pixel. To compare the simulated and measured data, an attenuation coefficient ΔS_{MT} was defined, which describes the relation between the simulated and the measured steady state signal.

$$\Delta S_{MT} = \frac{S_{sim,ss}}{S_{meas,ss}} \tag{3.64}$$

To compare the difference of the achieved effects in different tissues another coefficient ΔS_{tissue} was defined as the relation of the attenuation coefficients of the compared tissues, especially WM and GM in brain.

$$\Delta S_{tissue} = \frac{\Delta S_{MT_{WM}}}{\Delta S_{MT_{GM}}} \tag{3.65}$$

4 Results

4.1 Flip Angle Profiles

This section describes the simulated flip angle profiles using the discrete Bloch simulation (hard pulse approximation) described in Section 3.4.1 and the measured flip angle profiles in the described phantom. Figure 4.1 depicts a comparison between the Fourier approximation and the discrete Bloch simulation for different nominal flip angles. Figure 4.2 investigates the influence of the different RF-pulse types available in the Siemens TrueFISP_CV sequence. Figure 4.3 illustrates the measured intensity profiles in the phantom for different slice thicknesses. In Figure 4.4, the flip angle profiles calculated out of these intensity profiles are compared to each other. A comparison between measured and simulated flip angle profiles is done in Figure 4.5.

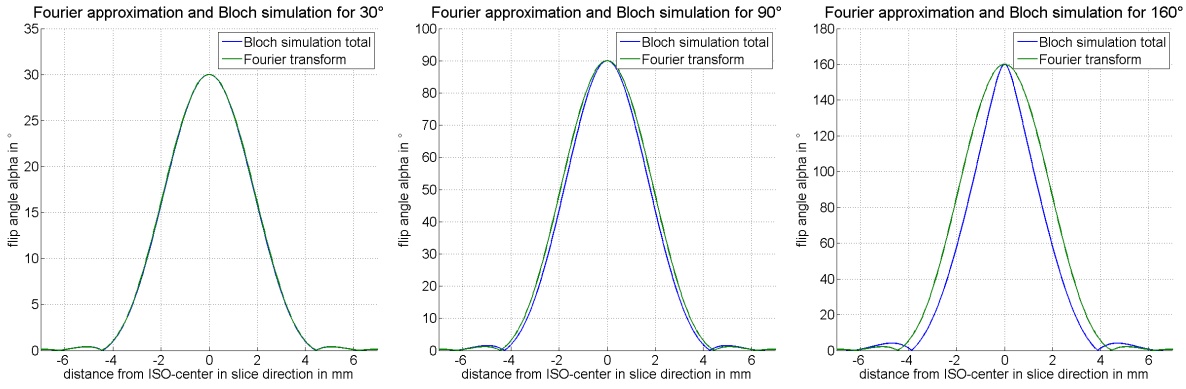

(a) (b) (c)

Figure 4.1: Comparison between the flip angle profile simulated by the Fourier- or "low flip angle" approximation and the descritized Bloch simulation for different nominal flip angles. (a) $\alpha_{nom} = 30°$, (b) $\alpha_{nom} = 90°$, (c) $\alpha_{nom} = 160°$

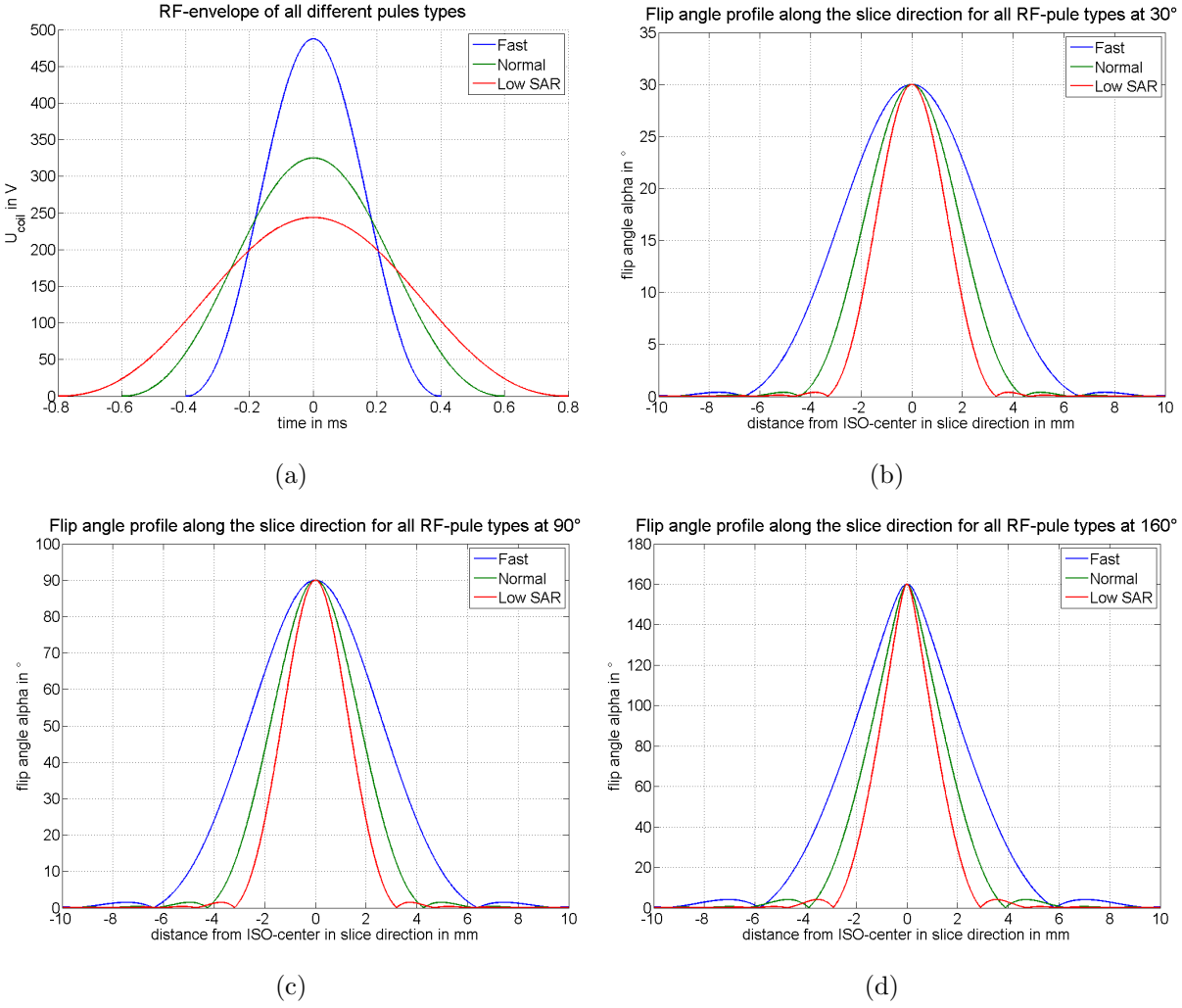

Figure 4.2: (a) Shapes of the RF-envelopes of all adjustable RF-pulse types in the True-FISP_CV sequence. The pulse shapes were exported out of the sequence development environment MultIDEA in the version VB17a. (b), (c) and (d) Simulated flip angle profiles $\alpha(z)$ using the B_1-shapes of (a) and a gradient of $10mT/m$ in z-direction. The simulation was done by the discretized Bloch simulation, for different nominal flip angles of (b) $\alpha_{nom} = 30°$, (c) $\alpha_{nom} = 90°$, (d) $\alpha_{nom} = 160°$.

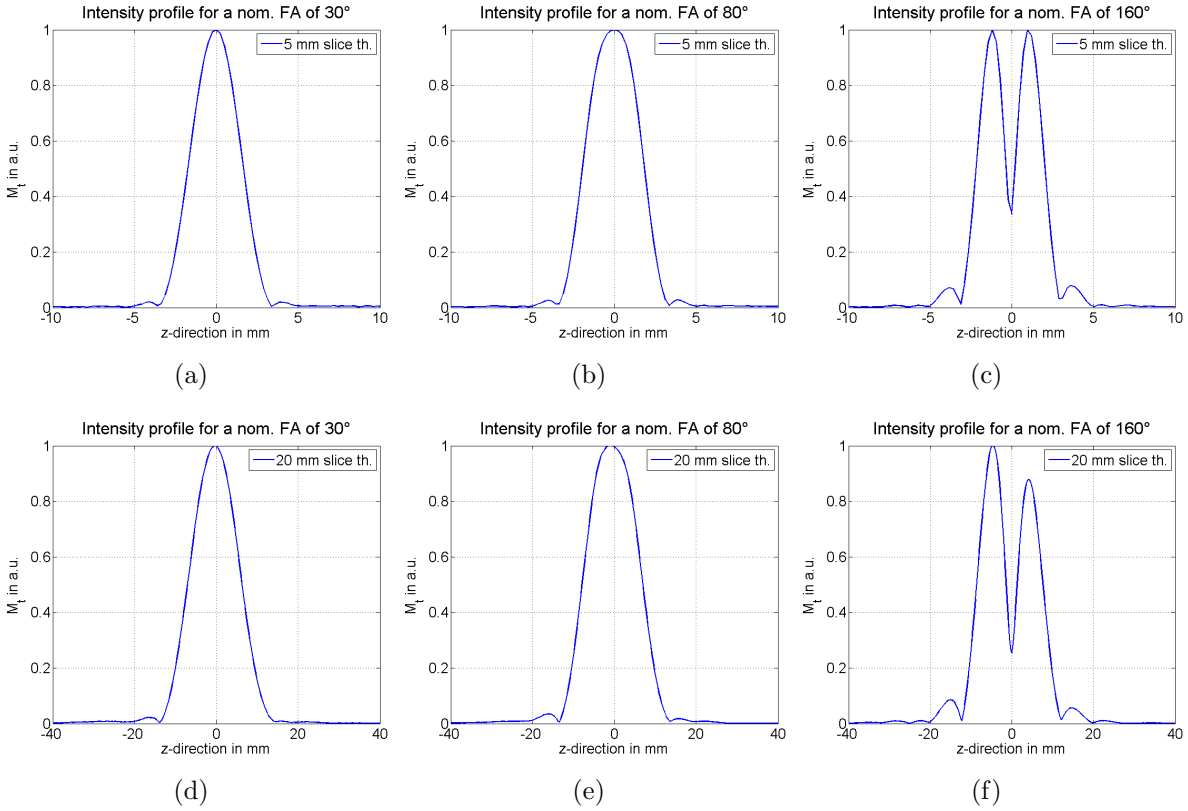

(a) (b) (c)

(d) (e) (f)

Figure 4.3: (a), (b), (c) Measured intensity profile for a slice thickness of 5mm and different nominal flip angles α_{nom}. (a) $\alpha_{nom} = 30°$, (b) $\alpha_{nom} = 80°$, (c) $\alpha_{nom} = 160°$. (d), (e), (f) Measured intensity profile for a slice thickness of 20mm and different nominal flip angles α_{nom}. (d) $\alpha_{nom} = 30°$, (e) $\alpha_{nom} = 80°$, (f) $\alpha_{nom} = 160°$

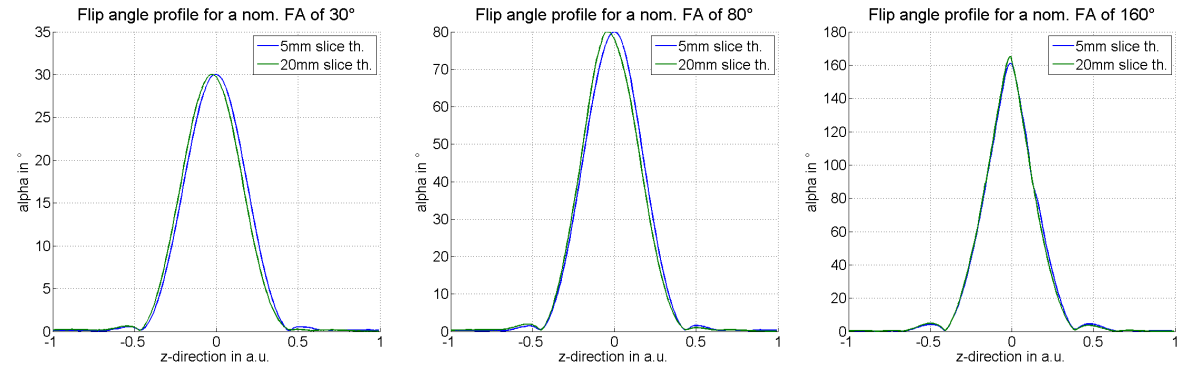

(a) (b) (c)

Figure 4.4: Comparison of measured flip angle profiles $\alpha(z)$ for a slice thickness of 5 and 20mm for different nominal flip angles α_{nom}. Because both flip angle profiles have a different dimension in z-direction, they were normalized to each other. The reference points are the left and the right first zero crossing after the main peak. Because of the normalization, the dimension in z-direction is represented in arbitrary units. (a) $\alpha_{nom} = 30°$, (b) $\alpha_{nom} = 80°$, (c) $\alpha_{nom} = 160°$

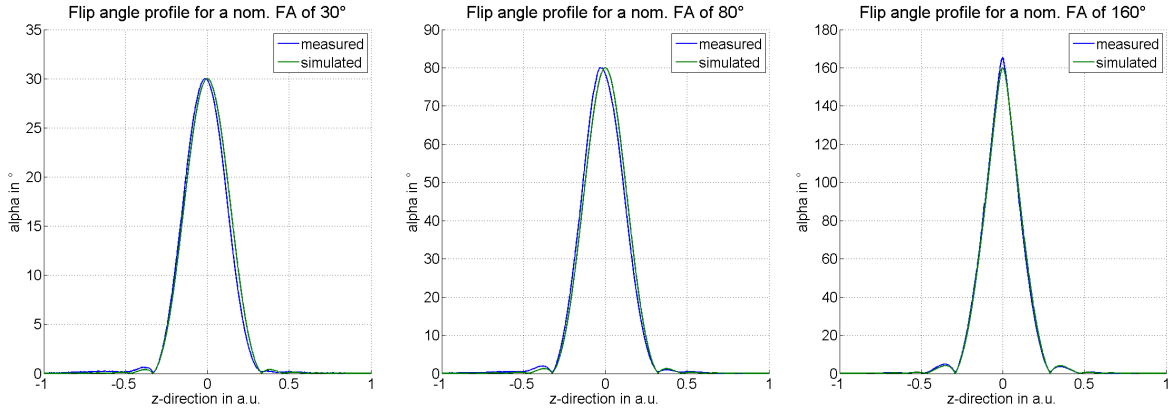

(a) (b) (c)

Figure 4.5: Comparison of measured and simulated flip angle profiles $\alpha(z)$ for different nominal flip angles α_{nom}. Because both flip angle profiles have a different dimension in z-direction, they were normalized to each other. The reference points are the left and the right first zero crossing after the main peak. Because of the normalization, the dimension in z-direction is in arbitrary units. (a) $\alpha_{nom} = 30°$, (b) $\alpha_{nom} = 80°$, (c) $\alpha_{nom} = 160°$

4.2 Simulations Concerning Schmitt-Approach

In this section, the influence of different non-ideal conditions on the parameter quantification using the Schmitt-approach are presented. The measurement data was simulated using the full forward model described in Section 3.1.1. The estimated parameters were plotted against the varied parameter. For T_1 and T_2, the deviation of the true value is shown in %. Because M_0 can only be determined relatively, it was normalized to one. The influence of varying nominal flip angle α_{nom}, varying off-resonance precession angle ϕ, different ratios of T_2 to T_1 and different absolute values of T_1 and T_2 at a constant ratio $T_2/T_1 = 0.5$ were investigated. The quantification error is shown for different flip angle profiles, both preparation methods and using noiseless and noisy data. If nothing else is mentioned, the following parameters were used to simulate the measured data: $T_1 = 1000ms$, $T_2 = 100ms$, $\alpha = 40°$, $TR = 4ms$. For the simulation 6 different flip angle profiles were used. An ideal (rectangular) profile with an infinitely steep transition from zero to α_{nom}, four artificial profiles and the real measured flip angle profile determined with a slice thickness of 5mm. Two flip angle profiles were generated by the Fourier approximation out of a truncated sinc-function, where the deviation to the ideal case is quite small. Two flip angle profiles with Gaussian and triangular shape were used to simulate a heavy deviation from the ideal case. To consider the influence of noise, the quantification was repeated 2000 times, where the simulated signal was corrupted with 10% Gaussian noise. The diagrams show mean and standard deviation over 2000 repetitions.

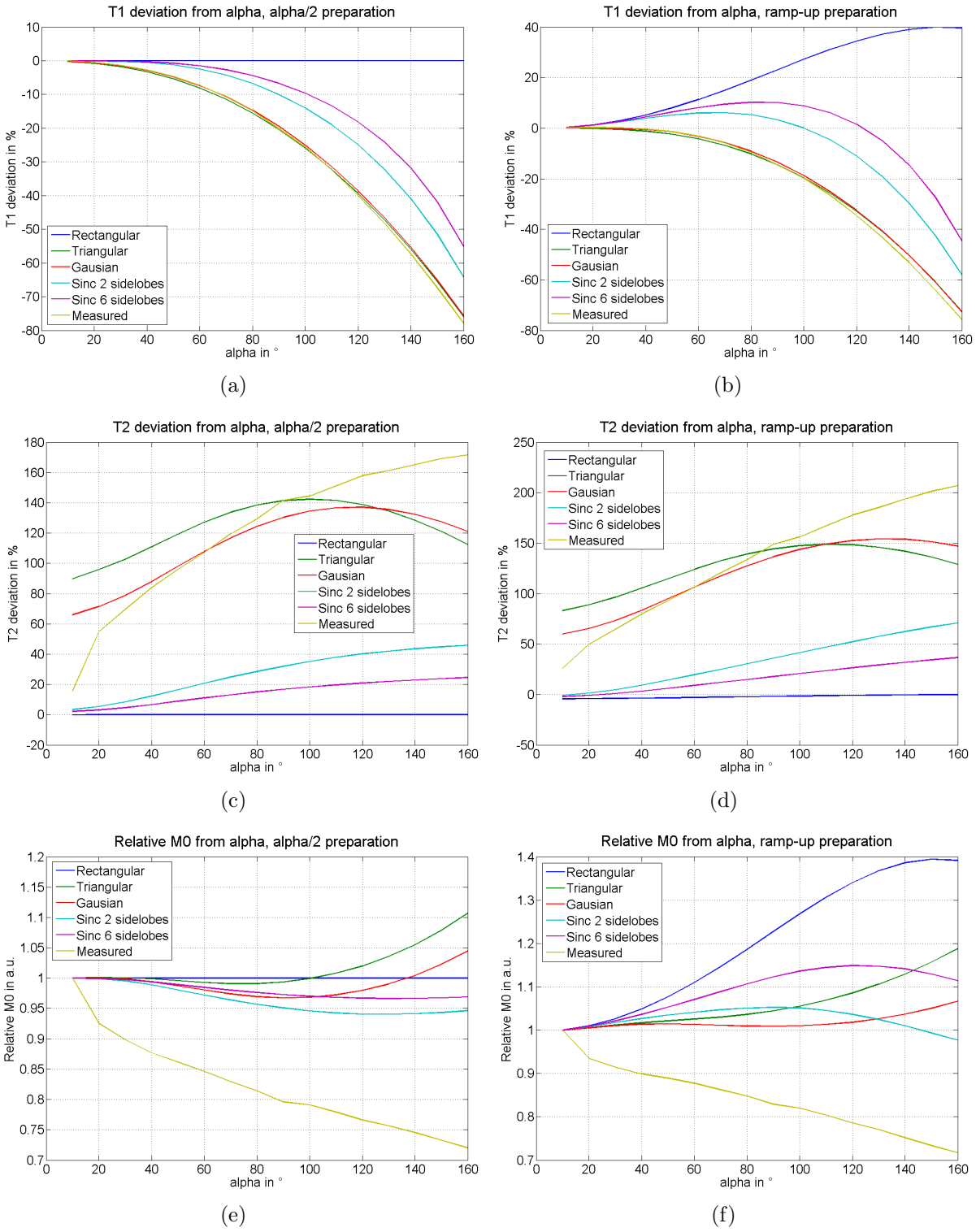

Figure 4.6: The influence of the flip angle on the parameter estimation using the Schmitt-approach for different nominal flip angles α_{nom} is illustrated for 6 different flip angle profiles, without noise, based on simulated data. T_1 and T_2 are shown as the deviation of the real value in % and the value of M_0 was normalized to one. (a), (c), (d) data was simulated using $\alpha/2$ preparation, (b), (d), (e) data was simulated using ramp-up preparation.

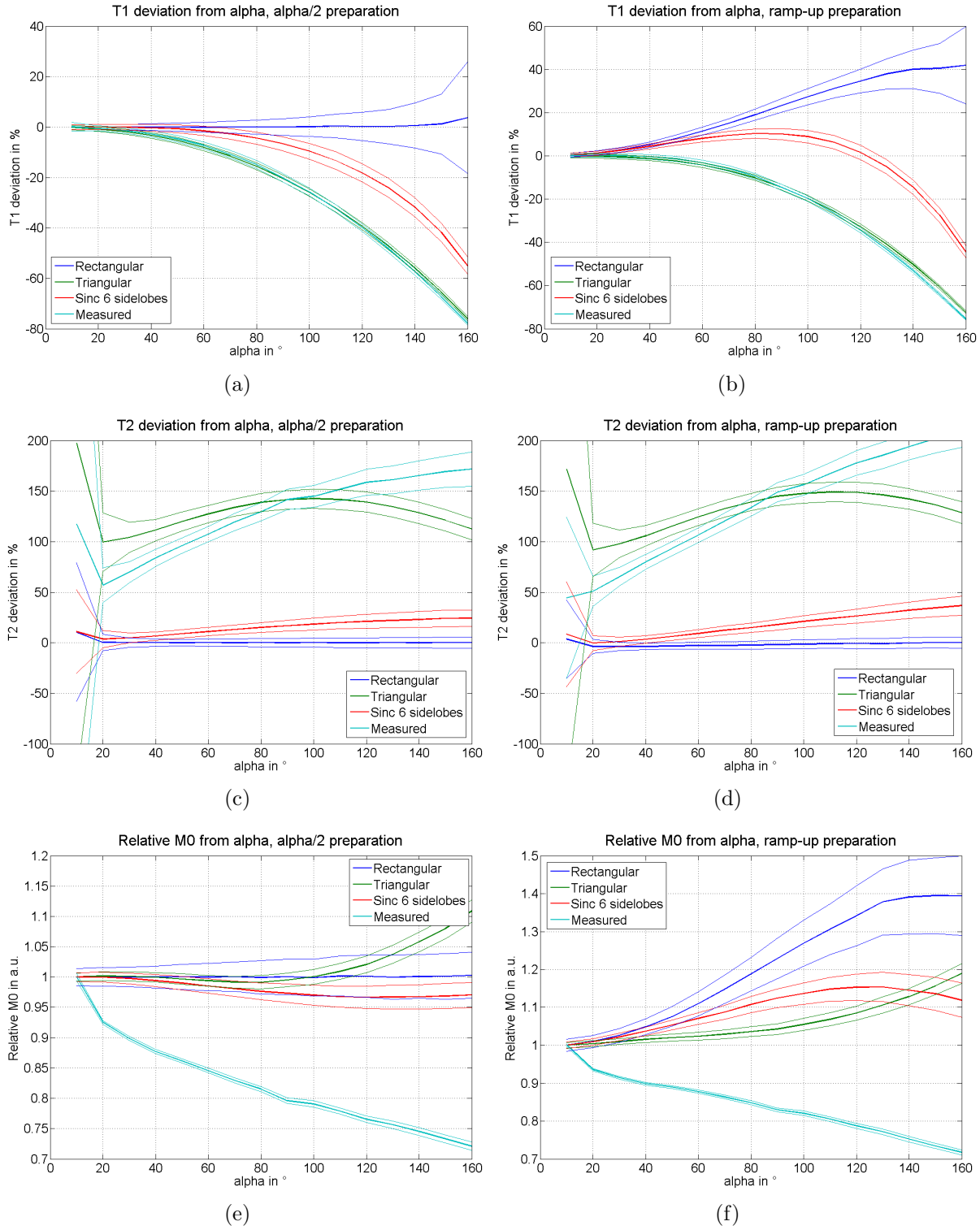

Figure 4.7: The influence on the parameter estimation using the Schmitt-approach for different nominal flip angles α_{nom} is illustrated for 4 different flip angle profiles, with a noise level of 10%, based on simulated data. T_1 and T_2 are shown as the deviation of the real value in % and the value of M_0 was normalized to one. The values here are plotted as mean (broad line) and standard deviation (thin line) over 2000 repetitions. (a), (c), (d) data was simulated using $\alpha/2$ preparation, (b), (d), (e) data was simulated using ramp-up preparation.

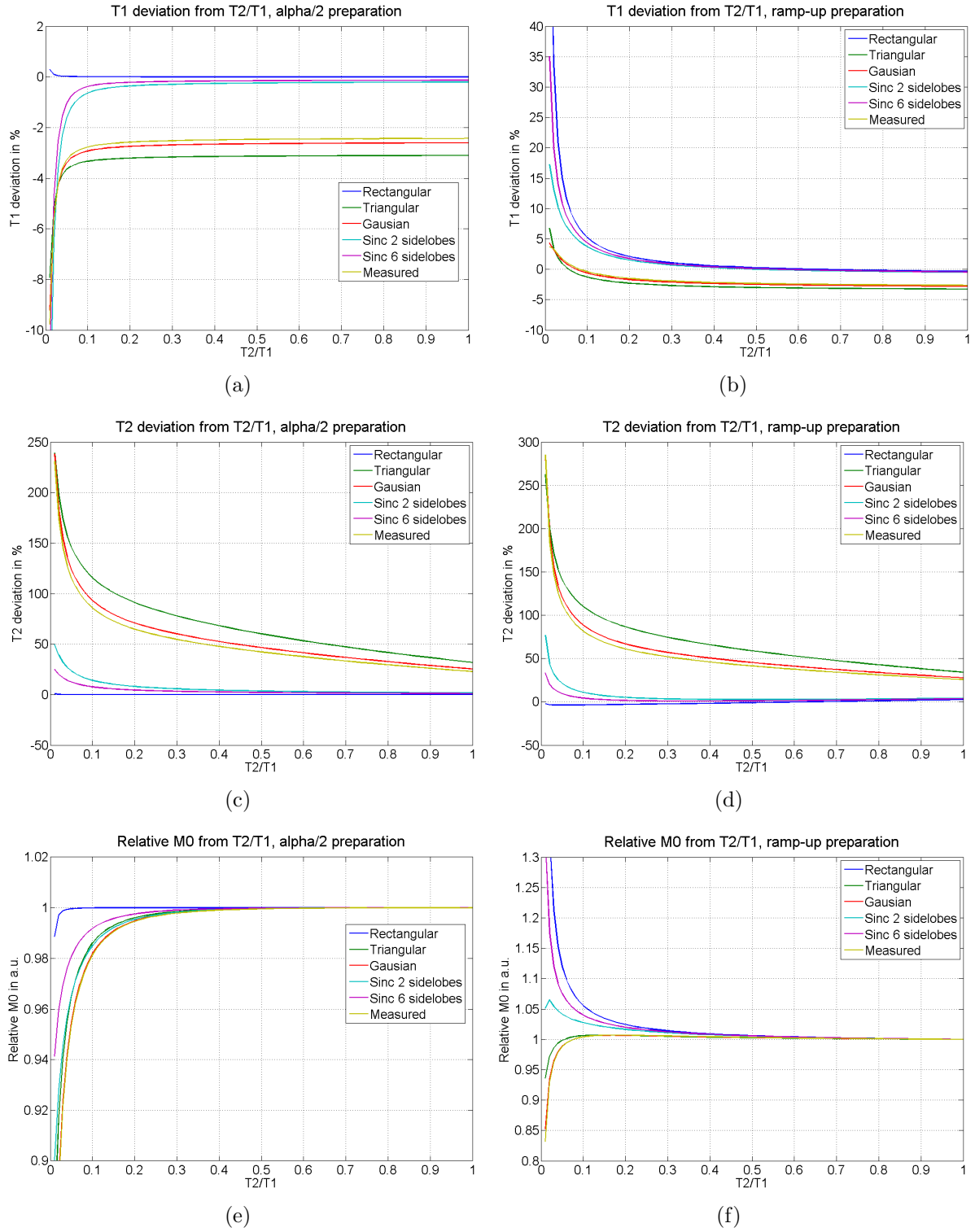

Figure 4.8: The influence on the parameter estimation using the Schmitt-approach for different ratios of T_2/T_1 is illustrated for 6 different flip angle profiles, without noise, based on simulated data. T_2 is varied from 10ms to 1000ms, with a constant value of $T_1 = 1000ms$. T_1 and T_2 are shown as the deviation of the real value in % and the value of M_0 was normalized to one. (a), (c), (d) data was simulated using $\alpha/2$ preparation, (b), (d), (e) data was simulated using ramp-up preparation.

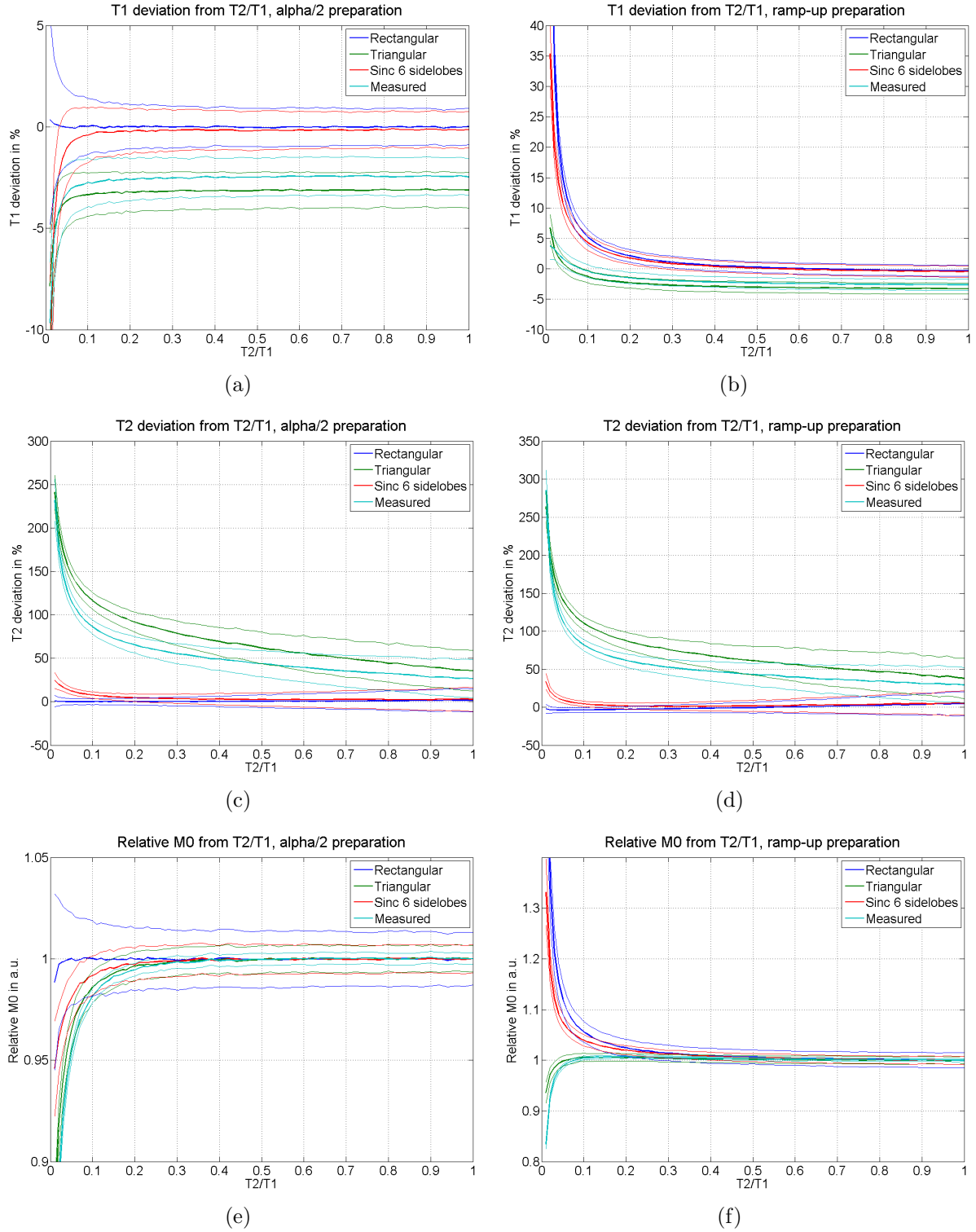

Figure 4.9: The influence on the parameter estimation using the Schmitt-approach for different ratios of T_2/T_1 is illustrated for 4 different flip angle profiles, with a noise level of 10%, based on simulated data. T_2 is varied from 10ms to 1000ms, with a constant value of $T_1 = 1000ms$. T_1 and T_2 are shown as the deviation of the real value in % and the value of M_0 was normalized to one. The values here are plotted as mean (broad line) and standard deviation (thin line) over 2000 repetitions. (a), (c), (d) data was simulated using $\alpha/2$ preparation, (b), (d), (e) data was simulated using ramp-up preparation.

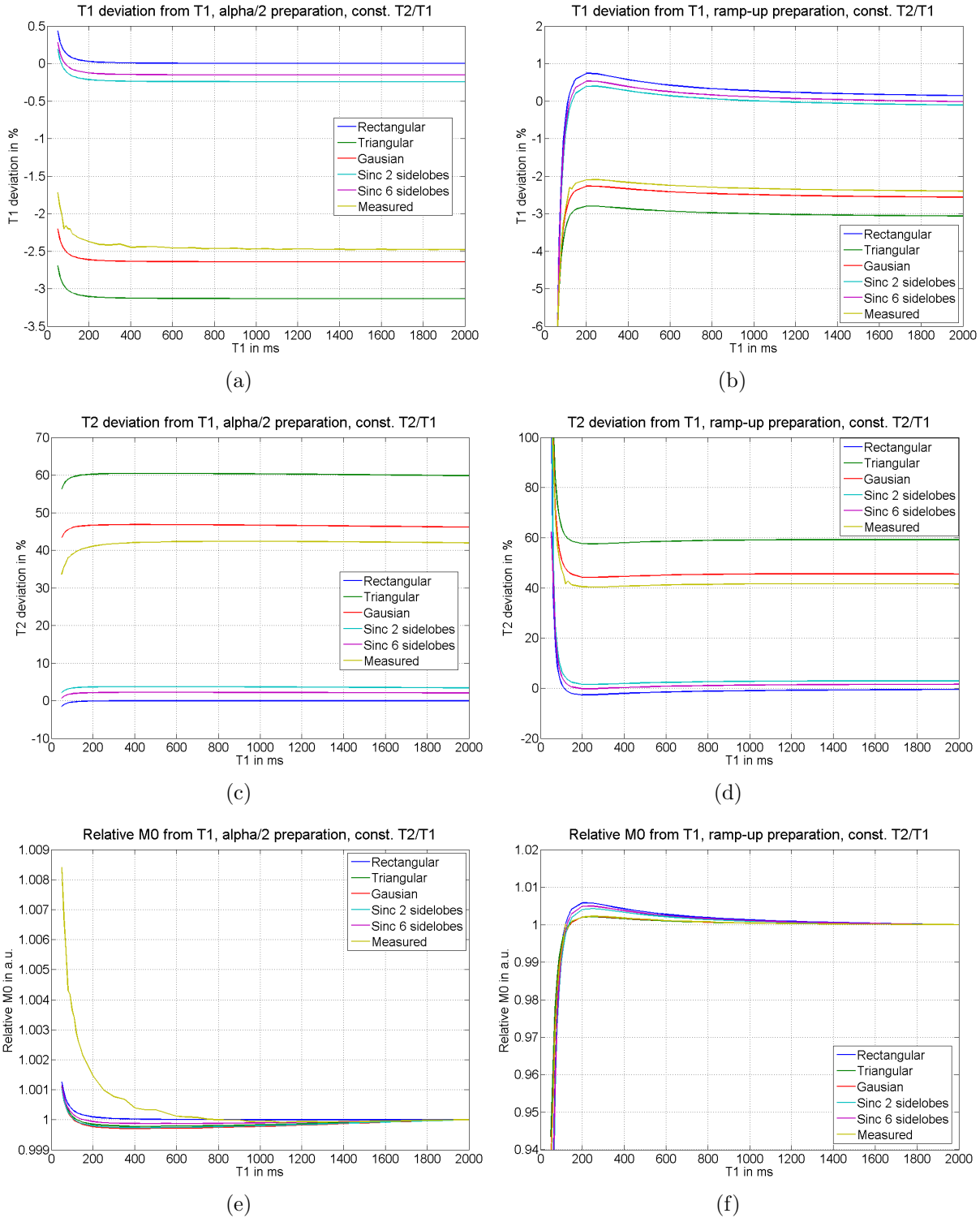

Figure 4.10: The influence on the parameter estimation using the Schmitt-approach for different values of T_1 is illustrated for 6 different flip angle profiles, without noise, based on simulated data. The ratio T_2/T_1 is held constant, with a value of $T_2 = 0.5T_1$. T_1 and T_2 are shown as the deviation of the real value in % and the value of M_0 was normalized to one. (a), (c), (d) data was simulated using $\alpha/2$ preparation, (b), (d), (e) data was simulated using ramp-up preparation.

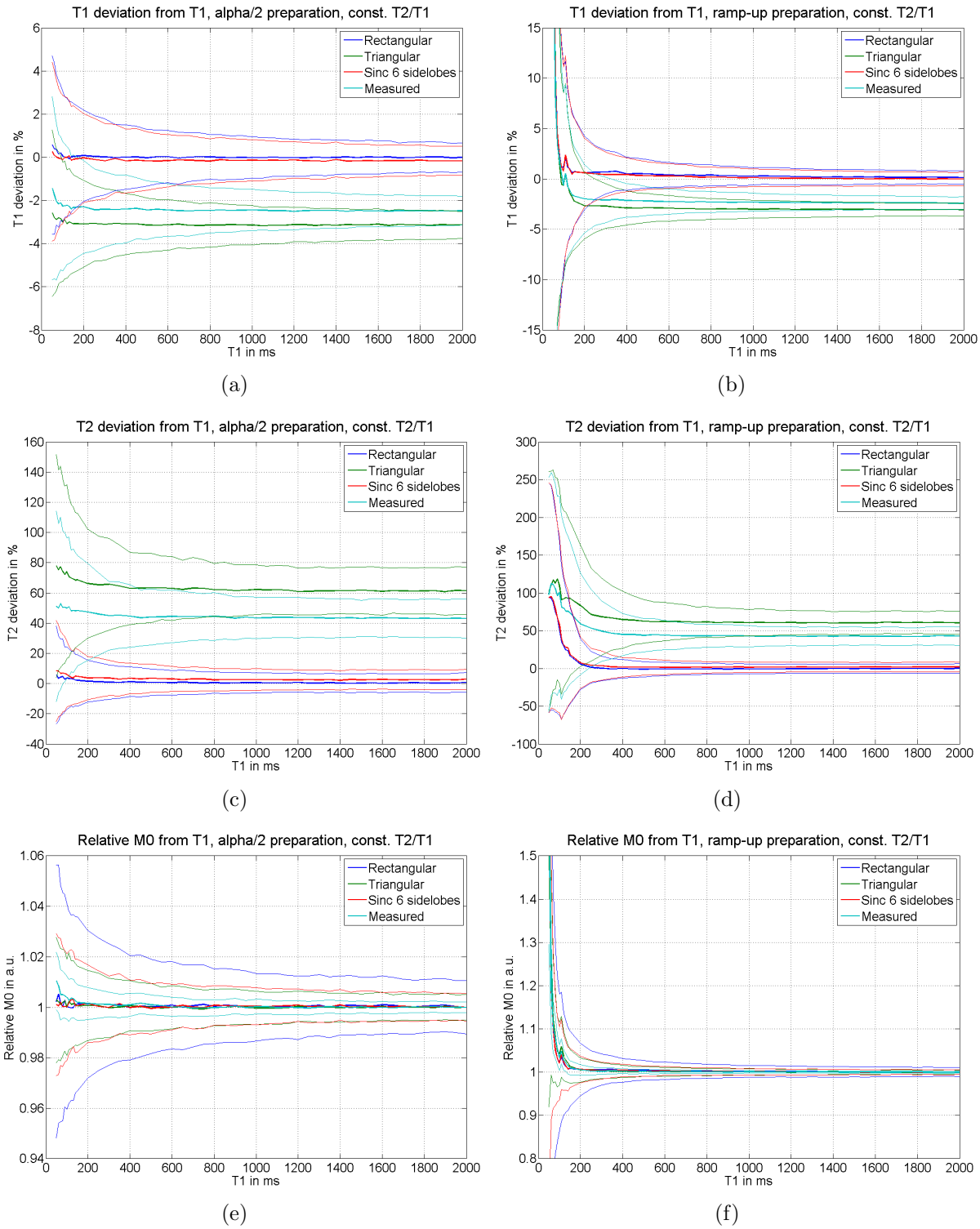

Figure 4.11: The influence on the parameter estimation using the Schmitt-approach for different values of T_1 is illustrated for 4 different flip angle profiles, with a noise level of 10%, based on simulated data. The ratio T_2/T_1 is held constant, with a value of $T_2 = 0.5T_1$. T_1 and T_2 are shown as the deviation of the real value in % and the value of M_0 was normalized to one. The values here are plotted as mean (broad line) and standard deviation (thin line) over 2000 repetitions. (a), (c), (d) data was simulated using $\alpha/2$ preparation, (b), (d), (e) data was simulated using ramp-up preparation.

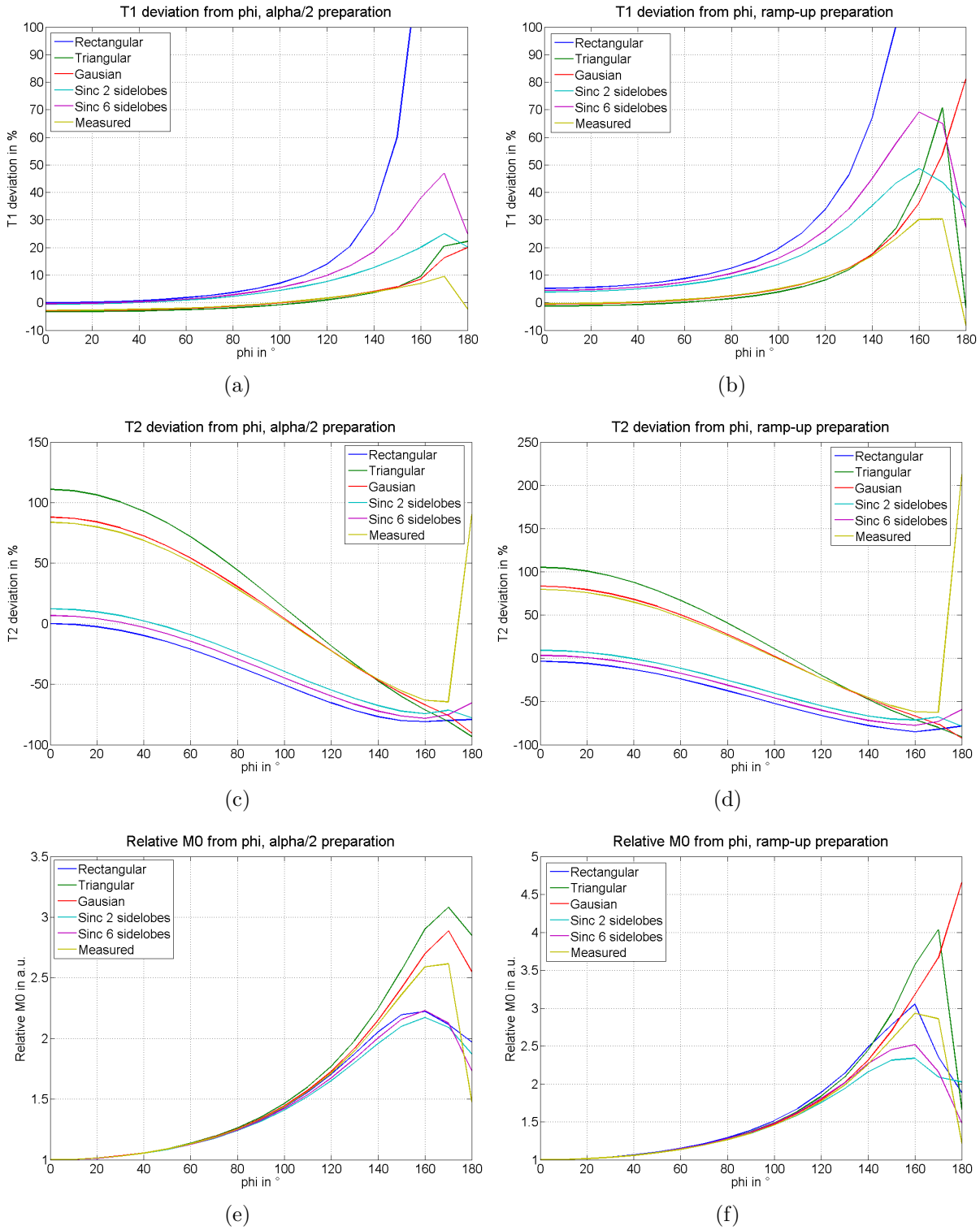

Figure 4.12: The influence on the parameter estimation using the Schmitt-approach for different off-resonance precession angles ϕ acquired during one TR period is illustrated for 6 different flip angle profiles, without noise, based on simulated data. T_1 and T_2 are shown as the deviation of the real value in % and the value of M_0 was normalized to one. (a), (c), (d) data was simulated using $\alpha/2$ preparation, (b), (d), (e) data was simulated using ramp-up preparation.

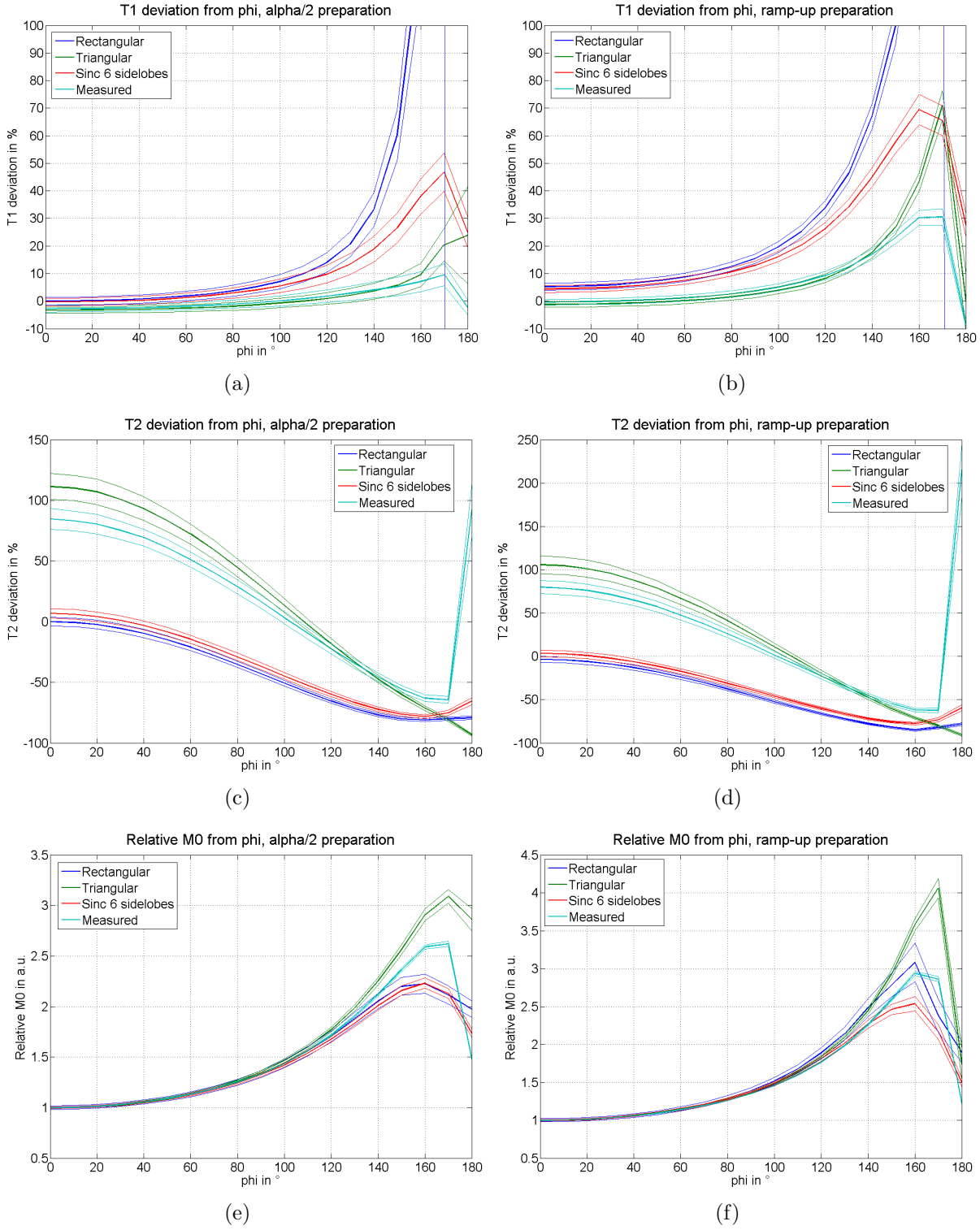

Figure 4.13: The influence on the parameter estimation using the Schmitt-approach for different off-resonance precession angles ϕ acquired during one TR period is illustrated for 4 different flip angle profiles, with a noise level of 10%, based on simulated data. T_1 and T_2 are shown as the deviation of the real value in % and the value of M_0 was normalized to one. The values here are plotted as mean (broad line) and standard deviation (thin line) over 2000 repetitions. (a), (c), (d) data was simulated using $\alpha/2$ preparation, (b), (d), (e) data was simulated using ramp-up preparation.

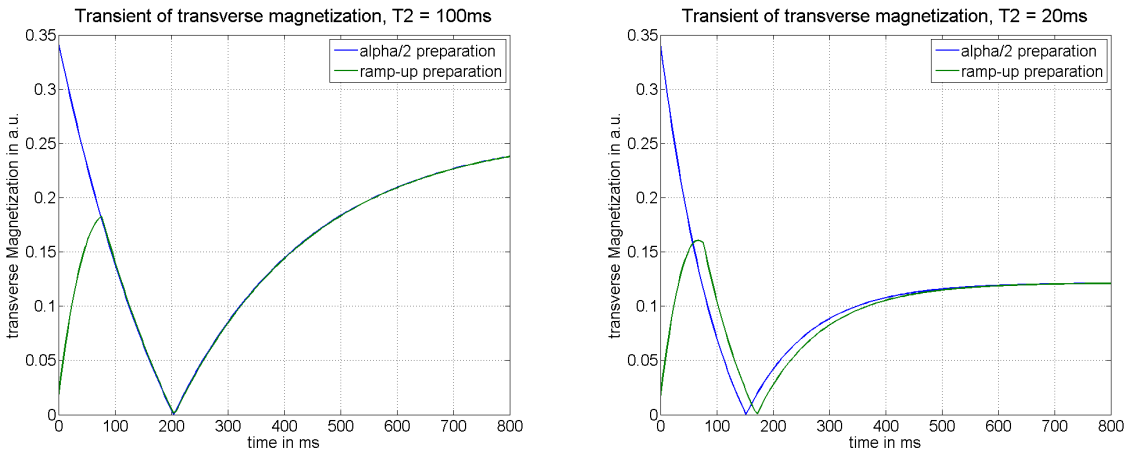

(a) (b)

Figure 4.14: Comparison between the transient responses of the transverse magnetization of a $\alpha/2$ prepared and a ramp-up prepared sequence with different values of T_2. The following parameters were used: $T_1 = 300ms$, $\alpha = 40°$ and $TR = 4ms$ (a) $T_2 = 100ms$, (b) $T_2 = 20ms$.

4.3 Parameter Estimation with Flip Angle Profile Correction on Simulated Data

In this section we present the results for the slice profile corrected parameter estimation algorithm described in Section 3.3.1 with ramp-up and $\alpha/2$ preparation based on simulated measurement data. The influence of the same non-ideal conditions as presented in Section 4.2 are shown here. The results are compared to the parameter estimation results achieved by the Schmitt-approach with an ideal rectangular flip angle profile (ideal conditions). To avoid that the forward simulation and the reconstruction are performed with exactly the same flip angle profile, profiles acquired with different parameters were used. For the forward simulation the flip angle profile acquired with 20mm slice thickness and a resolution of $K = 251$ was used and as flip angle profile in the reconstruction, the one acquired with 5mm slice thickness and a resolution of $K = 18$ was used. The noise evaluation was performed with 5% additive Gaussian noise to the simulated measurement data. The plotted mean and standard deviation were achieved over 1000 repetitions. In the appendix, further simulations with an increased noise level of 10% are presented.

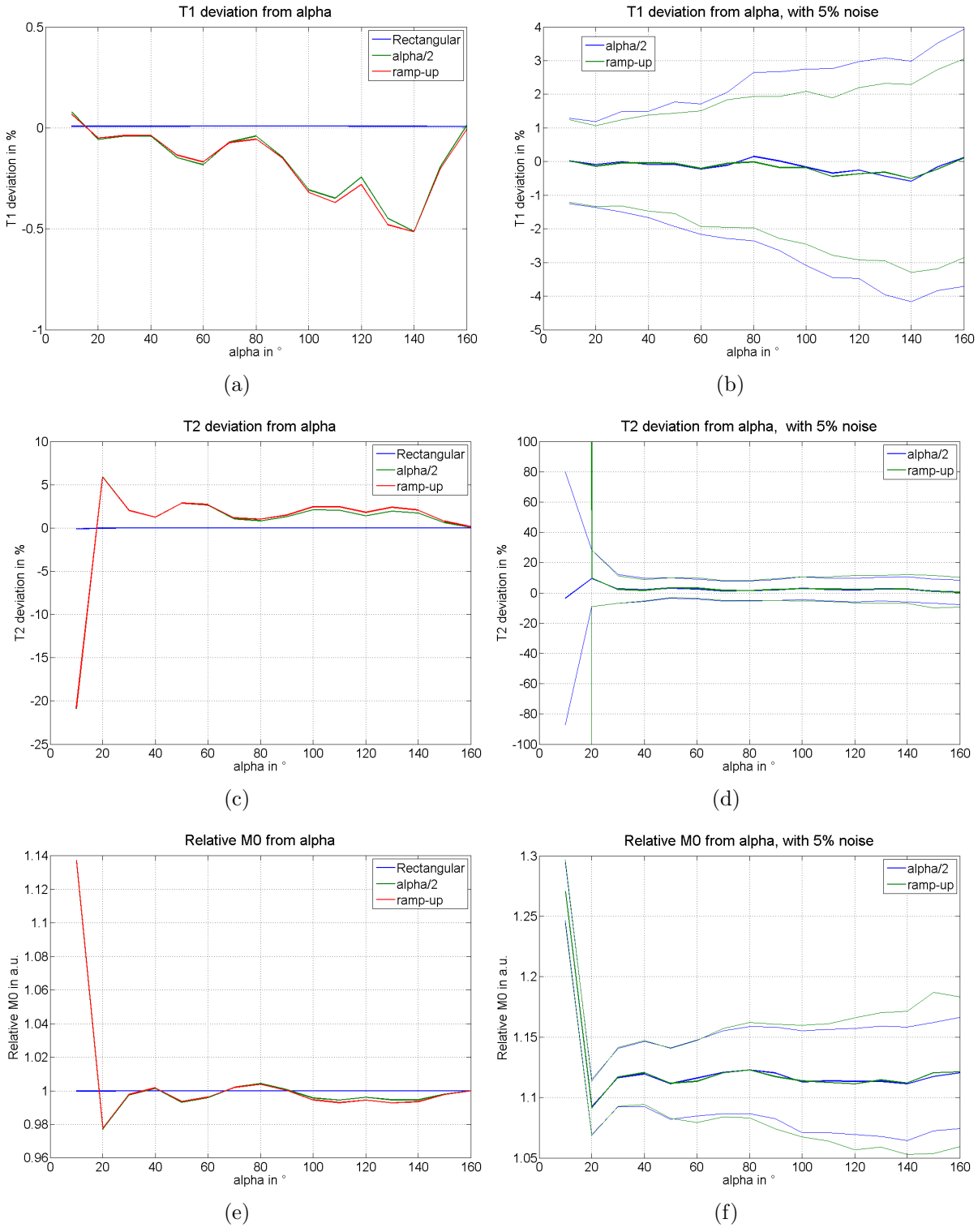

Figure 4.15: The influence on the parameter estimation with flip angle profile correction for different nominal flip angles α_{nom} is illustrated for ramp-up and $\alpha/2$ preparation in comparison to the Schmitt-approach with rectangular flip angle profile based on simulated data. T_1 and T_2 are shown as the deviation of the real value in % and the value of M_0 was normalized to one. (a), (c), (d) without noise (b), (d), (e) simulated data corrupted with 5% Gaussian white noise. The results are plotted as mean (broad line) and standard deviation (thin line) over 1000 repetitions.

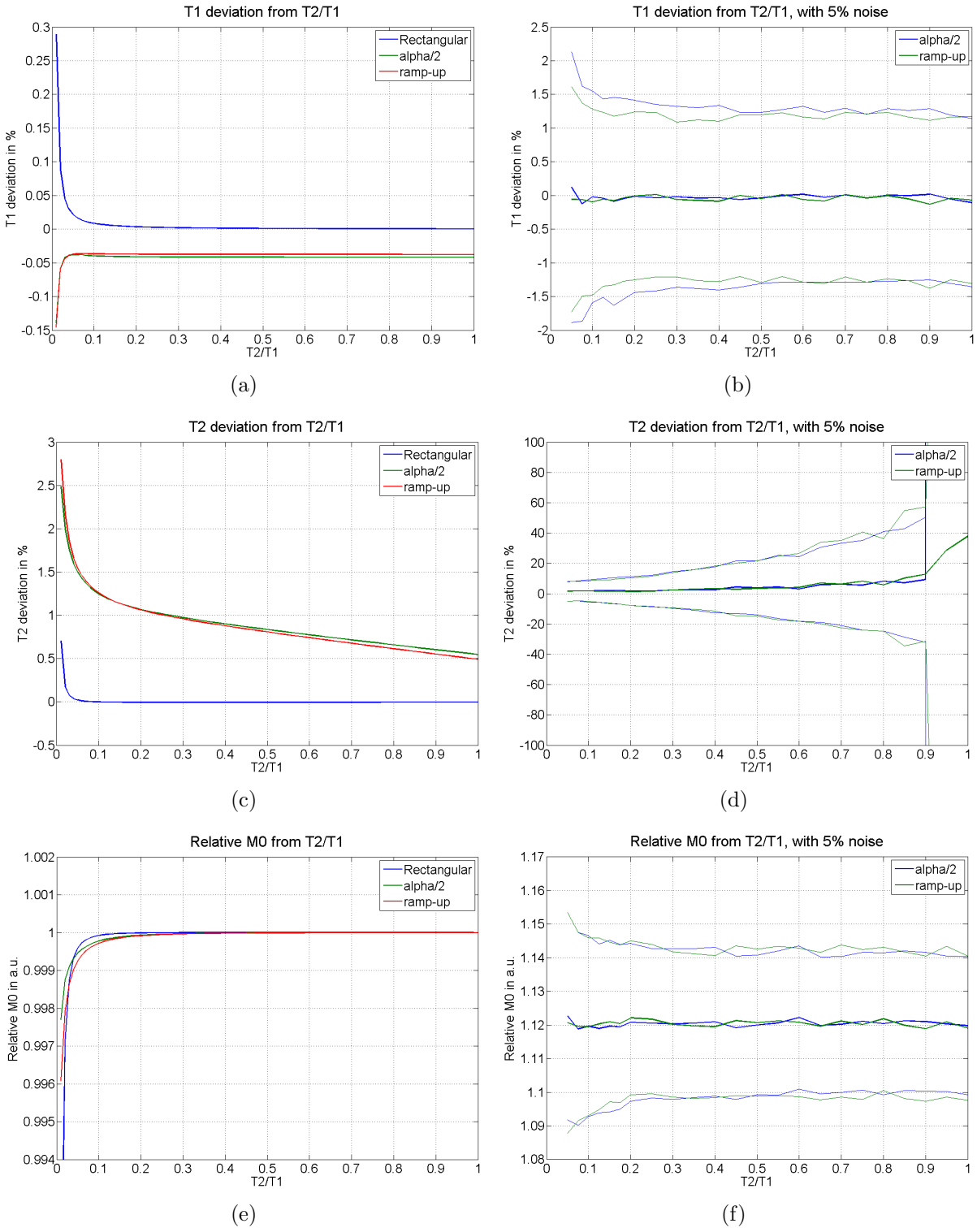

Figure 4.16: The influence on the parameter estimation with flip angle profile correction for different rations of T_2/T_1 is illustrated for ramp-up and $\alpha/2$ preparation in comparison to the Schmitt-approach with rectangular flip angle profile based on simulated data. T_2 is varied from 10ms to 1000ms with a constant value of $T_1 = 1000ms$. T_1 and T_2 are shown as the deviation of the real value in % and the value of M_0 was normalized to one. (a), (c), (d) without noise (b), (d), (e) simulated data corrupted with 5% Gaussian white noise. The results are plotted as mean (broad line) and standard deviation (thin line) over 1000 repetitions.

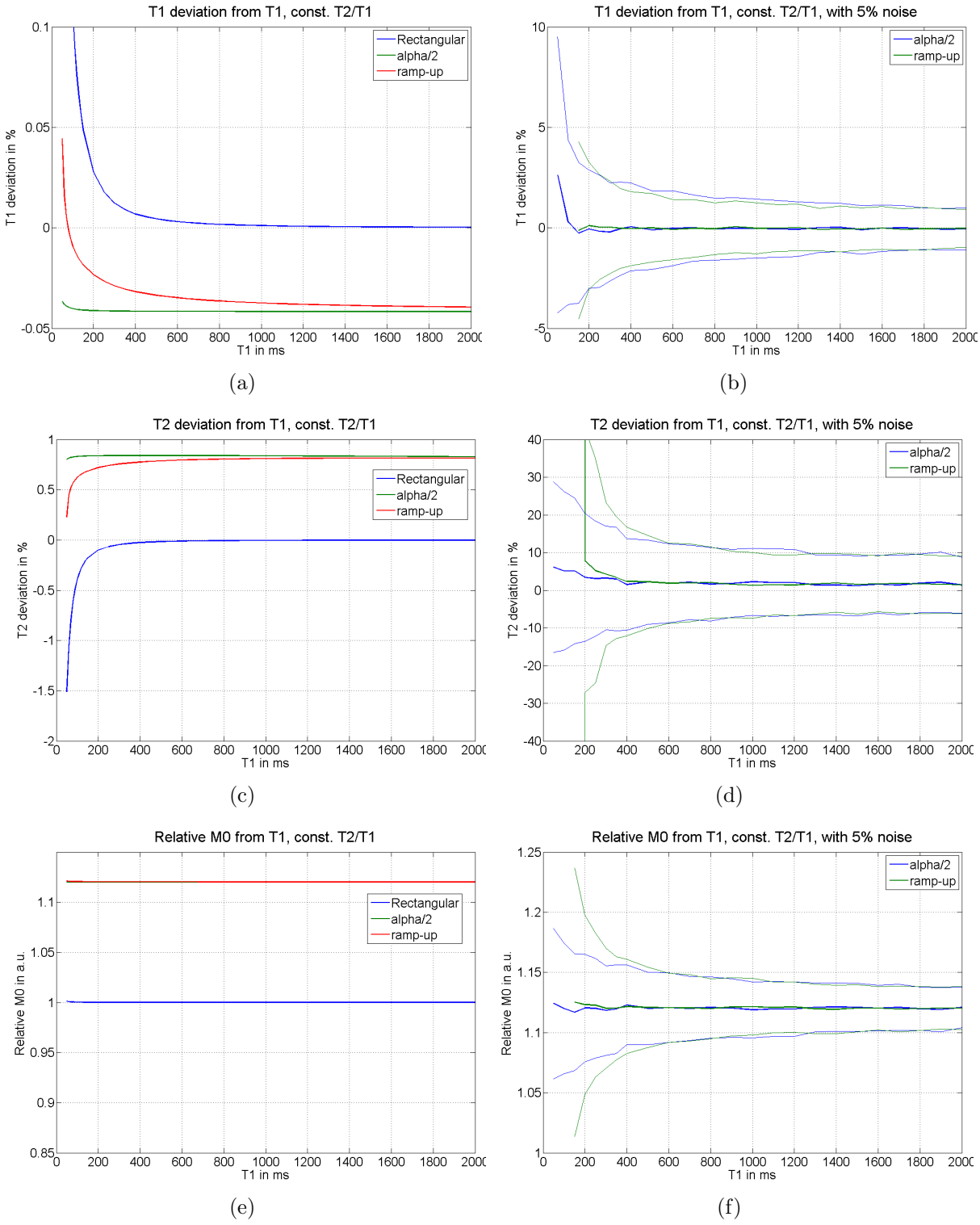

Figure 4.17: The influence on the parameter estimation with flip angle profile correction for different values of T_1 is illustrated for ramp-up and $\alpha/2$ preparation in comparison to the Schmitt-approach with rectangular flip angle profile based on simulated data. The ratio T_2/T_1 is held constant with a value of $T_2 = 0.2T_1$. T_1 and T_2 are shown as the deviation of the real value in % and the value of M_0 was normalized to one. (a), (c), (d) without noise (b), (d), (e) simulated data corrupted with 5% Gaussian white noise. The results are plotted as mean (broad line) and standard deviation (thin line) over 1000 repetitions.

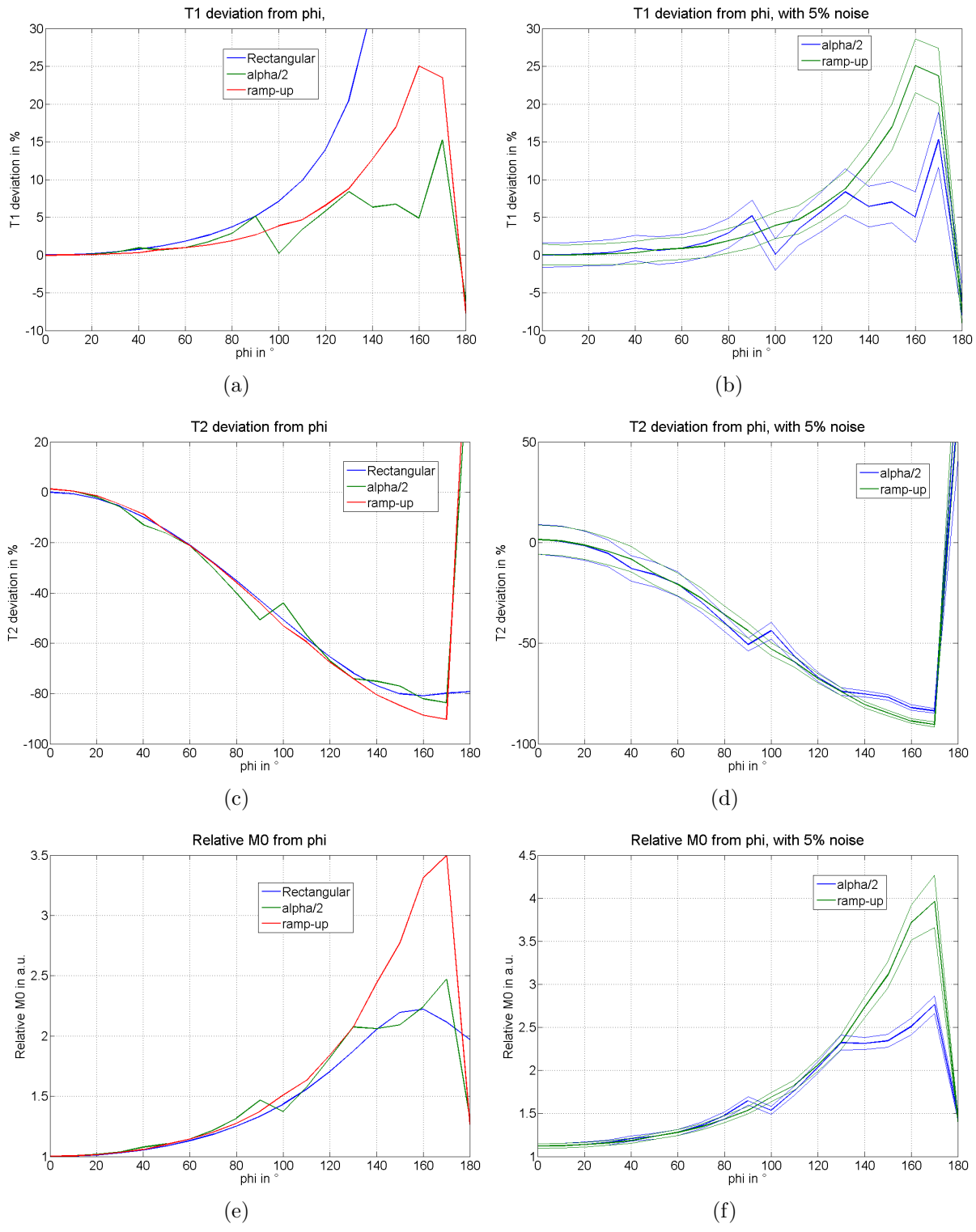

Figure 4.18: The influence on the parameter estimation with flip angle profile correction for different off-resonance precession angles ϕ acquired during on TR period is illustrated for ramp-up and $\alpha/2$ preparation in comparison to the Schmitt-approach with rectangular flip angle profile based on simulated data. T_1 and T_2 are shown as the deviation of the real value in % and the value of M_0 was normalized to one. (a), (c), (d) without noise (b), (d), (e) simulated data corrupted with 5% Gaussian white noise. The results are plotted as mean (broad line) and standard deviation (thin line) over 1000 repetitions.

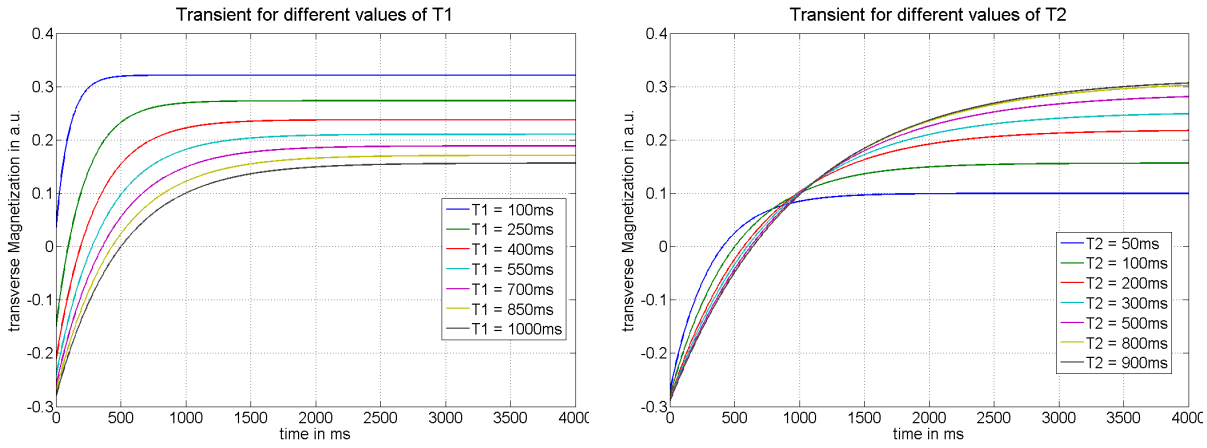

(a) (b)

Figure 4.19: Transient of the bSSFP-sequence after an inversion pulse for different relaxation times simulated for $\alpha = 40°$, $TR = 4ms$ and ramp-up preparation. (a) simulated transient for different values of T_1 with $T_2 = 100ms$ (b) simulated transient for different values of T_2 with $T_1 = 1000ms$.

4.4 Phantom Measurements

In this section we present the results achieved in the agar phantom and the Gd-doped phantoms. The agar phantom consists of the bulk material and two additional inclusions. The quantification performance of the algorithms including flip angle profile correction was evaluated on the basis of the agar phantom. The results for acquired data with different flip angles, different number of phase encoding steps and different factors of under sampling are listed in Table 4.1 and 4.2. The achieved values were compared to those computed by the method of Schmitt and to the reference measurements. The results are denoted as mean and standard deviation inside a ROI. The ROI's were placed in the bulk region, which excludes the two inclusions as it can be seen in Figure 4.21. The deviations of the mean inside this ROI from the mean of the reference measurements inside the same ROI are shown in Table 4.1 and 4.2. The complete parameter maps are illustrated color encoded in Figure 4.20, 4.21 and 4.22. More parameter maps for different flip angles and number of phase encoding steps are depicted in the appendix. Furthermore, the convergence performance of the k-space reconstruction algorithm is shown as the results for a different number of iterations in Table 4.3. As an example of poor quantification accuracy for T_2, the results of the Gd-doped phantoms are illustrated as parameter maps in Figure 4.23, 4.24 and 4.25. The mean and standard deviation inside a ROI in each of the Gd-phantoms and the deviation from the reference measurement is listed in Table 4.4. The last thing which is presented, is the influence of off-resonant excitation on the quantification results in Table 4.5 and the quality of the fitted transient for off-resonant

excitation in Figure 4.26.

		T_1		T_2		M_0	
α	Method	in ms	ϵ in %	in ms	ϵ in %	in a.u.	ϵ in %
	Reference	552 ±2.9	–	62.2 ±1.8	–	0.89 ±0.03	–
40°	Schmitt	514 ±5.2	-6.8%	119.5 ±6.6	92.1%	0.80 ±0.12	-10.4%
	pixel wise	513 ±5.3	-7.1%	71.7 ±17.3	15.2%	0.80 ±0.12	-10.1%
	full	512 ±4.8	-7.2%	67.9 ±2.1	9.12%	0.81 ±0.05	-8.4%
	2 times	514 ±5.0	-6.9%	67.3 ±2.4	8.1%	0.82 ±0.05	-7.6%
	3 times	511 ±5.3	-7.4%	68.7 ±3.4	10.35%	0.80 ±0.05	-10.1%
	4 times	510 ±10.1	-7.5%	70.9 ±10.7	13.9%	0.80 ±0.04	-10.0%
	5 times	513 ±30.1	-7.0%	99.5 ±76.7	60.0%	0.75 ±0.13	-15.7%
50°	Schmitt	511 ±6.2	-7.4%	117.8 ±5.9	89.4%	0.80 ±0.12	-10.4%
	pixel wise	507 ±12.9	-8.2%	69.6 ±81.6	11.9%	0.79 ±0.13	-10.5%
	full	506 ±5.1	-8.2%	62.5 ±1.8	0.5%	0.81 ±0.05	-9.2%
	2 times	506 ±5.1	-8.2%	62.5 ±1.8	0.4%	0.81 ±0.05	-8.9%
	3 times	506 ±5.4	-8.3%	62.9 ±2.4	1.1 %	0.80 ±0.05	-10.0
	4 times	505 ±12.2	-8.4%	64.0 ±9.6	2.8%	0.80 ±0.04	-9.6%
	5 times	517 ±16.4	-6.3%	55.4 ±10.8	-11.0%	0.78 ±0.11	-11.8%
60°	Schmitt	514 ±7.2	-6.9%	118.8 ±5.7	90.9%	0.80 ±0.12	-10.3%
	pixel wise	509 ±11.9	-7.8%	61.6 ±7.2	-1.1%	0.80 ±0.13	-9.9%
	full	509 ±5.4	-7.8%	59.3 ±1.7	-4.7%	0.81 ±0.05	-9.1%
	2 times	509 ±5.4	-7.9%	59.3 ±1.7	-4.6%	0.81 ±0.05	-9.1%
	3 times	509 ±5.8	-7.9%	59.1 ±2.3	-4.9%	0.80 ±0.05	-9.6%
	4 times	506 ±14.3	-8.3%	61.4 ±9.8	-1.4%	0.80 ±0.05	-9.9%
	5 times	523 ±19.3	-5.2%	50.9 ±10.6	-18.2%	0.75 ±0.12	-15.1%

Table 4.1: Quantification results for the agar phantom in a ROI which excludes the two embeddings and outliers. The mean and standard deviation of all three parameters in the ROI are listed for both reconstruction algorithms and for comparison the results achieved by the Schmitt-approach and the reference measure are listed as well. The reconstruction algorithm based on k-space data was performed with a *full*-sampled and a *2* to *5 times* under-sampled k-space. The error ϵ is the deviation of the mean value inside the ROI to the mean value of the reference measure inside the same ROI. The results are shown for flip angles $\alpha = 40°; 50°; 60°$ and a number of phase encoding steps of $N_{seg} = 8$.

		T_1		T_2		M_0	
α	Method	in ms	ϵ in %	in ms	ϵ in %	in a.u.	ϵ in %
	Reference	552 ±2.9	–	62.2 ±1.8	–	0.89 ±0.03	–
40°	Schmitt	490 ±13.0	-11.2%	136.3 ±9.3	119%	0.80 ±0.12	-10.0%
	pixel wise	492 ±11.2	-10.8%	87.2 ±21.7	40.1%	0.80 ±0.12	-10.3%
	full	489 ±9.5	-11.4%	81.8±4.7	31.4%	0.80 ±0.05	-9.8%
	2 times	488 ±9.6	-11.5%	82.0 ±4.9	31.8%	0.81 ±0.05	-9.4%
	3 times	460 ±24.3	-16.7%	599.5 ±693	863%	0.68 ±0.11	-23.7%
	4 times	474 ±27.3	-14.1%	441.8 ±920	610%	0.73 ±0.11	-18.2%
	5 times	505 ±24.6	-8.4%	66.5 ±21.6	6.8%	0.78 ±0.11	-12.1%
50°	Schmitt	488 ±13.9	-11.5%	128.6 ±7.2	106.8%	0.80 ±0.11	-10.0%
	pixel wise	488 ±15.6	-11.6%	73.5 ±5.1	18.1%	0.80 ±0.13	-9.6%
	full	485 ±9.9	-12.0%	73.0 ±2.9	17.3%	0.80 ±0.05	-9.6%
	2 times	486 ±9.7	-12.0%	73.0 ±2.8	17.3%	0.80 ±0.05	-10.2%
	3 times	486 ±11.4	-12.0%	75.4 ±10.4	21.2 %	0.79 ±0.05	-10.8%
	4 times	442 ±34.2	-20.0%	487 ±369	682%	0.64 ±0.14	-28.0%
	5 times	507 ±27.0	-8.2%	57.2 ±16.4	-8.0%	0.76 ±0.12	-14.6%
60°	Schmitt	488 ±25.6	-12.0%	130.7 ±7.6	110.1%	0.80 ±0.12	-10.4%
	pixel wise	485 ±25.4	-12.2%	70.8 ±8.1	13.8%	0.80 ±0.15	-10.5%
	full	481 ±10.5	-12.8%	70.1 ±2.4	12.7%	0.80 ±0.05	-9.6%
	2 times	481 ±10.5	-12.8%	70.1 ±2.5	12.7%	0.80 ±0.05	-9.5%
	3 times	481 ±10.9	-12.8%	70.4 ±4.2	13.1%	0.74 ±0.04	-16.4%
	4 times	475 ±28.2	-13.8%	79.5 ±32.0	27.7%	0.77 ±0.10	-12.8%
	5 times	508 ±30.4	-7.9%	52.7 ±15.4	-15.3%	0.75 ±0.13	-15.6%

Table 4.2: Quantification results for the agar phantom in a ROI which excludes the two embeddings and outliers. The mean and standard deviation of all three parameters in the ROI are listed for both reconstruction algorithms and for comparison the results achieved by the Schmitt-approach and the reference measure are listed as well. The reconstruction algorithm based on k-space data was performed with a *full*-sampled and a *2* to *5 times* under-sampled k-space. The error ϵ is the deviation of the mean value inside the ROI to the mean value of the reference measure inside the same ROI. The results are shown for flip angles $\alpha = 40°; 50°; 60°$ and a number of phase encoding steps of $N_{seg} = 16$.

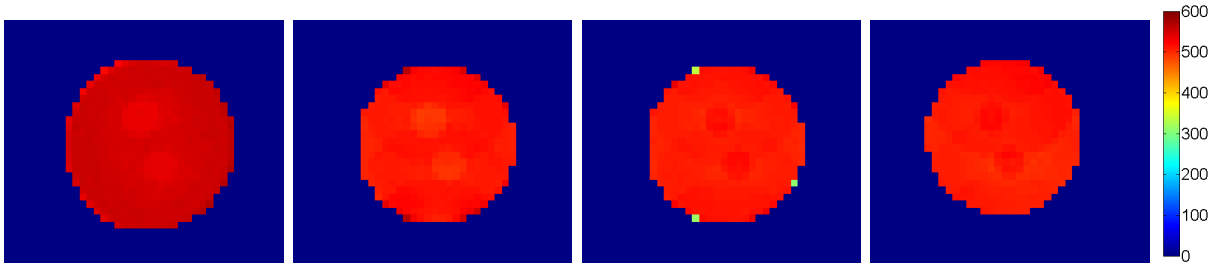

(a) (b) (c) (d)

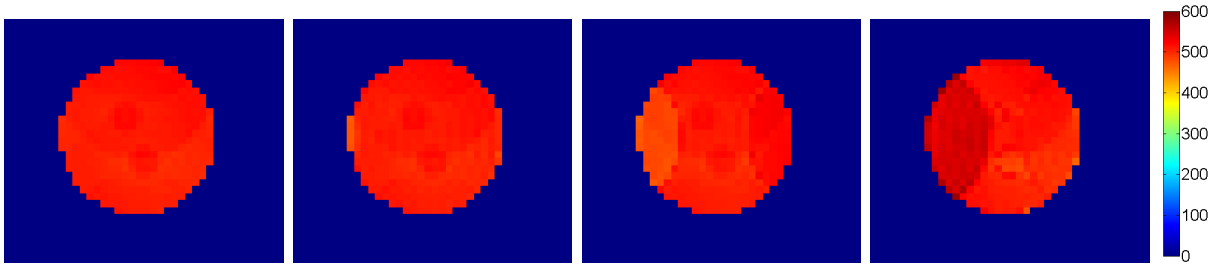

(f) (g) (h) (i)

Figure 4.20: T_1 maps in the Agar phantom generated with different methods for an acquisition with $N_{seg} = 8$ and $\alpha = 60°$. The values are displayed in ms. (a) Reference measurement, (b) Schmitt-approach, (c) pixel wise reconstruction, (d) reconstruction in k-space with full-sampled data, (f) 2-times under-sampled data, (g) 3-times under-sampled data, (h) 4-times under-sampled data, (i) 5-times under-sampled data.

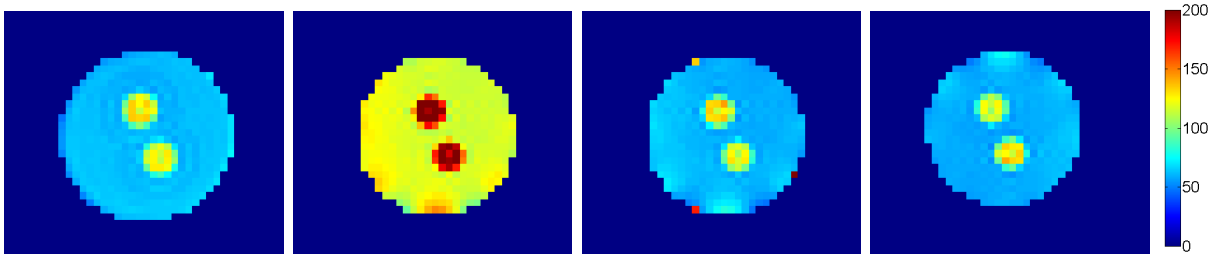

(a) (b) (c) (d)

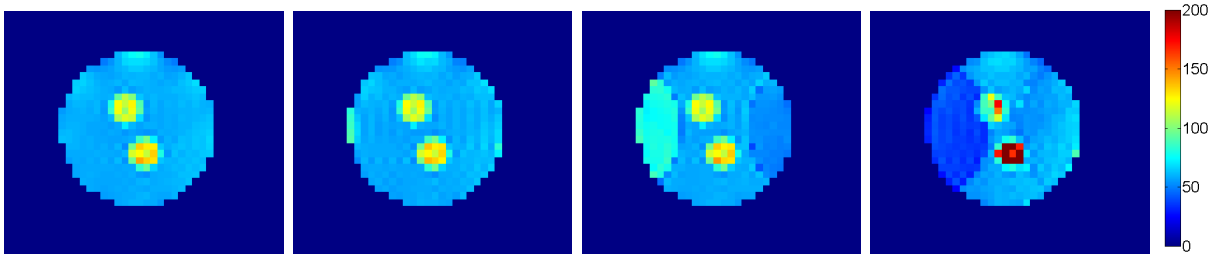

(f) (g) (h) (i)

Figure 4.21: T_2 maps in the Agar phantom generated with different methods for an acquisition with $N_{seg} = 8$ and $\alpha = 60°$. The values are displayed in ms. (a) Reference measurement, (b) Schmitt-approach, (c) pixel wise reconstruction, (d) reconstruction in k-space with full-sampled data, (f) 2-times under-sampled data, (g) 3-times under-sampled data, (h) 4-times under-sampled data, (i) 5-times under-sampled data.

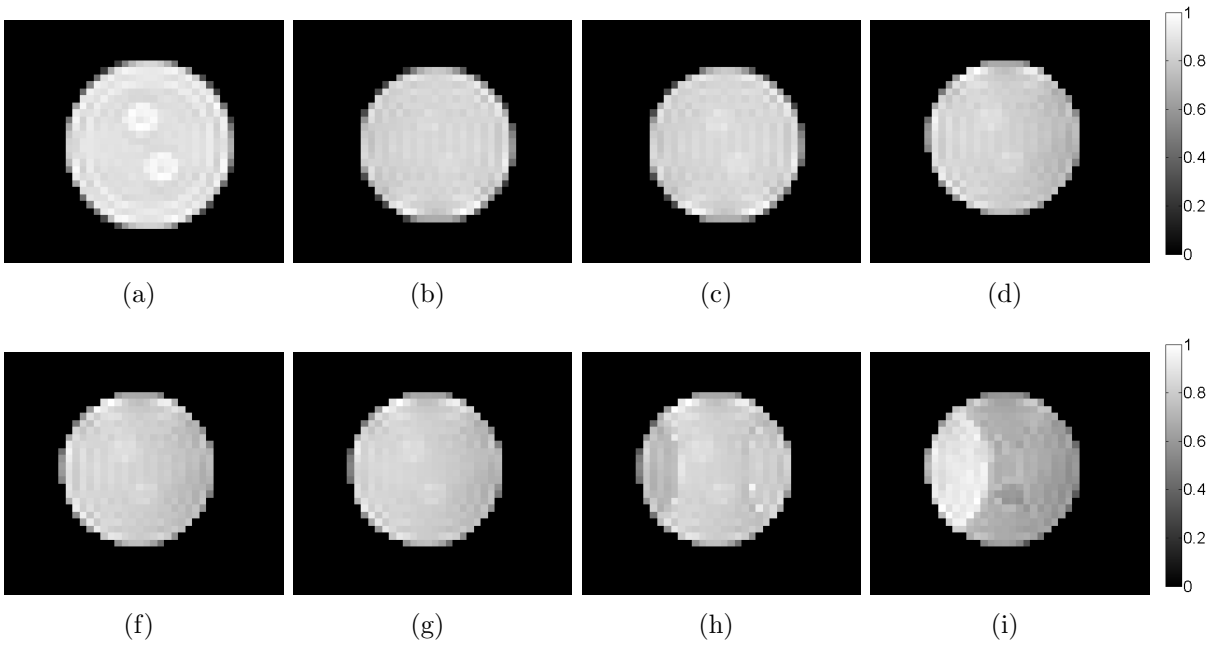

Figure 4.22: M_0 maps in the Agar phantom generated with different methods for an acquisition with $N_{seg} = 8$ and $\alpha = 60°$. The values are displayed in ms. (a) Reference measurement, (b) Schmitt-approach, (c) pixel wise reconstruction, (d) reconstruction in k-space with full-sampled data, (f) 2-times under-sampled data, (g) 3-times under-sampled data, (h) 4-times under-sampled data, (i) 5-times under-sampled data.

		T_1		T_2		M_0	
δ	iterations	in ms	ϵ in %	in ms	ϵ in %	in a.u.	ϵ in %
full	20	493.6 ±6.61	-10.6%	100.5 ±5.41	61.5%	0.80 ±0.05	-9.7%
	50	508.3 ±5.09	-7.9%	70.3 ±5.11	13.0%	0.79 ±0.06	-10.7%
	70	511.2 ±5.01	-7.4%	68.0 ±2.37	9.30%	0.79 ±0.05	-10.8%
	100	511.4 ±5.06	-7.3%	66.3 ±2.16	6.53%	0.83 ±0.05	-6.9%
	150	512.1 ±4.65	-7.2%	68.8 ±2.07	10.56%	0.81 ±0.05	-8.4%
	200	512.6 ±4.78	-7.1%	67.9 ±2.19	9.11%	0.82 ±0.05	-8.1%
	500	512.1 ±4.81	-7.2%	67.9 ±1.99	9.14%	0.82 ±0.05	-8.0%
	1000	512.1 ±4.81	-7.2%	67.9 ±1.99	9.15%	0.82 ±0.05	-8.0%
3	20	481.9 ±5.52	-12.7%	174.2 ±7.37	180%	0.82 ±0.05	-7.8%
	50	491.1 ±5.64	-11.0%	109.7 ±16.2	76.2%	0.74 ±0.06	-17.2%
	70	506.5 ±8.40	-8.2%	81.2 ±13.6	30.5%	0.77 ±0.07	-13.7%
	100	514.7 ±6.23	-6.7%	64.5 ±4.06	3.59%	0.84 ±0.05	-5.3%
	150	512.1 ±5.07	-7.2%	67.5 ±2.45	8.41%	0.83 ±0.04	-6.8%
	200	511.9 ±5.26	-7.2%	68.1 ±3.09	9.48%	0.82 ±0.05	-7.6%
	500	512.0 ±5.06	-7.2%	68.0 ±2.66	9.34%	0.81 ±0.05	-8.4%
	1000	512.0 ±5.04	-7.2%	68.0 ±2.63	9.26%	0.81 ±0.05	-8.3%

Table 4.3: Results for the k-space based reconstruction algorithm with different numbers of iteration for full-sampled and 3-times under-sampled k-space data. The parameters are listed as mean and standard deviation inside the ROI. The error ϵ is the deviation of the mean value to the reference value. The results are listed for $\alpha = 40°$ and $N_{seg} = 8$.

		T_1		T_2	
Gd-conc.	Method	in ms	ϵ in %	in ms	ϵ in %
2mM	Reference	87.2 ±2.21	–	73.9 ±1.66	–
	Schmitt	80.1 ±0.86	-8.1%	165.3 ±1.83	123%
	PW recon.	85.5 ±1.52	-2.0%	–*	–*
	k-space	85.4 ±0.95	-2.1%	405.5 ±1.25	448%
1mM	Reference	172.0 ±2.25	–	144.8 ±2.8	–
	Schmitt	164.3 ±3.23	-4.5%	195.1 ±51.1	34.8%
	PW recon.	176.7 ±2.91	2.8%	95.9 ±17.0	-33.8%
	k-space	175.4 ±3.59	2.0%	100.6 ±14.9	-30.5%
0.5mM	Reference	323.4 ±4.83	–	256.5 ±5.4	–
	Schmitt	306.6 ±3.09	-5.2%	518.3 ±65.0	102%
	PW recon.	325.9 ±2.82	0.8%	288.8 ±31.9	12.6%
	k-space	323.2 ±3.84	-0.1%	433.1 ±110.4	68.9%
0.25mM	Reference	481.8 ±6.03	–	376.4 ±42.8	–
	Schmitt	468.7 ±6.33	-2.7%	578.6 ±79.9	53.7%
	PW recon.	491.4 ±5.92	2.0%	370.4 ±49.2	-1.6%
	k-space	488.2 ±7.40	1.3%	452.7 ±112.1	20.3%
0.125mM	Reference	947.9 ±12.8	–	697.8 ±89.1	–
	Schmitt	920.6 ±10.3	-2.9%	1026.7 ±109.9	47.2%
	PW recon.	955.6 ±9.99	0.8%	719.5 ±84.0	3.12%
	k-space	955.7 ±10.3	0.8%	687.5 ±70.1	-1.47%

Table 4.4: Quantification results for the Gd-doped phantoms with different concentrations inside a ROI. The mean and standard deviation of T_1 and T_2 are listed for both reconstruction algorithms, the Schmitt-approach and the reference value. The reconstruction algorithm based on k-space data was performed with a *full*-sampled k-space. The error ϵ is the deviation of the mean value inside the ROI to the mean value of the reference measure inside the same ROI. The results are listed for flip angles $\alpha = 40°$ and a number of segments $N_{seg} = 8$. (* Algorithm has not converged.)

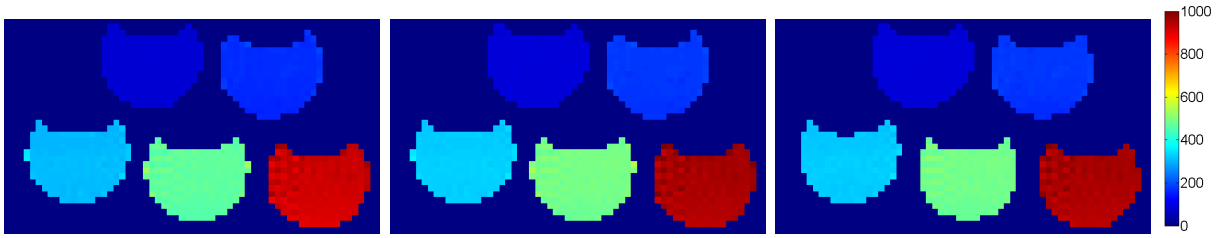

(a) (b) (c)

Figure 4.23: T_1 maps of the Gd-doped phantoms generated with different methods for an acquisition with $N_{seg} = 8$ and $\alpha = 40°$. The scale is displayed in ms. The Gd-concentration of the phantoms is from left to right and from top to bottom 2mM, 1mM, 0.5mM, 0.25mM and 0.125mM. (a) Schmitt-approach, (b) pixel wise reconstruction, (c) reconstruction in k-space with full-sampled data.

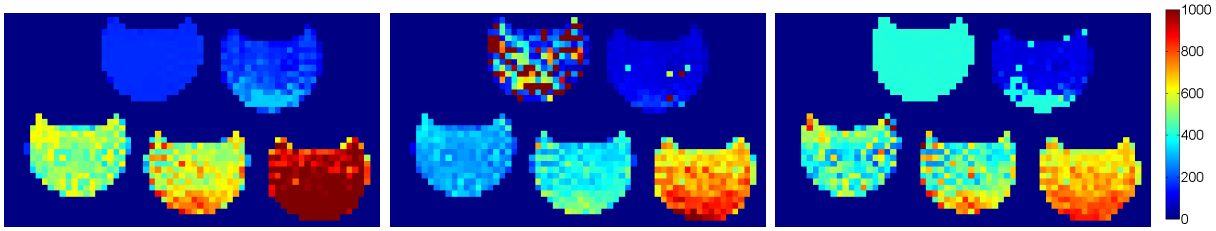

(a) (b) (c)

Figure 4.24: T_2 maps of the Gd-doped phantoms generated with different methods for an acquisition with $N_{seg} = 8$ and $\alpha = 40°$. The scale is displayed in ms. The Gd-concentration of the phantoms is from left to right and from top to bottom 2mM, 1mM, 0.5mM, 0.25mM and 0.125mM. (a) Schmitt-approach, (b) pixel wise reconstruction, (c) reconstruction in k-space with full-sampled data.

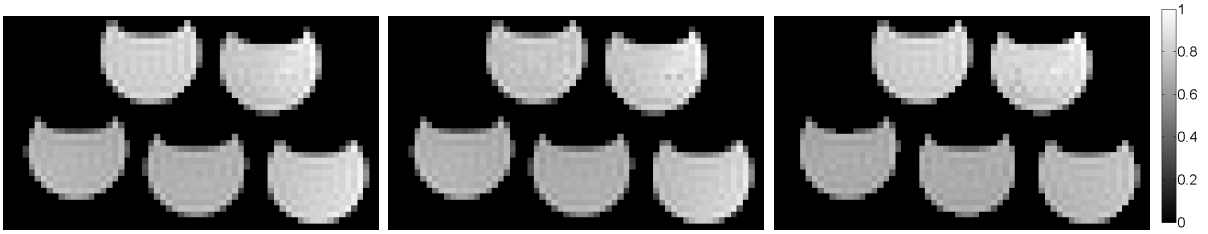

(a) (b) (c)

Figure 4.25: M_0 maps of the Gd-doped phantoms generated with different methods for an acquisition with $N_{seg} = 8$ and $\alpha = 40°$. The scale is displayed in arbitrary units, the maximum value is normalized to one. The Gd-concentration of the phantoms is from left to right and from top to bottom 2mM, 1mM, 0.5mM, 0.25mM and 0.125mM. (a) Schmitt-approach, (b) pixel wise reconstruction, (c) reconstruction in k-space with full-sampled data.

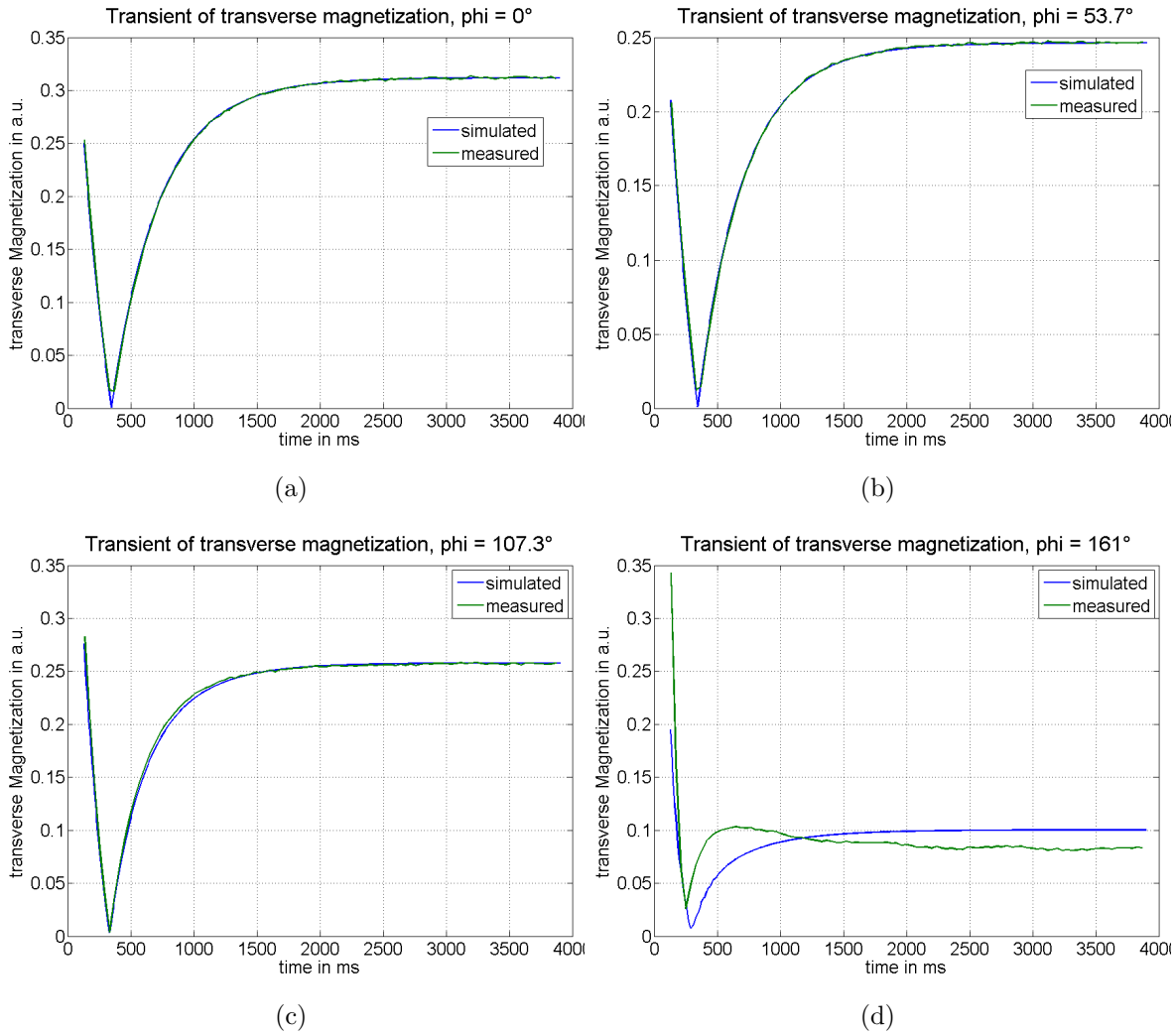

Figure 4.26: Comparison between the simulated and measured transient in the agar phantom for different off-resonance precession angles ϕ. The acquisition was performed with $\alpha = 40°$, $N_{seg} = 8$ and different off-resonance frequencies. The simulation was performed using the T_1 and T_2 values achieved at zero off-resonance. (a) $\Delta f = 0Hz$, $\phi = 0°$; (b) $\Delta f = 30Hz$, $\phi \approx 53.7°$; (c) $\Delta f = 60Hz$, $\phi \approx 107°$; (d) $\Delta f = 90Hz$, $\phi \approx 161°$.

		pixel wise reconstruction		Schmitt approach	
Δf in Hz	ϕ in °	T_1 in ms	T_2 in ms	T_1 in ms	T_2 in ms
0	0	524.7 ±3.27	73.3 ±4.14	527.4 ±2.86	122.7 ±1.93
15	26.8	525.2 ±1.62	73.5 ±1.98	526.2 ±1.99	123.4 ±2.66
30	53.7	529.6 ±2.69	59.7 ±2.18	537.5 ±3.75	103.6 ±2.88
45	80.5	534.9 ±2.81	43.2 ±2.31	555.6 ±3.69	79.6 ±2.95
60	107.3	541.8 ±3.08	27.8 ±1.72	589.5 ±6.12	55.4 ±2.82
90	161.0	646.0 ±36.9	3.8 ±0.21	1137 ±284	13.14 ±3.29

Table 4.5: Quantification results for different off-resonance precession angles ϕ performed with pixel wise reconstruction and the Schmitt approach. The off-resonance frequency Δf was adjusted on the scanner and the off-resonance precession angle follows from TR.

4.5 In Vivo Measurements

In this section we present the quantification results achieved inside the human brain for the different reconstruction algorithms and different factors of under-sampling. The results are illustrated as color encoded parameter maps in Figures 4.27, 4.28 and 4.29 and are listed as mean and standard deviation inside a ROI in the three main types of tissue in the brain (GM, WM and CSF). The results are compared to those achieved by the Schmitt approach and the reference measurements. To show the inter subject variability the results of three different volunteers are listed in Table 4.7.

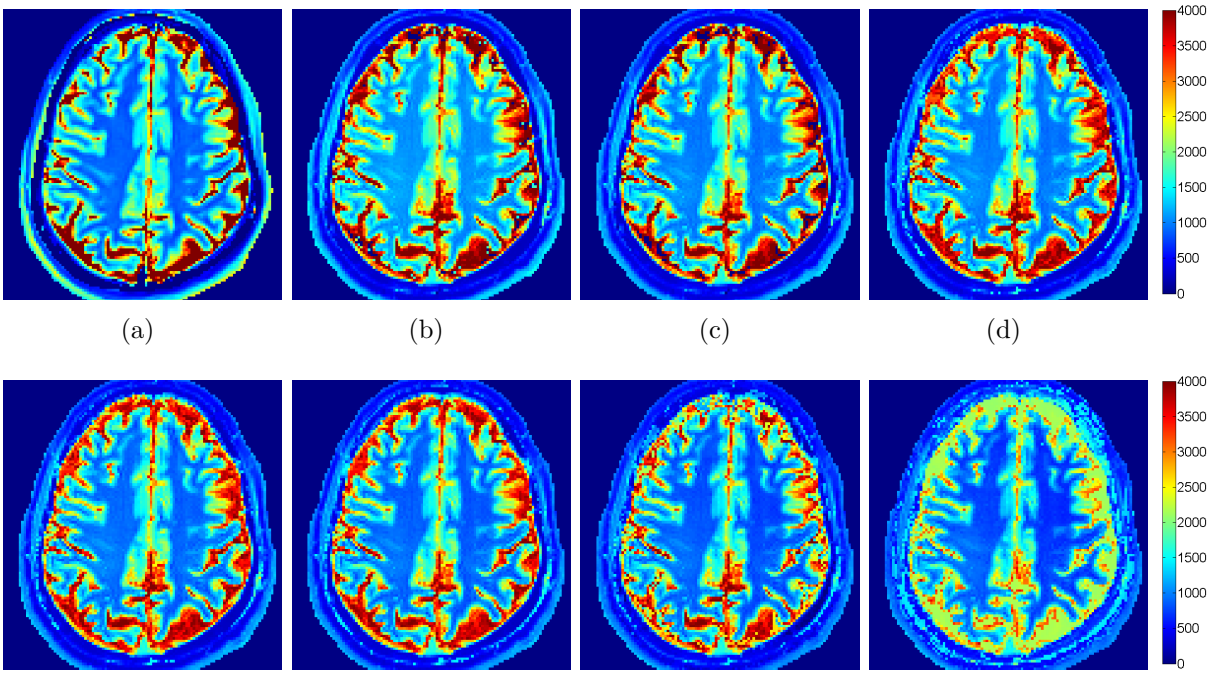

Figure 4.27: T_1 maps in vivo generated with different methods for an acquisition with $N_{seg} = 8$ and $\alpha = 40°$. The values are displayed in ms. (a) Reference measurement, (b) Schmitt-approach, (c) pixel wise reconstruction, (d) reconstruction in k-space with full-sampled data, (f) 2-times under-sampled data, (g) 3-times under-sampled data, (h) 4-times under-sampled data, (i) 5-times under-sampled data.

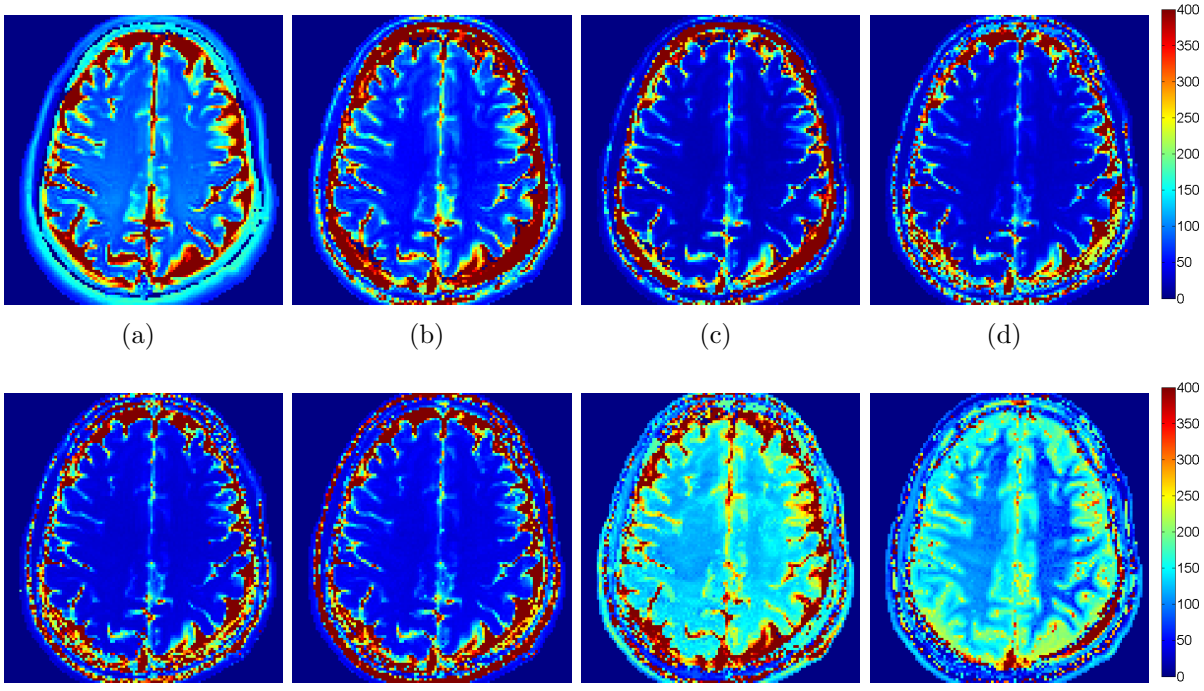

Figure 4.28: T_2 maps in vivo generated with different methods for an acquisition with $N_{seg} = 8$ and $\alpha = 40°$. The values are displayed in ms. (a) Reference measurement, (b) Schmitt-approach, (c) pixel wise reconstruction, (d) reconstruction in k-space with full-sampled data, (f) 2-times under-sampled data, (g) 3-times under-sampled data, (h) 4-times under-sampled data, (i) 5-times under-sampled data.

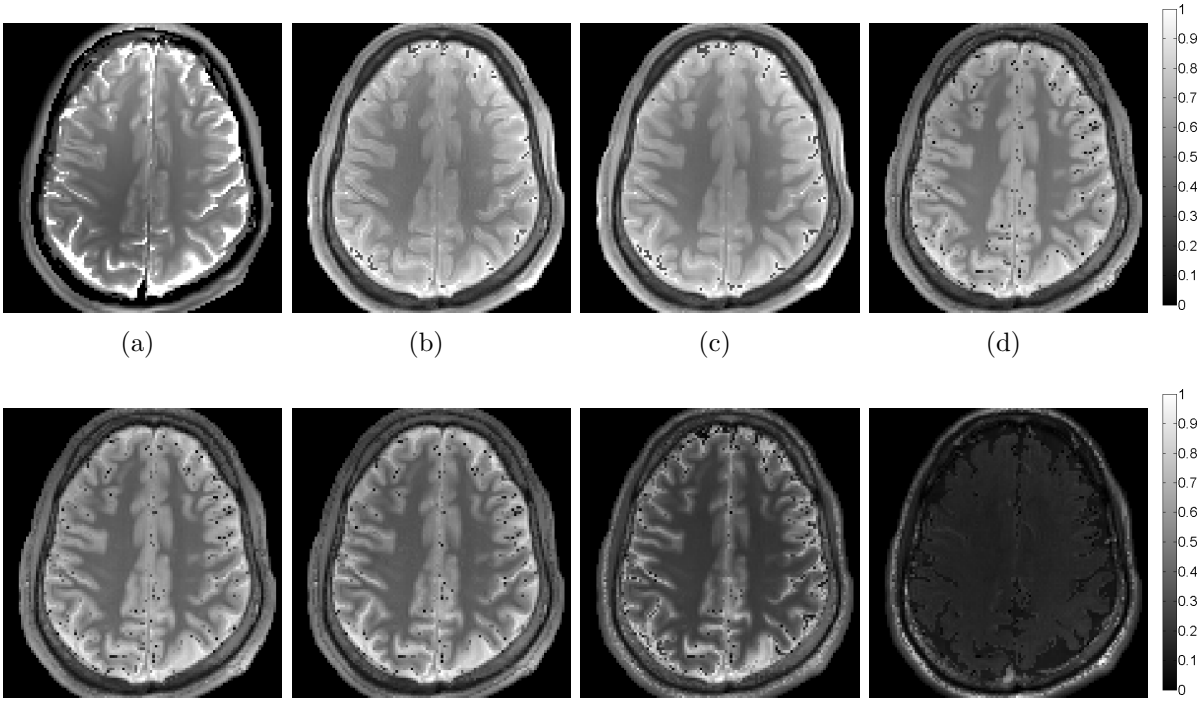

Figure 4.29: M_0 maps in vivo generated with different methods for an acquisition with $N_{seg} = 8$ and $\alpha = 40°$. The values are displayed in ms. (a) Reference measurement, (b) Schmitt-approach, (c) pixel wise reconstruction, (d) reconstruction in k-space with full-sampled data, (f) 2-times under-sampled data, (g) 3-times under-sampled data, (h) 4-times under-sampled data, (i) 5-times under-sampled data.

		T_1		T_2		M_0
	Method	in ms	ϵ in %	in ms	ϵ in %	in a.u.
GM	Reference	1628 ±207	–	125.4 ±52.5	–	0.48 ±0.06
	Schmitt	1970 ±350	21.0%	83.9 ±25.1	-33%	0.54 ±0.04
	pixel wise	1841 ±337	13.1%	39.1 ±15.5	-69%	0.53 ±0.04
	full	1869 ±354	14.8%	39.8 ±13.7	-68%	0.60 ±0.13
	2 times	1781 ±346	9.4%	44.7 ±14.6	-64%	0.55 ±0.12
	3 times	1720 ±335	5.6%	53.2 ±14.6	-58%	0.49 ±0.12
	4 times	1629 ±340	0.1%	165.7 ±37.7	32%	0.35 ±0.10
	5 times	1561 ±333	-4.1%	151.2 ±23.3	21%	0.14 ±0.03
WM	Reference	872 ±36.4	–	87.3 ±5.8	–	0.39 ±0.04
	Schmitt	1071 ±43.2	22.9%	49.7 ±3.3	-43%	0.44 ±0.02
	pixel wise	969 ±45.8	11.2%	20.7 ±1.5	-76%	0.41 ±0.02
	full	974 ±48.4	11.7%	25.7 ±1.3	-71%	0.43 ±0.02
	2 times	906 ±48.4	3.9%	31.7 ±1.9	-64%	0.37 ±0.01
	3 times	867 ±53.3	-0.6%	37.2 ±2.2	-57%	0.34 ±0.02
	4 times	810 ±62.2	-7.1%	124.0 ±9.8	42%	0.22 ±0.01
	5 times	745 ±75.4	-14.6%	90.4 ±12.7	3.6%	0.13 ±0.01
CSF	Reference	35707 ±55772	–	874 ±382	–	5.32 ±7.10
	Schmitt	3040 ±1682	–	379 ±354	-57%	2.64 ±9.30
	pixel wise	–*	–	–*	–*	2.11 ±5.80
	full	3705 ±271	–	578 ±324	-34%	0.80 ±0.08
	2 times	3704 ±214	–	683 ±347	-22%	0.79 ±0.08
	3 times	3713 ±202	–	656 ±350	-25%	0.79 ±0.08
	4 times	2742 ±940	–	433 ±199	-50%	0.50 ±0.25
	5 times	2179 ±205	–	194 ±24.5	-78%	0.09 ±0.02

Table 4.6: Quantification results for an in-vivo measurement in a healthy volunteer for three different ROIs. Each ROI covers one of the three main tissue types in brain, GM, WM and CSF. The mean and standard deviation of all three parameters inside the three ROIs are listed for both reconstruction algorithms, the Schmitt-approach and the reference measurement. The reconstruction algorithm based on k-space data was performed with a *full*-sampled and a *2* to *5 times* under-sampled k-space. The error ϵ is the deviation of the mean value inside the ROI to the mean value of the reference measure inside the same ROI. Because the reference measurement for T_1 in CSF fails, no error was calculated. The measurement was performed with $\alpha = 40°$ and $N_{seg} = 8$. (* Algorithm has not converged.)

Region	Method	VNr.	T_1 in ms	T_2 in ms	M_0 in a.u.
GM	Schmitt	1	1603 ±233	89.5 ±22.2	0.58 ±0.13
		2	1612 ±195	98.4 ±16.9	0.77 ±0.06
		3	1615 ±154	88.5 ±11.1	0.71 ±0.08
	pixel wise	1	1537 ±236	38.2 ±11.6	0.67 ±0.15
		2	1551 ±195	44.5 ±9.2	0.76 ±0.06
		3	1532 ±147	41.8 ±6.7	0.71 ±0.08
WM	Schmitt	1	1021 ±52.5	49.7 ±4.3	0.48 ±0.05
		2	977 ±44.7	56.9 ±4.4	0.59 ±0.03
		3	1084 ±46.1	60.1 ±4.3	0.56 ±0.05
	pixel wise	1	924 ±47.1	20.0 ±2.1	0.53 ±0.05
		2	897 ±42.4	24.1 ±2.2	0.56 ±0.03
		3	1002 ±45.0	26.4 ±2.2	0.55 ±0.05
CSF	Schmitt	1	3550 ±290	2419 ±2636	0.49 ±0.07
		2	4100 ±379	807 ±586	0.72 ±0.17
		3	4220 ±414	465 ±277	0.63 ±0.09
	pixel wise	1	3616 ±317	–*	0.57 ±0.08
		2	4162 ±371	534 ±457	0.70 ±0.10
		3	4145 ±456	292 ±186	0.64 ±0.09

Table 4.7: Quantification results in GM, WM and CSF in three different volunteers. The results are listed for the quantification according to Schmitt and the pixel wise reconstruction inside the same ROI. The data acquisition was performed with $\alpha = 40°$ and $N_{seg} = 8$. (* Algorithm has not converged.)

4.6 Influence of Magnetization Transfer

In this section we present the simulated results including MT-effects. In Figure 4.30 the fitted transients with the quantified parameters are depicted in WM. Even though the calculated parameters deviated substantially from the reference measure, but the cure fit the measured data quite well. In contrast to that, Figures 4.31 and 4.32 illustrate the simulated transient including the influence of on-resonant magnetization transfer effects in GM and WM for different nominal flip angles. The relaxation parameters were taken from the reference measures. This simulation is compared to the measured transient and the transient simulated with the true relaxation parameters without magnetization transfer. The parameters to simulate the magnetization transfer in both tissues were taken from [29]. Table 4.8 lists the quantified relaxation parameters corrected for flip angle profiles and the ratio between the simulated steady state signal with true relaxation parameters without MT effect and the measured steady state signal ΔS_{MT} for different nominal flip angles in GM and WM.

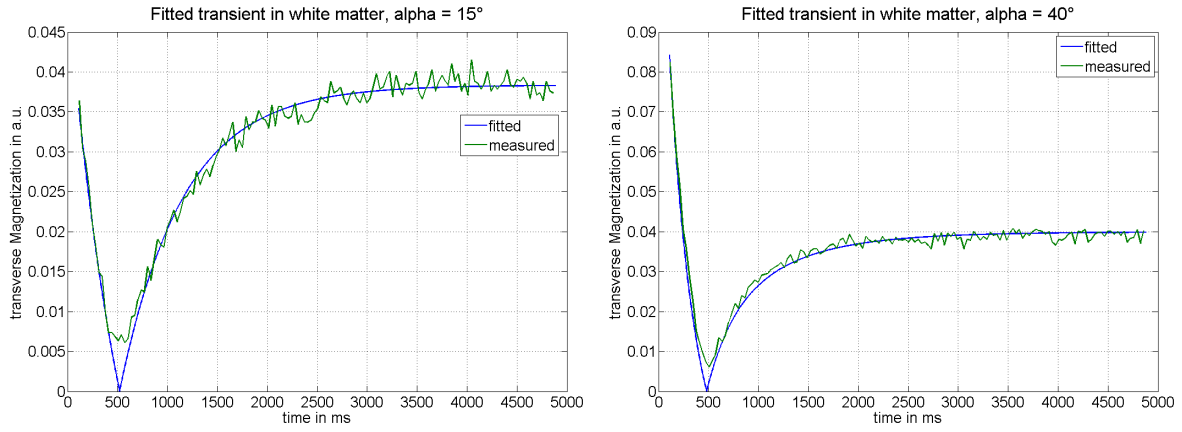

(a) (b)

Figure 4.30: Measured and fitted transient in WM for different nominal flip angles, with the quantified parameters listed in Table 4.8.

		GM		WM	
α_{nom}		Quant. Res.	ΔS_{MT}	Quant. Res.	ΔS_{MT}
15°	T_1	1319ms	1.11	791ms	1.13
	T_2	43.9ms		31.6ms	
20°	T_1	1370ms	1.24	811ms	1.28
	T_2	40.9ms		26.4ms	
30°	T_1	1479ms	1.51	887ms	1.56
	T_2	38.4ms		24.7ms	
40°	T_1	1597ms	1.74	958ms	1.83
	T_2	39.3ms		24.1ms	

Table 4.8: Quantification results in GM and WM for different nominal flip angles using the pixel wise slice profile correction reconstruction algorithm. The attenuation coefficient ΔS_{MT} represents the ratio of the simulated steady state signal with correct relaxation parameters (out of the reference measure) without MT effects and the measured steady state signal. The simulated steady state was simulated with the following parameters. GM: $T_1 = 1600ms$, $T_2 = 125ms$; WM: $T_1 = 900ms$, $T_2 = 85ms$.

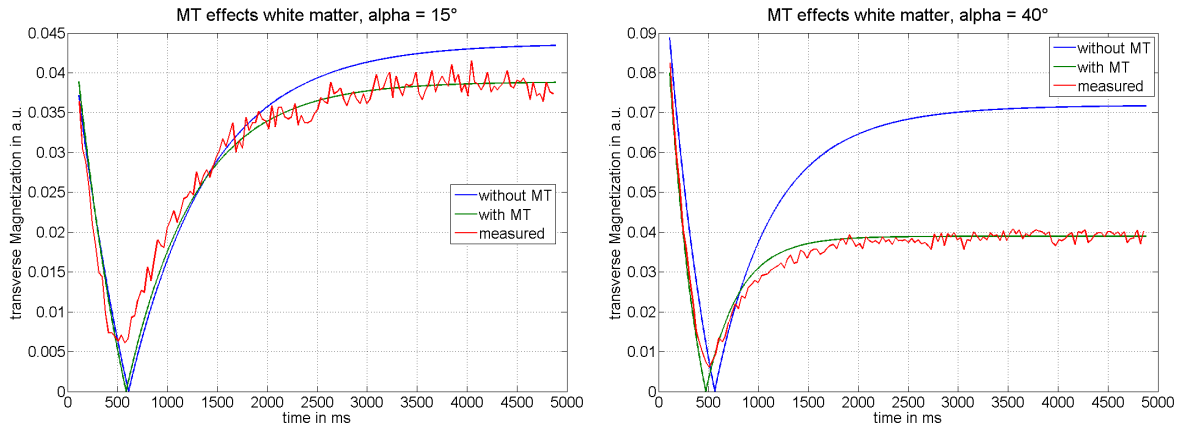

(a) (b)

Figure 4.31: Comparison between the simulated bSSFP transient with true relaxation parameters, the simulated transient including magnetization transfer effects with true relaxation parameters and the measured transient in WM for different nominal flip angles. The true relaxation parameters were determined by the reference measure and the MT parameters were taken from [29]. Parameters used for the simulation: $T_1 = 900ms$, $T_2 = 85ms$, $F = 15\%$, $k_f = 5.1s^{-1}$, $G(0) = 2.8 \cdot 10^{-5}s$ (a) $\alpha_{nom} = 15°$, (b) $\alpha_{nom} = 40°$.

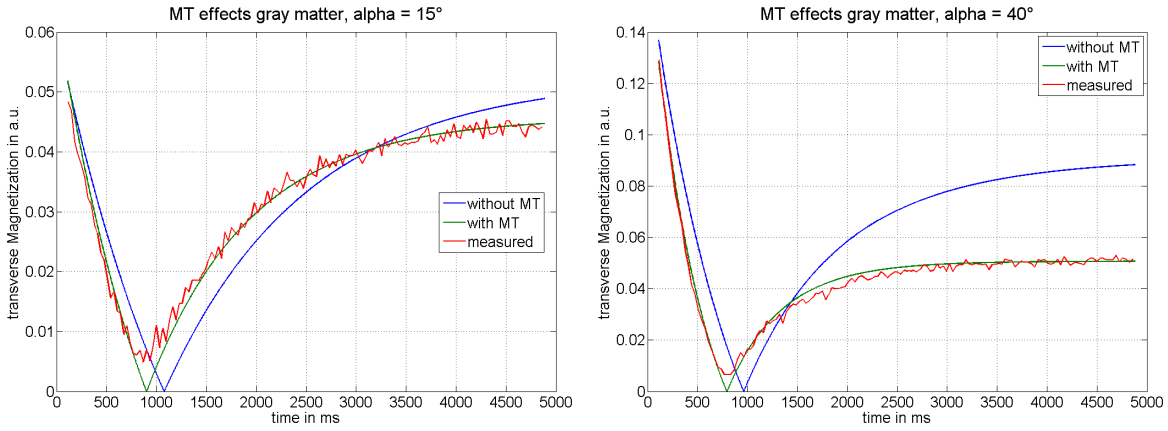

(a) (b)

Figure 4.32: Comparison between the simulated bSSFP transient with true relaxation parameters, the simulated transient including magnetization transfer effects with true relaxation parameters and the measured transient in GM for different nominal flip angles. The true relaxation parameters were determined by the reference measure and the MT parameters were taken from [29]. Parameters used for the simulation: $T_1 = 1600ms$, $T_2 = 125ms$, $F = 7.1\%$, $k_f = 1.9s^{-1}$, $G(0) = 4.0 \cdot 10^{-5}s$ (a) $\alpha_{nom} = 15°$, (b) $\alpha_{nom} = 40°$.

5 Discussion

5.1 Flip Angle Profiles

First of all, the effect of the different RF-excitation pulse types available in the TrueFISP_CV sequence and their influences to the flip angle profile was investigated. In Figure 4.2(a), all available RF-pulse shapes are illustrated. Normally, sinc-shaped RF-pulses are applied to achieve a more or less rectangular shaped slice profile. An ideal slice profile requires an infinite long sinc-shaped pulse, because it has a rectangular spectrum. In practice, a few side-lobes of windowed sinc-functions are used [10, p. 37–43]. The RF-pulse types used in the TrueFISP_CV sequence are far away of this desired sinc-shape, as they are generated by a windowed Gaussian function. All three pulse shapes in 4.2(a) are exactly the same, the only difference is scaling. To achieve the same nominal flip angle, the area under all three RF-pulse shapes is the same (Eq. 3.31). The "Fast"-pulse has a duration of 0.8ms and a maximum amplitude of about 500V. Compared to that, the duration of the "Low-SAR"-pulse is doubled and its maximum amplitude is exactly the half. Because the specific absorption rate (SAR), which is a measure for the RF-energy absorbed in the body, is proportional to the square of the B_1-amplitude [10, p. 33], the SAR can be reduced by the "Low-SAR"-pulse by the factor of four.
According to the "low flip angle approximation" and the fact that all RF-pulse types have the same shapes, no variation in flip angle profile would be expected at least for low flip angles. The Figures 4.2(b), 4.2(c) and 4.2(d) depict the simulated flip angle profiles for all RF-pulse types and different nominal flip angles α_{nom} using discrete Bloch simulations. The resulting flip angle profiles are exactly the same at each nominal flip angel, the only difference is the resulting slice thickness. This effect would be expected also from the Fourier approximation, because the shorter RF-pulse shapes have a higher bandwidth and therefore a wider slice profile. Although the Fourier approximation does not hold for higher flip angles, the general relationship between RF-pulse bandwidth and slice thickness is still the same. These different slice thicknesses are compensated by applying another gradient strength on the scanner. This circumstance (Figure 4.2) shows the independence of the flip angle profile from the applied RF-pulse type.

In Figure 4.1 the flip angle profiles simulated by the Fourier approximation and the discrete Bloch simulation are compared for different nominal flip angles. For $\alpha_{nom} = 30°$ (Figure 4.1(a)), both flip angle profiles are nearly the same. For $\alpha_{nom} = 90°$ (Figure 4.1(b)) the deviation to the Fourier approximation is significant, but the error is still low. At a flip angle of $\alpha_{nom} = 160°$ (Figure 4.1(c)), the shape of the slice profile calculated by the Bloch simulation is completely different to that calculated by the Fourier approximation. The Fourier approximation cannot be applied any more. This shows the importance of an accurate slice profile simulation especially for high flip angles.

The next thing which had to be investigated was the influence of the slice thickness on the flip angle profile. Simulations showed that the shape of the flip angle profile is independent from the applied gradient strength, which is responsible for varying slice thicknesses. Because of the linear relationship between gradient and flip angle profile, a deviation would not be expected. A question that arises is, if there exist other influences on the scanner. To answer this question, different flip angle profiles at different flip angles and different slice thicknesses (5, 8 and 20mm) were measured. In Figure 4.4 the 5mm and the 20mm slice are compared to each other and therefore they are normalized in z-direction. Especially in Figure 4.4(b), there is a slight deviation between the two slice thicknesses noticeable. The flip angle profile with 20mm thickness tends to be asymmetric. This effect can be explained by varying coil sensitivities along the slice. For this huge thickness of 20mm constant coil sensitivities along the slice cannot be assumed any more. Figure 4.3 images the measured intensity profile for different nominal flip angles at 5mm and 20mm slice thickness. If you compare Figure 4.3(c) with 4.3(f), you will see, that the intensity profile tends to become asymmetric with increasing slice thickness. In some channels, asymmetries are also noticeable already at 5mm slice thickness. This effect influences the flip angle profile at a nominal flip angle of 160°much less than the others. This can be explained by the way of reconstructing flip angle profiles at nominal flip angles exceeding 90°. The left and the right peak are normalized to 90° and therefore the influence of coil sensitivities along the slice is corrected at these reference points. Nevertheless, the influence of slice thickness is very small, especially for common used slice thicknesses of about 5mm, and the basic shape seems to be unchanged. Compared to the very rough slice profile resolution used in the reconstruction and the thereby cause deviation, the deviation caused by the slice thickness is negligible. The results for 8mm slice thickness are similar and therefore not presented explicitly.

The last question concerning the flip angle profiles is, how accurate the simulation compared to the slice profiles is in real? The answer is given in Figure 4.5, where the simulated and the measured flip angle profiles for a slice thickness of 5mm are compared for different nominal flip angles. The difference between both profiles is less than that for

different slice thicknesses, but the reason for that might be the same. Figure 4.5 shows that the model of Bloch simulations is very accurate for the calculation of flip angle profiles at a wide range of nominal flip angles. Practically, for the reconstruction and simulation, it does not matter which flip angle profile is used. Using the simulated profile would be a little bit better, because it is not influenced by noise and coil sensitivities.

5.2 Simulation Results

Ideal Conditions: The simulation results in Section 4.2 show that the parameter estimation using the Schmitt-approach works nearly perfect under ideal conditions. For a rectangular flip angle profile and $\alpha/2$ preparation, all three parameters can be estimated nearly without error for a nominal flip angle from 10° to almost 160°, see Figure 4.6 (a),(c),(e). Also different ratios between T_2 and T_1 do not alter the estimation significantly, only if T_2 comes into the range of TR, a slight deviation occurs, because the assumption $TR \ll T_2 < T_1$ is violated (Figure 4.8 (a),(c),(e)). The same result can be achieved for the simulation with a constant ratio of T_2/T_1. Only for very small values of T_1 and T_2, the estimation accuracy decreases (Figure 4.10 (a),(c),(e)). This behaviour is not really surprising, because the equations in Section 2.2 are determined for exactly this case, but with some simplification (see Appendix). The good performance of the method of Schmitt can be confirmed by these simulations for the ideal case. However, the situation looks somewhat different, if the conditions differ from these ideal conditions, like it is always the case for real measurements.

Non-Ideal Flip Angle Profiles: If the flip angle profile differs from the ideal case, the quantification accuracy decreases significantly especially for T_2. This is the case, because the signal is generated by many magnetization vectors with a different flip angle along the slice. The resulting transverse magnetization, which is proportional to the signal, can be seen as the vectorial sum over all magnetization vectors, each with its own transient. Therefore, the resulting transient changes as well and the quantification accuracy decreases. In general, the quantification with a non-ideal flip angle profile tends to underestimate T_1 and to overestimate T_2 . The degree of under- or overestimation increases, the more the flip angle profile deviates from the rectangular shape. In the range of flip angles for practical use of about 30–60°, the underestimation of T_1 is lower than 10% and the overestimation of T_2 lies around 70–100% for the real slice profile (Figure 4.6 (a),(c),(e)). The ratio of T_2/T_1 has also an important influence on the parameter quantification. The quantification error increases with decreasing T_2/T_1 and is most dominant in T_2 (Figure 4.8 (a),(c),(e)). The simulation in Figure 4.8 was done with $T_1 = 1000ms$ and varying T_2. In the physiological range ($T_2 < 100ms$ in many tissues), T_2 is overestimated by around 100% with the real slice profile, which is definitely not accurate enough. The error in

T_1 lies in an acceptable range lower than 5% even at the worst flip angle profile. Only if T_2 gets very low, the error in T_1 increases, but this seems to be a result of violating the assumption $TR \ll T_2 < T_1$. According to Figure 4.10(a),(c),(e), the absolute value of T_1 and T_2 seems to have no influence on the quantification accuracy for all slice profiles. This of course is only the case, if the condition $TR \ll T_2 < T_1$ is satisfied.

Noisy Data: For all investigations so far, the signal was simulated without noise. Now, we would like to consider the influence of noisy data on the parameter quantification. Even for the ideal slice profile, a significant flip angle dependency appears. The quantification of T_1 gets more and more uncertain for increasing flip angles, see increasing standard deviation in Figure 4.7(a). The quantification of T_2 behaves exactly opposite. At low flip angles, the standard deviation of the quantification error increases up to $\pm 80\%$ even for the ideal slice profile. The non-ideal profiles are much worse, the error increases to $\pm$ several times T_2 (Figure 4.7(c)). Out of that, the ideal flip angle can be determined as a trade-off between T_1 and T_2 accuracy and lies somewhere between 40° and 60°. This is in accordance to theory [31] and [16]. Referring to Eq. 2.5, the transient decay rate is mainly influenced by T_1 at low flip angles and by T_2 at high flip angles. To get information of both values, a medium flip angle is needed. Interestingly, the quantification of T_1 using data with non-ideal slice profiles is much more robust against noise at high flip angles than in the ideal case (Figure 4.7(a)). A possible explanation might be that the signal gets very low for high nominal flip angles and due to the varying flip angle over the slice, the resulting signal is much higher than in the ideal case and therefore less sensitive to noise. However, this has no relevance in practice. The determination of T_2 with the same amount of noise and a bad slice profile is nearly impossible. At low flip angles the quantification is highly influenced by noise and at higher flip angles, the systematic error caused by the non-ideal slice profile is dominant (Figure 4.7(c)). A similar situation can be seen for the quantification of T_2 with respect to the relation of T_2/T_1 (Figure 4.9(c)). The sensitivity to noise increases, if the ratio is in the order of one (even for ideal slice profile), but the systematic error due to non-ideal slice profiles increases significantly for low values of T_2/T_1. This increased noise sensitivity can be explained by the fact that the transient depends on the ratio of T_2/T_1 as well. The higher it is, the lower is the influence of T_2 on the transient. If $T_2 > T_1/2$, the transient is nearly independent of T_2. In Figure 4.19 it is shown that the transients for $T_2 = 500ms$, $T_2 = 800ms$ and $T_2 = 900ms$ are nearly the same. The noise sensitivity also increases slightly with decreasing values of T_1 and T_2 (Figure 4.11(c)), but the overall influence is comparatively low over the complete range. The T_2 quantification is influenced most, but the standard deviation is less than $\pm 20\%$ for a simulation with $T_1 > 100ms$ for the rectangular flip angle profile. For non-ideal profiles, the noise sensitivity increases to around $\pm 40\%$ for T_2.

Preparation Method: The influence of the preparation method was investigated, too. Changing the preparation method from $\alpha/2$ to ramp-up preparation influences mainly the quantification of T_1 . The quantification results for T_2 are qualitatively the same as with $\alpha/2$ preparation. Quantitatively the error increases by a few percent in most cases. The quantification of T_1 is influenced much more. Interestingly, the ideal slice profile is influence most, where as the worse slice profiles show a similar behaviour as with $\alpha/2$ preparation. For flip angles of more than 40°, T_1 gets overestimated significantly (Figure 4.6(b)). The same behaviour can be observed for a low ratio of T_2/T_1, where the influence is maximal for the ideal slice profile (Figure 4.8(b)). This behaviour can be explained by the influence of the ratio T_2/T_1 on the transient. In Figure 4.14, the transients of $\alpha/2$ and ramp-up preparation are compared to each other for different values of T_2 and a constant value of T_1. The readout for the ramp-up prepared sequence starts after the preparation, so the ascending part of the transient is not measured. For low values of T_2, the whole transient is shifted to the right, which leads to an overestimation of T_1. A similar behaviour can be simulated for high flip angles as well ($\alpha > 60°$). This shows that the assumption stated in Section 2.2, that the transient is the same for both preparation strategies after preparation has finished, is only an approximation. It is violated for high flip angles and low values of T_2 . For low values of T_1, the quantification accuracy decreases significantly, especially for T_2 (Figure 4.10(d)). The reason for this is simply that the main part of the transient is over before the first readout takes place and the transient cannot be sampled sufficiently long. The noise sensitivity behaves similar to that for the $\alpha/2$ prepared sequence.

Off-Resonances: Figures 4.12 and 4.13 illustrate the influence of off-resonances without noise and a noise level of 10% respectively. Off-resonances are modelled by the off-resonance precession angle ϕ. However, this model is not sufficient enough, because for high off-resonances the varying axis of rotation has to be taken into account. Nevertheless, the tendency can be shown correctly. With increasing off-resonance angle ϕ, T_1 is increasingly overestimated and T_2 gets increasingly underestimated. The ideal slice profile is influenced most in the quantification of T_1. For the quantification of T_2 an interesting situation appears. There is a point where the error due to the bad slice profile and the error due to off-resonance compensate each other and T_2 seems to be quantified correctly. The noise sensitivity is nearly constant over the whole range for both preparation strategies.

Other simulations were performed for varying TR and TI, but the quantification results are not altered significantly. Another interesting fact is that the error in M_0 is qualitatively similar to the error in T_1 in nearly all cases. Under ideal conditions, the rectangular flip angle profile delivers excellent results, but if the conditions get worse, the rectangular slice profile is often more sensitive to that than the non-ideal ones.

5.3 Simulation Results with Slice Profile Correction

The results shown in Figures 4.15 to 4.17 are very promising. Nearly all systematic errors can be corrected except of some exceptions. The achieved results with the measured flip angle profile are very close to that reached with an ideal slice profile using the Schmitt-approach. The estimated parameters get nearly independent of the flip angle α, the ratio T_2/T_1 and the absolute value of T_1. T_1 can be quantified in all cases with an error lower than 1%, and the error in T_2 is less than 5% compared to the real value. The only exception are flip angles lower than 20° (Figure 4.15), where the error in T_2 gets significant. Systematic errors appear as well for decreasing T_2 (Figure 4.16), but the reason for that is not known. Nevertheless, these systematic errors are lower than 3%, they can be neglected and were not investigated further. The quantification algorithm with flip angle profile correction is less sensitive to low values of T_1 and T_2 (in the range of TR), if the ratio T_2/T_1 is constant (Figure 4.17), because the assumption $TR \ll T_2 < T_1$ was not made in the forward model. Especially for $\alpha/2$ preparation, the result is nearly independent of the absolute value of T_1 and T_2. For ramp-up preparation the deviation for low values of T_1 increases a little bit, because of the long preparation time and the poorer sampled transient, but it is still lower than for the Schmitt approach with rectangular slice profile. Furthermore, the parameter estimation seems to be independent of the preparation method, the only exception are low values of T_1.

This excellent quantification results for noiseless measurement data can be reproduced in most cases, if the simulated measurement data are corrupted with 5% Gaussian noise. The mean curve over 1000 repetitions tends to behave similar as the corresponding curve without noise. In general, standard deviation of the quantified parameter lies in an acceptable range of a few percent in T_1 and 10-30% in T_2 and varies linearly with the amount of noise. This is only valid, if the noise level is below a critical value. If this value is exceeded, the algorithm does not converge anymore and the error in T_2 increases exorbitantly. The reason for this is that the minimum of the cost function is not very stable. If the value of T_2 moves too far away from the true value during the minimization, T_2 tends to be infinity. This means that the transient of pure T_1 decay is always a local minimum of the cost function. Therefore, an accurate initial guess is also essential. The critical value is not constant and depends on the investigated parameter. There are three critical regions where the algorithm starts to diverge easily: For low flip angles lower than 30° (Figure 4.15), a ratio T_2/T_1 near one (Figure 4.16) and low values of T_1 (Figure 4.17), but these cases are practically not observed in vivo. The reasons are more or less the same as for the increased noise sensitivity of the Schmitt approach. For low flip angles, the transient mainly depends on T_1 and the quantification of T_2 gets very uncertain. If the noise level is increased to 10%, the critical region is not shifted to higher flip angles

and stays around 30°(Figure A.1(c)). If T_2 is in the range of T_1, the transient behaviour is also dominated by T_1 as it is shown in Figure 4.19. If the noise level is increased to 10%, the algorithm starts to diverge, if T_2 is in the range of 30% of T_1. For low values of T_1 at a constant ratio of T_2/T_1, the noise sensitivity increases, because the transient cannot be sampled sufficiently. This influences mainly the ramp-up prepared sequence due to the longer preparation. At a noise level of 5% the algorithm starts to diverge at $T_1 = 200ms$, for $\alpha/2$ preparation convergence is established also for the lowest T_1 value simulated (Figure 4.17(d)). If the noise level is increased to 10% or the ratio T_2/T_1 is increased from 0.2 to 0.5, the divergence starts at $T_1 = 400ms$ independent of the preparation method (Figures A.2(d) and (d)).

The simulations in Figure 4.18 illustrates that the quantification error due to off-resonances can be reduced with slice profile correction in comparison to the Schmitt approach, at least in T_1. The error in T_2 is nearly unchanged and the noise sensitivity is nearly constant over the simulated range.

5.4 Phantom Measurements

The promising simulation results are in accordance to those achieved by measurements in the agar and the Gd-doped phantoms. In the agar phantom, the ratio between T_2 and T_1 is in a good range and T_1 is sufficiently long, so this phantom is suitable to demonstrate the performance of the reconstruction algorithm. The parameter maps of the agar phantom are shown in Figures 4.20, 4.21 and 4.22. The agar phantom consists of the background matter and two enclosures. According to the reference maps Figures 4.20(a) and 4.21(a), T_1 is slightly lower and the T_2 is much higher inside the enclosure compared to the background matter. The quantification of T_1 performs slightly better with the method of Schmitt, but the results lie in the same range at around 7–8% underestimation compared to the reference measure. The slightly lower T_1 inside the enclosure is also resolved better with Schmitt. The slice profile corrected T_1 map looks completely homogeneous over the imaged cross section. As expected, the T_2 map generated with the method of Schmitt is completely overestimated by more than 90%. With slice profile correction, the error in T_2 decreases in a range of around 5% for $N_{seg} = 8$ and 12–13% for $N_{seg} = 16$ for a flip angle of 60°. The reference spin density map suggests a much higher spin density inside the enclosures, but it can be assumed that this huge increase is due to ringing artifacts as you can see at the boarder of the phantom. The true increase might be lower. This increase cannot be resolved by the M_0 map generated by the method of Schmitt, however, it can be detected by both slice profile corrected reconstruction methods.

One main difference can be recognized by comparing the pixel wise and the k-space based reconstruction algorithms. The pixel wise reconstruction algorithm tends to produce "hot pixel" as it can be seen in the border region of Figures 4.20(c) and 4.21(c) or more prominent in Figures A.3 and A.4 acquired with a flip angle of 40°. This is because each pixel is seen as independent and no information of the neighbours is taken into account. If the transient in one pixel is altered due to noise or partial volume artefacts, the algorithm might not converge in this particular pixel. However, these artefacts have the characteristic of salt and pepper noise and can be filtered out easily using a median filter. Another improvement would be to fit the transient as a kind of weighted average over the neighbourhood, but this would blur the parameter map and decrease the spatial resolution.

In contrast to that, the k-space based reconstruction algorithm is more robust against such outliers, which is an inherent characteristic of the algorithm, although no additional regularization was used. It would be possible to add a regularization term to the cost function as it is done in the original framework of [14] considering the norm of the first derivatives of the image to prefer piecewise constant images. The actual reason for the reconstruction in k-space is not the smoother image, but the ability to reconstruct under-sampled measurement data. As shown in Figures 4.20(f–i), 4.21(f–i) and 4.22(f–i) the achieved results do not differ from those achieved with a full sampled k-space until an under-sampling factor of three. The quantification accuracy stays stable too. For an under-sampling factor of four, back-folding artifacts start to appear. For measurement data acquired with a flip angle of $\alpha = 40°$ (Figures A.3 to A.5) or with a number of segments $N_{seg} = 16$ (Figures A.9 to A.11), the image stays free from artifacts until 3-times under-sampling, but the quantification accuracy decreases significantly. In this case it is very important to choose the right flip angle to improve the T_2 accuracy. The acquisition with $N_{seg} = 16$ 2-times under-sampled would be better as the acquisition with $N_{seg} = 8$ 3-times under-sampled, because the scan time can be reduced by a factor of 4 instead of 3 compared to the full sampled acquisition with $N_{seg} = 8$ with similar quantification accuracy. Unfortunately, these high under-sampling factors of around 10 as described in [14] could not be reached. The reason for that might be the much more complicated forward model compared to that used in [14] for mono exponential T_2 decay. As stated in [14], an improvement might be possible by using a blocked under-sampling scheme. For the results discussed here, an interleaved under-sampling pattern was used. Table 4.3 lists the quantification results for the k-space based reconstruction algorithm for full sampled and 3-times under-sampled k-space data for different numbers of CG iterations in the agar phantom. It can be shown, that the algorithm reaches full convergence after about 200 CG iterations. More iterations do not improve the quantification result significantly, but increase the calculation effort.

The results achieved in the Gd-doped phantoms are also in accordance to theory. The contrast agent decreases T_1 and T_2 with increasing concentration, but the ratio T_2/T_1 is only slightly lower than one. As presented in Section 4.3, the quantification of T_2 gets very uncertain in this region of T_2/T_1. As shown in Table 4.4 and Figure 4.23 the quantification of T_1 works very well with both slice profile correction algorithms, the error is always lower than 3%. The method of Schmitt underestimates the true T_1 value slightly, but the error is lower than 10% in all phantoms. The T_2 values quantified by the method of Schmitt are overestimated partially by more than 100% as it is expected. The T_2 value is higher than the corresponding T_1 value in all cases. The results in T_2 achieved by the pixel wise and the k-space based reconstruction are quiet different, for the different concentrations, as it is depicted in Figure 4.23. The T_2 value in the phantom with the highest concentration of 2mM cannot be quantified accurately with both algorithms, because of the very short value of T_1 and the ratio T_2/T_1 near one. The pixel wise reconstruction results in a T_2 map with a very high standard deviation, the solver converges in each pixel to a completely different value or it does not converge at all. Moreover the k-space based approach converges to a homogeneous T_2 map, but the quantified value is 4.5 times higher than the true value in the 2mM Gd-phantom. T_2 in the phantom with 1mM Gd-concentration cannot be quantified correctly too. The mean value inside the ROI, where outliers were removed, is underestimated by more than 30%. The pixel wise reconstruction tends to produce outliers and the k-space based method divides the phantom into two regions with totally different T_2, which drops down the reliability to a minimum. The results of T_2 for the lower Gd-concentrations (0.5, 0.25 and 0.125mM) achieved by the pixel wise reconstruction are better than expected. According to the simulations, the standard deviation gets very high and the average inside the ROI lies very close to the true value. The results achieved with the k-space based reconstruction algorithm are worse, it seems that the error is averaged over the whole image.

The results achieved with off-resonant excitation are also very similar to the simulated results, as it is presented in Table 4.5. According to simulations, the T_1 values are systematically over- and the T_2 values are systematically underestimated for the method of Schmitt as well as with applied slice profile correction, where the overestimation in T_1 is stronger with the method of Schmitt. But this is not the whole truth, the values in Table 4.5 for the pixel wise reconstruction are stated as mean and standard deviation inside a ROI, which only includes pixels where the algorithm has converged. For off-resonance precession angles of more than 100°, the pixel wise reconstruction algorithm does not tend to converge, which did not appear in simulation. In Figure 4.26 a comparison between the simulated and the measured transient for different off-resonance precession angles is shown. The simulations were performed with the T_1 and T_2 values quantified with on-resonant excitation. The fit performs well until an off-resonance precession angle of about

60°. At 100°, a slight deviation occurs and for higher angles the model does not fit any more. The measured transient performs an overshoot before the steady state is reached, which cannot be modeled by a simple rotation around the z-axis. For these strong off-resonances, the deviation of the flip axis during excitation probably has to be taken into account.

5.5 In Vivo Measurements and Influence of Magnetization Transfer

The results for an in vivo measurement in the brain of a healthy volunteer are depicted in Figure 4.27, 4.28 and 4.29, the corresponding ROI evaluation of all three relevant tissues is listed in Table 4.6. The T_1 values are overestimated in GM and WM by 12–15% with both flip angle correction algorithms, compared to an overestimation of around 20% with the method of Schmitt, which does not correspond to theory or to the on-resonant measurements in phantoms. The T_2 values are underestimated in GM and WM by the method of Schmitt by around 30–40%. However, a massive overestimation would be expected. The T_2 quantification results for both flip angle profile correction algorithms are even worse, the T_2 value is underestimated by more than 70% compared to reference measure. The first assumption was that these results are the effect of some off-resonances due to a bad shim, but this could not be proofed by measurements. In a publication of Bieri and Scheffler [32], it was shown that the steady state signal of the bSSFP sequence in GM and WM is much lower than it would be expected according to theory. They also showed that the reasons for this signal attenuation are on-resonant magnetization transfer effects and that the attenuation is less in GM than in WM. The ratio between the attenuation coefficients in WM to GM ΔS_{tissue} is about 1.06 for the simulated data and 1.05 for measured data in [32]. It was tried to reproduce these results and it turned out that the ratio between the attenuation coefficients in WM and GM is about 1.06 for a flip angle of 40° (Table 4.8), which is in good agreement with [32]. Furthermore, it was shown in [32] that the attenuation coefficient increases with increasing flip angle, which could also be verified by measurements (Table 4.8). The values in [32] cannot be compared directly to ours, because the MT attenuation in [32] was demonstrated by using different values of TR. Our sequence does not allow a manual adjustment of TR, so the attenuation coefficient ΔS_{MT} is determined by comparing the measured value to the theoretical one. This flip angle dependency of the attenuation coefficient can be explained by Eq. 3.52, because the saturation of the bound pool is proportional to the square of ω_1. An argument against the theory of MT as a reason for the wrong parameter quantification in vivo might be, that in agar magnetization transfer appears as well. But it is shown in [32] that for this particular sequence nearly no MT effects are present in agar.

To further verify the theory of magnetization transfer, a simplified model including MT effects for the bSSFP sequence proposed by [30] was implemented to simulate the transient including MT effects. The model parameters are taken from [29]. These simulated transients for GM and WM are illustrated in Figures 4.31 and 4.32, which is in a good agreement with the measured signal. There is only one factor of uncertainty, the $G(0)$ factor describing the absorption line in Eq. 3.53. The problem is that the function has to be evaluated for zero off-resonance frequency, but it has a singularity there. In [30] it is solved by an asymptotic approximation, but if this value is used in simulation, the fit is very poor. Because this value appears in the exponent of an exponential function, it has a strong influence on the resulting transient. To achieve the fits in Figure 4.31 and 4.32 the value of $G(0)$ has to be adapted for the particular tissue. The idea to determine the MT parameters bound pool fraction F and the exchange parameter k_f out of the transient seems to be very difficult, because of the mentioned uncertainty in $G(0)$ and the fact that a very good fit without including MT effects can be established, but with wrong parameters.

However, the performance of both reconstruction algorithms is comparable to that demonstrated in phantoms. The pixel wise reconstruction tends to produce more outliers especially in regions with poor data acquisition like in CSF. For example neither T_1 nor T_2 could be quantified in CSF with the pixel wise reconstruction. The stable regions are too small to give a reasonable value for mean and standard deviation. Especially in M_0, the k-space based reconstruction produces also some outlier artifacts in CSF, but the values of T_1 and T_2 are much more stable. The quantified parameter maps are also in good accordance to each other for both quantification algorithms, which is an indication that no algorithmic reason is responsible for the bad quantification results. The parameter maps do not change significantly until an under-sampling factor of three. For 4-times under-sampling, a huge increase in the T_2 map can be recognized. The reference values in WM are in good accordance to those in literature. In [33], the relaxation times in WM are stated that T_1 is around 790–890ms and T_2 is around 80–85ms depending on the region in the brain and the sex of the volunteer, which is in good accordance to our results of 872 and 87ms, respectively. The reference values in GM vary strongly in literature. In [33], T_1 of around 1300–1400ms and a T_2 of around 100–130ms is stated depending on the examined area. In contrast to that, in [34] relaxation times of $T_1 = 1820 \pm 114$ and $T_2 = 99 \pm 7$ are stated. Our determined reference values lie somewhere in between that with $T_1 = 1628 \pm 207$ and $T_2 = 125 \pm 53$. It seems that there is a strong inter-subject variability, but also the intra-subject variability is very high according to the high standard deviation. A possible reason for that might be partial volume artifacts, because the small region of GM is very close to CSF. Due to the slice thickness of 5mm and the low resolution of 128x128, partial volume artifacts are very likely. Interestingly, the reference measurement in CSF did not work. A value of around 36s is far too high. In [35], a T_1

value in CSF of around 3700ms is stated, which is in very good accordance to the results which were achieved by the k-space based reconstruction algorithm. The reason for this significant error in the reference measure is that a TR of 10s is not long enough to ensure complete relaxation in CSF. The T_2 value in CSF seems to be at least more feasible, although the assumption of complete relaxation is violated, too. To find a reliable value for T_2 in CSF in literature is very challenging and the given values vary in a wide range. In [1, p. 161] it is stated that T_2 in CSF is very long (>1000ms), in [36] T_2 of CSF is modeled with 2000ms, in [13] it is stated to be 190ms, after [12] it is 1523ms $\pm$232 and the publication of [4] says that T_2 in CSF has a value of 2562 $\pm$123. The results in Table 4.7 show the quantified values in the three main tissues of the brain for three different healthy volunteers. A slight inter subject variation can be recognized.

Calculation Performance: Because of the fact that the whole forward model has to be solved for all sub-slices in each iteration step of the optimization algorithm, the calculation effort is very high. In spite of simplifying the forward model as described in Section 3.1.2 and a parallelization on the CPU the reconstruction with the pixel wise algorithm takes around 30–45min for a 64x64 matrix and 3.5 hours for a 128x128 matrix depending on the size of the object in the image. The reconstruction was performed on a hyper-threaded quad core Intel i7 870 CPU with 2.93GHz. The calculation effort increases nearly linear with the number of pixels in the pixel wise case.

The calculation effort for the reconstruction in k-space is even higher. The reconstruction of a 64x64 parameter map takes about one hour on the hyper-threaded quad core Intel i7-870 CPU. The reconstruction time increases disproportionately high with image size, a 128x128 parameter map takes about 8-10 hours on a hyper threaded hexa core Intel i7-3930K CPU with 3.2GHz.

5.6 Conclusion

It could be shown that the slice profile correction leads to a significant improvement in the quantification of especially T_2 and a slight improvement in T_1 using the transient of the bSSFP sequence based on simulated data and measurements in phantoms. Furthermore, it was shown that this correction could be included in a model based reconstruction framework, which allows the quantification by using under-sampled measurement data until a under-sampling factor of three with good accuracy.

The huge error in biological tissue, especially in WM and GM in the human brain, which is even worse than without slice profile correction, could be explained by the signal attenuation caused by the saturation of the bound pool fraction and the following magnetization transfer. This theory could be verified by simulating the transient including the magnetization effects by a model which was developed for the bSSFP sequence under some assumptions, which are justified in our case.

Outlook/Further Work: Further work has to be done to investigate the influence of the magnetization transfer in more detail, and maybe to develop an algorithm which is able to correct these effects. This seems to be very difficult, because the established fit using the wrong parameters without modeling MT-effects achieves very low residuals. One idea might be to perform the measurement with different flip angles to get more information about the MT.

Further investigations are also necessary to speed up the reconstruction. This could be done by investigating the reconstruction algorithm, maybe it is possible to implement it more efficiently. On the other hand a massive improvement could be expected by performing the calculations on the GPU using CUDA or OpenCL.

Bibliography

[1] Tofts P. *Quantitative MRI of the Brain, measuring changes caused by disease*. John Wiley & Sons Ltd, The Atrium, Southern Gate, Chichester, West Sussex PO19 8SQ, England, 2003.

[2] Margaret Cheng HL, Stikov N, Ghugre NR, Wright GA. Practical medical applications of quantitative MR relaxometry. *Journal of Magnetic Resonance Imaging*, 36(4):805–824, 2012.

[3] Gulani V, Schmitt P, Griswold MA, Webb AG, Jakob PM. Towards a single-sequence neurologic magnetic resonance imaging examination: Multiple-contrast images from an IR TrueFISP experiment. *Investigative Radiology*, 39:767–774, 2004.

[4] Schmitt P, Griswold MA, Jakob PM, Kotas M, Gulani V, Flentje M, Haase A. Inversion recovery TrueFISP: Quantification of T1, T2 and spin density. *Magnetic Resonance in Medicine*, 51:661–667, 2004.

[5] Petrovic A, Scheurer E, Yen K, Stollberger R. Improved T2-quantification with slice selective MSE-sequences. In *19th Annual Meeting ISMRM, Montreal*. Proc. Intl. Soc. Mag. Reson. Med., 2011.

[6] Petrovic A, Scheurer E, Stollberger R. Closed-form solution for T2 mapping with non-ideal refocusing of slice selective CPMG sequences. *Magnetic Resonance in Medicine*, 2014.

[7] Scheffler K Hennig J. T1 quantification with inversion recovery TrueFISP. *Magnetic Resonance in Medicine*, 45:720–723, 2001.

[8] Messroghli DR, Radjenovic A, Kozerke S, Higgins DM, Sivananthan MU, Ridgway JP. Modified Look-Locker inversion recovery (MOLLI) for high-resolution T1 mapping of the heart. *Magnetic resonance in medicine*, 52(1):141–146, 2004.

[9] Deoni SC, Peters TM, Rutt BK. High-resolution T1 and T2 mapping of the brain in a clinically acceptable time with DESPOT1 and DESPOT2. *Magnetic resonance in medicine*, 53(1):237–241, 2005.

[10] Bernstein MA, King KF, Zhou XJ. *Handbook of MRI pulse sequences*. Elsevier, 2004.

[11] Newbould RD, Skare ST, Alley MT, E.Gold G, Bammer R. Three-dimensional T1, T2 and proton density mapping with inversion recovery balanced SSFP. *Magnetic Resonance Imaging*, 28:1374–1382, 2010.

[12] Stehning C, Winkelmann S, Dahnke H. Simultaneous T1, T2 and spin density quantification in 5 seconds using inversion recovery SSFP. *Proc. Intl. Soc. Mag. Reson. Med.*, 15:1719, 2007.

[13] Griswold MA, Schmitt P, Speier P, Nittka M, Gulani V, Jakob PM. Real-time undersampled radial IR-TrueFISP for fast quantitative T1, T2 & M0 mapping. *Proc. Intl. Soc. Mag. Reson. Med.*, 11:2661, 2004.

[14] Sumpf TJ, Uecker M, Boretius S, Frahm J. Model-based nonlinear inverse reconstruction for T2 mapping using highly undersampled spin-echo MRI. *Journal of Magnetic Resonance Imaging*, 34(2):420–428, 2011.

[15] Scheffler K Hennig J. Is TrueFISP a gradient-echo or a spin-echo sequence? *Magnetic resonance in medicine*, 49(2):395–397, 2003.

[16] Scheffler K. On the transient phase of balanced SSFP sequences. *Magnetic Resonance in Medicine*, 49:781–783, 2003.

[17] Hennig J, Speck O, Scheffler K. Optimization of signal behavior in the transition to driven equilibrium in steady-state free precession sequences. *Magnetic resonance in medicine*, 48(5):801–809, 2002.

[18] Le Roux P. Simplified model and stabilization of SSFP sequences. *Journal of Magnetic Resonance*, 163(1):23–37, 2003.

[19] Hargreaves BA, Vasanawala SS, Pauly JM, Nishimura DG. Characterization and reduction of the transient response in steady-state MR imaging. *Magnetic Resonance in Medicine*, 46:149–158, 2001.

[20] Haacke E, Brown R, Thompson M, Venkatesan R. *Magnetic Resonance Imaging: Physical Principles and Sequence Design*. Wiley, 1999.

[21] Neumayer B Opriessnig P. Imaging Labor MR: Messung, Auswertung und Spektroskopie. lecture notes for imaging lab, 2010.

[22] Stollberger R. NMR-Blochsche Gleichungen. lecture notes for Bioimaging chapter3, 2010.

[23] Stollberger R Wach P. Imaging of the active B1 field in vivo. *Magnetic Resonance in Medicine*, 35(2):246–251, 1996.

[24] Cooper MA, Nguyen TD, Spincemaille P, Prince MR, Weinsaft JW, Wang Y. Flip angle profile correction for T1 and T2 quantification with look-locker inversion recovery 2D steady-state free precession imaging. *Magnetic Resonance in Medicine*, 68(5):1579–1585, 2012.

[25] Olsson DM Nelson LS. The Nelder-Mead simplex procedure for function minimization. *Technometrics*, 17(1):45–51, 1975.

[26] Uecker M, Hohage T, Block KT, Frahm J. Image reconstruction by regularized nonlinear inversion-joint estimation of coil sensitivities and image content. *Magnetic Resonance in Medicine*, 60(3):674–682, 2008.

[27] Hager WW Zhang H. A new conjugate gradient method with guaranteed descent and an efficient line search. *SIAM Journal on Optimization*, 16(1):170–192, 2005.

[28] Heuser H. Lehrbuch der Analysis, Teil 2. *BG Teubner, Stuttgart*, 6, 1991.

[29] Gloor M. *Magnetization transfer imaging using steady-state free precession MR sequences*. PhD thesis, University of Basel, 2010.

[30] Gloor M, Scheffler K, Bieri O. Quantitative magnetization transfer imaging using balanced SSFP. *Magnetic Resonance in Medicine*, 60(3):691–700, 2008.

[31] Schmitt P, Griswold M, Gulani V, Kotas M, Flentje M, Haase A, Jakob P. IR TrueFISP: Analytical expressions for calculation of T1, T2 and spin density and investigation of off resonance influences. In *Proc. Intl. Soc. Mag. Reson. Med*, volume 11, page 2083, 2004.

[32] Bieri O Scheffler K. On the origin of apparent low tissue signals in balanced SSFP. *Magnetic resonance in medicine*, 56(5):1067–1074, 2006.

[33] Wansapura JP, Holland SK, Dunn RS, Ball WS. NMR relaxation times in the human brain at 3.0 tesla. *Journal of magnetic resonance imaging*, 9(4):531–538, 1999.

[34] Stanisz GJ, Odrobina EE, Pun J, Escaravage M, Graham SJ, Bronskill MJ, Henkelman RM. T1, T2 relaxation and magnetization transfer in tissue at 3T. *Magnetic Resonance in Medicine*, 54(3):507–512, 2005.

[35] Clare S Jezzard P. Rapid T1 mapping using multislice echo planar imaging. *Magnetic resonance in medicine*, 45(4):630–634, 2001.

[36] Whittall KP, MacKay AL, Li DK. Are mono-exponential fits to a few echoes sufficient to determine T2 relaxation for in vivo human brain? *Magnetic resonance in medicine*, 41(6):1255–1257, 1999.

List of Figures

List of Tables

A Appendix

A.1 Derivation of the bSSFP Steady State Signal

As described in Section 3.1 on page 21 the magnetization at time point n can be calculated iteratively by

$$\vec{M}_{n+1} = \mathbf{E}\left({}^{TR}/_{2}\right) \cdot \mathbf{R}_x\left(\alpha\right) \cdot \mathbf{R}_z\left(\pi\right) \cdot \left(\mathbf{E}\left({}^{TR}/_{2}\right) \cdot \vec{M}_n + \vec{e}\right) + \vec{e} \tag{A.1}$$

The terms in Eq. A.1 are described in Section 3.1. If the condition

$$\vec{M}_{n+1} = \vec{M}_n = \vec{M}_{ss} \tag{A.2}$$

holds, the steady state is reached. After combining Eq. A.1 and A.2, the equation of the steady state magnetization can be stated as

$$\vec{M}_{ss} = \left(\mathbf{I} - \mathbf{E}_{TR/2}\mathbf{R}_x\mathbf{R}_z\mathbf{E}_{TR/2}\right)^{-1}\left(\mathbf{E}_{TR/2}\mathbf{R}_x\mathbf{R}_z\vec{e}_{TR/2} + \vec{e}_{TR/2}\right) \tag{A.3}$$

If the matrix operations are carried out and an initial magnetization $\vec{M}_0$ of

$$\vec{M}_0 = \begin{pmatrix} 0 \\ 0 \\ M_0 \end{pmatrix} \tag{A.4}$$

is assumed, a steady state magnetization vector of

$$\vec{M}_{ss} = \begin{pmatrix} 0 \\ -\dfrac{\left(1-E_1\right)\sqrt{E_2}M_0\sin\left(\alpha\right)}{1-E_1E_2-\left(E_1-E_2\right)\cos\left(\alpha\right)} \\ -\dfrac{\left(-1+\sqrt{E_1}\right)M_0\left(1+\sqrt{E_2}E_2+\left(\sqrt{E_1}+E_2\right)\cos\left(\alpha\right)\right)}{1-E_1E_2-\left(E_1-E_2\right)\cos\left(\alpha\right)} \end{pmatrix} \tag{A.5}$$

is calculated. Because of the fact that the transverse magnetization can be calculated using the law of Protagoras, this yields to following equation:

$$M_{ss} = \frac{(1 - E_1)\sqrt{E_2} M_0 \sin(\alpha)}{1 - E_1 E_2 - (E_1 - E_2)\cos(\alpha)} \tag{A.6}$$

If $TR \ll T_2 < T_1$, then $E_{1,2}$ can be simplified using Taylor series expansion to

$$E_{1,2} \approx 1 - \frac{TR}{T_{1,2}} \tag{A.7}$$

Plugging Eq. A.7 into A.6 leads to

$$\begin{aligned} M_{ss} &= M_0 \sin(\alpha) \frac{\frac{TR}{T_1}}{1 - \left(1 - \frac{TR}{T_1}\right)\left(1 - \frac{TR}{T_2}\right) - \left(\frac{TR}{T_2} - \frac{TR}{T_1}\right)\cos(\alpha)} \sqrt{E_2} \qquad \text{(A.8)} \\ &= M_0 \sin(\alpha) \frac{\frac{TR}{T_1}}{\frac{TR}{T_1} + \frac{TR}{T_2} - \underbrace{\frac{TR^2}{T_1 T_2}}_{\approx 0} - \left(\frac{TR}{T_2} - \frac{TR}{T_1}\right)\cos(\alpha)} \sqrt{E_2} \end{aligned}$$

Because of $TR \ll T_2 < T_1$ the term $\frac{TR^2}{T_1 T_2}$ can be neglected and TR can be canceled out of the fraction. The T_2 decay between excitation and readout is also neglected, which leads to

$$M_{ss} \approx M_0 \sin(\alpha) \frac{\frac{1}{T_1}}{\frac{(T_2 - T_1)\cos(\alpha) + T_1 + T_2}{T_1 T_2}} \tag{A.9}$$

After canceling out T_1 and reordering, the simplified steady state equation appears in different forms, Eq. A.10 appears in [4] and Eq. A.11 is written in [10].

$$\begin{aligned} M_{ss} &\approx \frac{M_0 \sin(\alpha)}{\left(\frac{T_1}{T_2} + 1\right) - \cos(\alpha)\left(\frac{T_1}{T_2} - 1\right)} \qquad \text{(A.10)} \\ &= \frac{M_0 \sin(\alpha)}{\left(\frac{T_1}{T_2}\right)(1 - \cos(\alpha)) + (1 + \cos(\alpha))} \qquad \text{(A.11)} \end{aligned}$$

A.2 Deviation of the "Schmitt Approach"

In this section, the formulas and approaches of [16] and [4] are summarized and the important formulas are derived. The derivation starts in [16], where matrix notation is used to describe the transient of the magnetization vector after $\alpha/2$ preparation. For this derivation, zero off-resonance and exact alignment of the magnetization vector along

the $\alpha/2$ cone is assumed. As shown in Figure 2.3 during the first RF-pulses a slight deviation from the $\alpha/2$ cone occurs because of relaxation effects (especially for short relaxation times). If the condition $TR \ll T_2 < T_2$ is satisfied, the deviation of the $\alpha/2$ cone is very small and can be neglected. In [16], only the transient component $\vec{Q}(j)$ of the magnetization is considered where M_{ss} is the steady state magnetization derived in A.5.

$$\vec{Q}(j) = \vec{M}(j) - \vec{M}_{ss} \tag{A.12}$$

"Because of the perfect alignment to the $\alpha/2$ cone, each magnetization vector produced at TE after an excitation pulse is a copy of the previous magnetization at TE, but of reduced magnitude. If $\mathbf{T}$ is the transition matrix between two successive magnetization vectors at TE, the corresponding magnetizations are eigenvectors of $\mathbf{T}$."(from [16]).

$$\mathbf{T} \cdot \vec{Q}(j) = \lambda \vec{Q}(j) \tag{A.13}$$

The transition Matrix $\mathbf{T}$ consists of rotation and relaxation matrices. This formulation differs a little bit (order of rotations and flip axis of excitation pulse) to the forward simulation in this thesis, but the transient time course is not effected by that. The rotation and relaxation matrices are the same.

$$\mathbf{T} = \mathbf{E}_{TR/2}\mathbf{R}_z(\pi)\mathbf{R}_y(\alpha)\mathbf{E}_{TR/2} \tag{A.14}$$

Because of the excitation around the y-axis, the y-component of the magnetization is always zero and Eq. A.13 can be written as follows:

$$\begin{pmatrix} -E_2\cos(\alpha) & \sqrt{E_1E_2}\sin(\alpha) \\ \sqrt{E_1E_2}\sin(\alpha) & E_1\cos(\alpha) \end{pmatrix} \begin{pmatrix} Q_x \\ Q_y \end{pmatrix} = \lambda \begin{pmatrix} Q_x \\ Q_y \end{pmatrix} \tag{A.15}$$

After performing an eigenvalue decomposition, the positive eigenvalue can be calculated by:

$$\lambda_1 = \cos(\alpha)(E_1 - E_2) + \frac{1}{2}\sqrt{\cos^2(\alpha)(E_1 - E_2)^2 + 4E_1E_2} \tag{A.16}$$

Eq. A.16 can be simplified using $\cos^2(\alpha)(E_1 - E_2)^2 \ll 4E_1E_2$ and $E_1 \approx E_2 \approx 1$ under physiological conditions and assuming $TR \ll T_2 < T_1$ leads to:

$$\lambda_1 \approx \cos(\alpha)(E_1 - E_2) + 1 \tag{A.17}$$

Furthermore, using $\cos(\alpha) = \cos^2\left(\frac{\alpha}{2}\right) - \sin^2\left(\frac{\alpha}{2}\right)$ and again $E_1 \approx E_2 \approx 1$ and plugging into Eq. A.17 leads to:

$$\begin{aligned} \lambda_1 &\approx \left(\cos^2\left(\frac{\alpha}{2}\right) - \sin^2\left(\frac{\alpha}{2}\right)\right)(E_1 - E_2) + 1 \\ &= E_1 \cos^2\left(\frac{\alpha}{2}\right) + E_2 \sin^2\left(\frac{\alpha}{2}\right) \underbrace{-E_2 \cos^2\left(\frac{\alpha}{2}\right) - E_1 \sin^2\left(\frac{\alpha}{2}\right)}_{\approx -1} + 1 \end{aligned} \tag{A.18}$$

The positive eigenvalue can be seen as decay rate E_1^* with the time constant T_1^* and can be calculated as denoted in Eq. A.19.

$$E_1^* = \lambda_1 = E_1 \cos^2\left(\frac{\alpha}{2}\right) + E_2 \sin^2\left(\frac{\alpha}{2}\right) \tag{A.19}$$

The magnetization can be described using the derivation above,

$$\vec{M}(j) = \left(\sin\left(\frac{\alpha}{2}\right)\vec{M}_0 - \vec{M}_{ss}\right)(E_1^*)^j + \vec{M}_{ss} \tag{A.20}$$

$$(E_1^*)^j = e^{-\frac{j \cdot TR}{T_1^*}} \tag{A.21}$$

In [4], Eq. A.19 is used to derive an equation for the relation between the time constant for the transient T_1^* and the relaxation time constants T_1 and T_2. Again the assumption $TR \ll T_2 < T_1$ and the Taylor series expansion $E_{1,2} \approx 1 - \frac{TR}{T_{1,2}}$, $E_1^* \approx 1 - \frac{TR}{T_1^*}$ is used.

$$1 - \frac{TR}{T_1^*} = \left(1 - \frac{TR}{T_1}\right)\cos^2\left(\frac{\alpha}{2}\right) + \left(1 - \frac{TR}{T_2}\right)\sin^2\left(\frac{\alpha}{2}\right) \tag{A.22}$$

$$1 - \frac{TR}{T_1^*} = \underbrace{\cos^2\left(\frac{\alpha}{2}\right) + \sin^2\left(\frac{\alpha}{2}\right)}_{\approx 1} - \frac{TR}{T_1}\cos^2\left(\frac{\alpha}{2}\right) - \frac{TR}{T_2}\sin^2\left(\frac{\alpha}{2}\right) \tag{A.23}$$

$$T_1^* = \left(\frac{1}{T_1}\cos^2\left(\frac{\alpha}{2}\right) + \frac{1}{T_2}\sin^2\left(\frac{\alpha}{2}\right)\right)^{-1} \tag{A.24}$$

As described in [4], the transient of the bSSFP sequence can be modeled by an three parameter mono-exponential function (Eq. A.25).

$$S(t) = S_{ss}\left(1 - INV \cdot e^{-\frac{t}{T_1^*}}\right) \tag{A.25}$$

The parameter INV can be determined using the limit operation to the signal model for $t \to 0$. For the limit $t \to \infty$ the exponential term vanishes and only the steady state signal S_{ss} remains.

$$\lim_{t \to 0} S(t) = S_{ss}(1 - INV) \tag{A.26}$$

$$INV = 1 - \frac{S_0}{S_{ss}} \tag{A.27}$$

Because of $\alpha/2$ preparation and neglecting the T_1 relaxation between the inversion an the preparation pulse, the signal at time point zero S_0 can be calculated by

$$S_0 = -M_0 \sin\left(\frac{\alpha}{2}\right) \tag{A.28}$$

Using Eq. A.28 and the simplified equation for the steady state signal derived above (Eq. A.10), the INV parameter can be rewritten to:

$$INV = 1 + \frac{\sin\left(\frac{\alpha}{2}\right)}{\sin(\alpha)}\left[\left(\frac{T_1}{T_2}+1\right) - \cos(\alpha)\left(\frac{T_1}{T_2}-1\right)\right] \tag{A.29}$$

Eq. A.29 can be used to derive the ratio between T_1 and T_2 which is needed later.

$$\frac{T_1}{T_2} = \frac{(INV-1)\dfrac{\sin(\alpha)}{\sin\left(\frac{\alpha}{2}\right)} - 1 - \cos(\alpha)}{1-\cos(\alpha)} \tag{A.30}$$

Eq. A.24 is used to derive an equation for T_1 and T_2.

$$T_1 = T_1^*\left(\cos^2\left(\frac{\alpha}{2}\right) + \frac{T_1}{T_2}\sin^2\left(\frac{\alpha}{2}\right)\right) \tag{A.31}$$

$$T_2 = T_1^*\left(\frac{T_2}{T_1}\cos^2\left(\frac{\alpha}{2}\right) + \sin^2\left(\frac{\alpha}{2}\right)\right) \tag{A.32}$$

Using Eq. A.30 and splitting the ratio T_1 to T_2 up into Eq. A.33, where A and B are given in Eq. A.34 and A.35 respectively. T_1 and T_2 can be calculated by Eq. A.36 and A.37 using only parameters fitted by Eq. A.25.

$$\frac{T_1}{T_2} = (A \cdot INV + B) \tag{A.33}$$

$$A = 2\left(1-\cos(\alpha)\right)^{-1}\cos\left(\frac{\alpha}{2}\right) \tag{A.34}$$

$$B = \left(1+2\cos\left(\frac{\alpha}{2}\right)+\cos(\alpha)\right) - \left(\cos(\alpha)-1\right)^{-1} \tag{A.35}$$

$$T_1 = T_1^*\left(\cos^2\left(\frac{\alpha}{2}\right) + (A\cdot INV + B)\sin^2\left(\frac{\alpha}{2}\right)\right) \tag{A.36}$$

$$T_2 = T_1^*\left(\sin^2\left(\frac{\alpha}{2}\right) + (A\cdot INV + B)^{-1}\cos^2\left(\frac{\alpha}{2}\right)\right) \tag{A.37}$$

Using Eq. A.28 and A.27 leads to

$$M_0 = \frac{S_{ss}\,(INV-1)}{\sin\left(\frac{\alpha}{2}\right)} \tag{A.38}$$

A.3 Gradient Expressions

In this section, the complete expressions for the derivatives of $\vec{M}\left(j, \vec{T}\right)$ with respect to T_1, T_2 and M_0 are denoted, which are calculated according to Eq. 3.30.

$$\frac{\partial M_{y,j+1}}{\partial T_1} = - E_2 \cos(\alpha_j) \frac{\partial M_{y,j}}{\partial T_1} - \sqrt{E_1 E_2} \left(\frac{\partial M_{z,j}}{\partial T_1} + \frac{TR}{2T_1^2} \left(-M_{z,j} + M_0 \right) \right) \sin(\alpha_j) \tag{A.39}$$

$$\begin{aligned} \frac{\partial M_{y,j+1}}{\partial T_2} =& E_2 \left(M_{y,j} \frac{TR}{T_2^2} - \frac{\partial M_{y,j}}{\partial T_2} \right) \cos(\alpha_j) + \\ & \left[M_0 \frac{TR}{2T_2^2} \left(\sqrt{E_1 E_2} - \sqrt{E_2} \right) + \sqrt{E_1 E_2} \left(- \frac{\partial M_{z,j}}{\partial T_2} + M_{z,j} \frac{TR}{2T_2^2} \right) \right] \sin(\alpha_j) \end{aligned} \tag{A.40}$$

$$\frac{\partial M_{y,j+1}}{\partial M_0} = - E_2 \cos(\alpha_j) \frac{\partial M_{y,j}}{\partial M_0} + \left(\sqrt{E_1 E_2} - \sqrt{E_2} - \sqrt{E_1 E_2} \frac{\partial M_{z,j}}{\partial M_0} \right) \sin(\alpha_j) \tag{A.41}$$

$$\begin{aligned} \frac{\partial M_{z,j+1}}{\partial T_1} =& \sqrt{E_1} M_0 \frac{TR}{2T_1^2} + \left(\left(-\frac{\sqrt{E_1}}{2} + E_1 \right) M_0 \frac{TR}{T_1^2} - E_1 \left(M_{z,j} \frac{TR}{T_1^2} - \frac{\partial M_{z,j}}{\partial T_1} \right) \right) \\ & \cdot \cos(\alpha_j) + \sqrt{E_1 E_2} \left(M_{y,j} \frac{TR}{2T_1^2} - \frac{\partial M_{y,j}}{\partial T_1} \right) \sin(\alpha_j) \end{aligned} \tag{A.42}$$

$$\frac{\partial M_{z,j+1}}{\partial T_2} = E_1 \frac{\partial M_{z,j}}{\partial T_2} \cos(\alpha_j) - \sqrt{E_1 E_2} \left(M_{y,j} \frac{TR}{2T_2^2} + \frac{\partial M_{y,j}}{\partial T_2} \right) \sin(\alpha_j) \tag{A.43}$$

$$\frac{\partial M_{z,j+1}}{\partial M_0} = \left(1 - \sqrt{E_1} \right) + \left(\sqrt{E_1} - E_1 + E_1 \frac{\partial M_{z,j}}{\partial M_0} \right) \cos(\alpha_j) - \sqrt{E_1 E_2} \frac{\partial M_{y,j}}{\partial M_0} \sin(\alpha_j) \tag{A.44}$$

A.4 Further Results

This section shows some further results, which are not essentially necessary to understand this thesis.

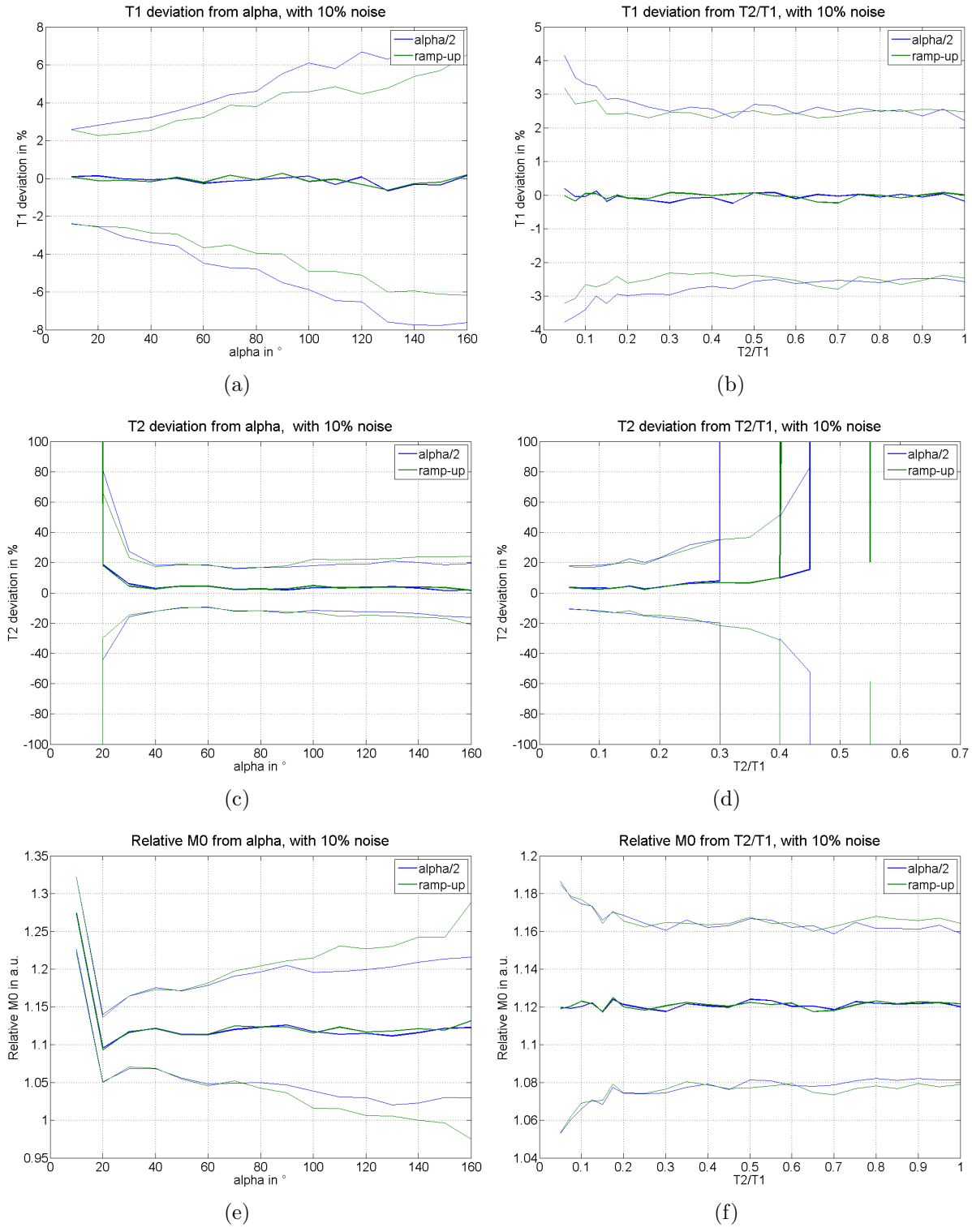

Figure A.1: The influence on the parameter estimation with flip angle profile correction for 10% white Gaussian noise is illustrated for ramp-up and $\alpha/2$ preparation based on simulated data. T_1 and T_2 are shown as the deviation of the real value in % and the value of M_0 is normalized one. The results are shown as mean and standard deviation over 1000 repetitions. (a), (c), (d) variation of flip angle α (b), (d), (e) variation of the ratio T_1/T_2.

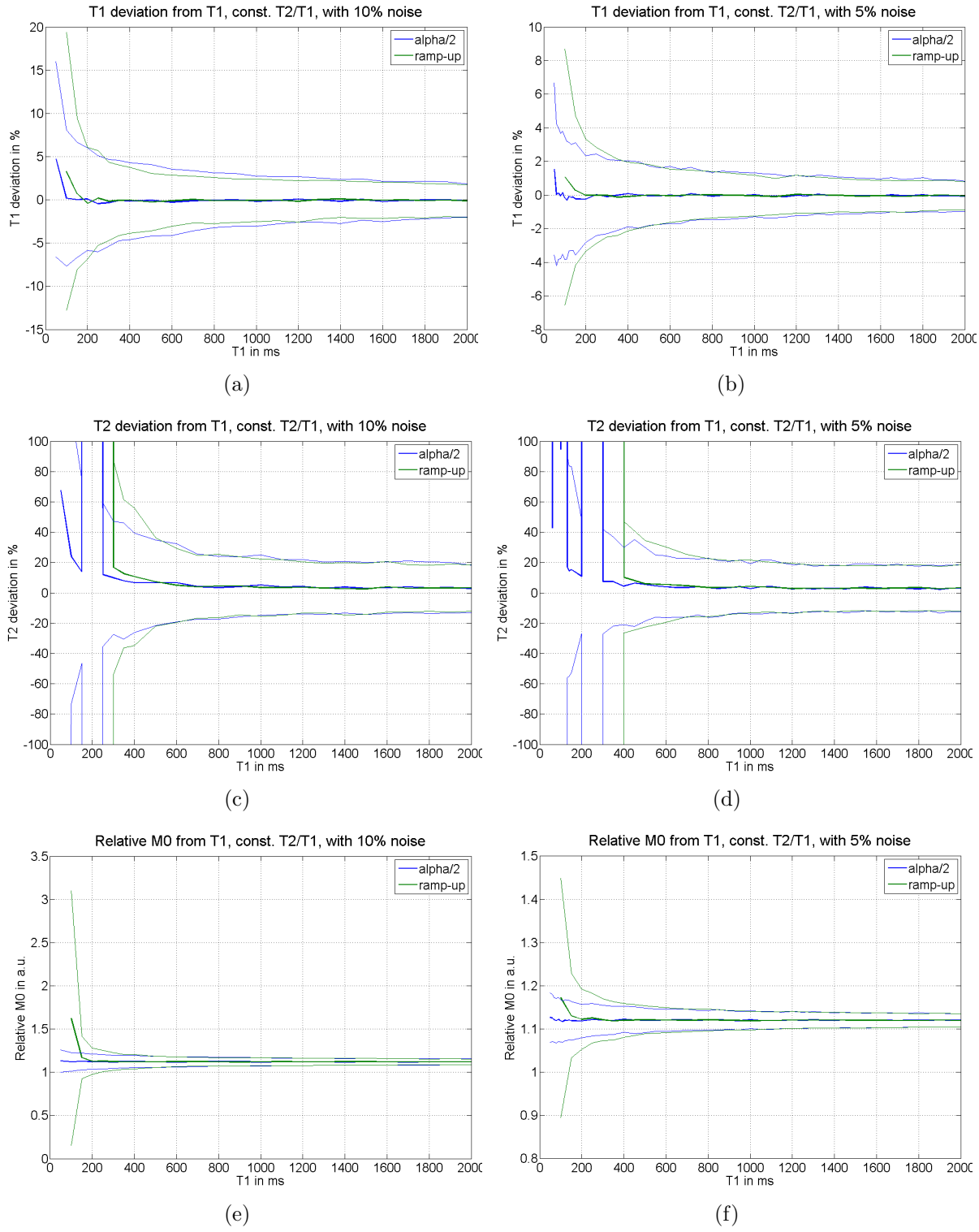

Figure A.2: The influence on the parameter estimation with flip angle profile correction for different values of T_1 is illustrated for ramp-up and $\alpha/2$ preparation based on simulated data. T_1 and T_2 are shown as the deviation of the real value in % and the value of M_0 is normalized one. The results are shown as mean and standard deviation over 1000 repetitions. (a), (c), (d) 10% white Gaussian noise and a ratio of $T_1/T_2 = 0.2$ (b), (d), (e) 5% white Gaussian noise and a ratio of $T_1/T_2 = 0.5$.

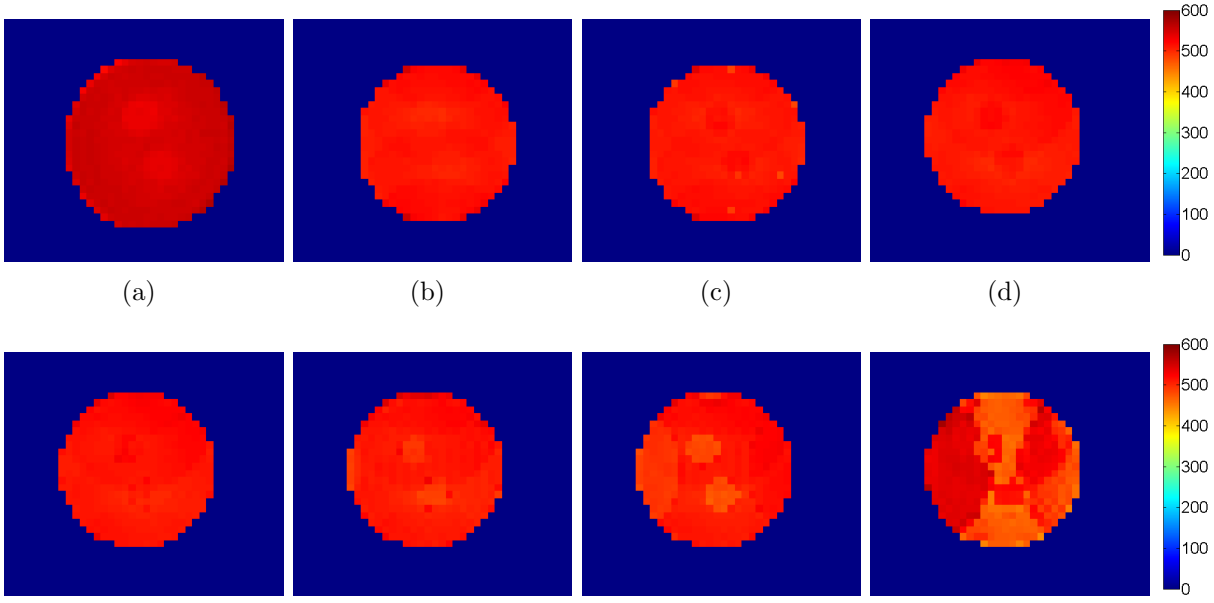

Figure A.3: T_1 maps in the agar phantom generated with different methods for an acquisition with $N_{seg} = 8$ and $\alpha = 40°$. The values are displayed in ms. (a) Reference, (b) Schmitt-approach, (c) pixel wise reconstruction, (d) reconstruction in k-space with full-sampled data, (f) 2-times under-sampled data, (g) 3-times under-sampled data, (h) 4-times under-sampled data, (i) 5-times under-sampled data.

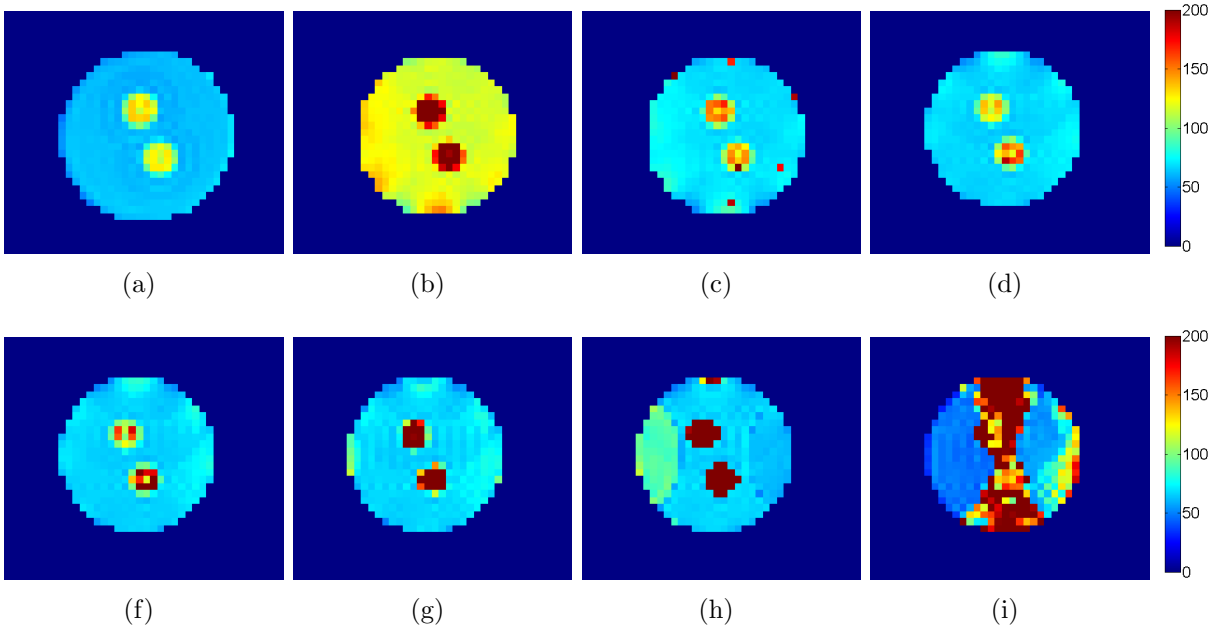

Figure A.4: T_2 maps in the agar phantom generated with different methods for an acquisition with $N_{seg} = 8$ and $\alpha = 40°$. The values are displayed in ms. (a) Reference, (b) Schmitt-approach, (c) pixel wise reconstruction, (d) reconstruction in k-space with full-sampled data, (f) 2-times under-sampled data, (g) 3-times under-sampled data, (h) 4-times under-sampled data, (i) 5-times under-sampled data.

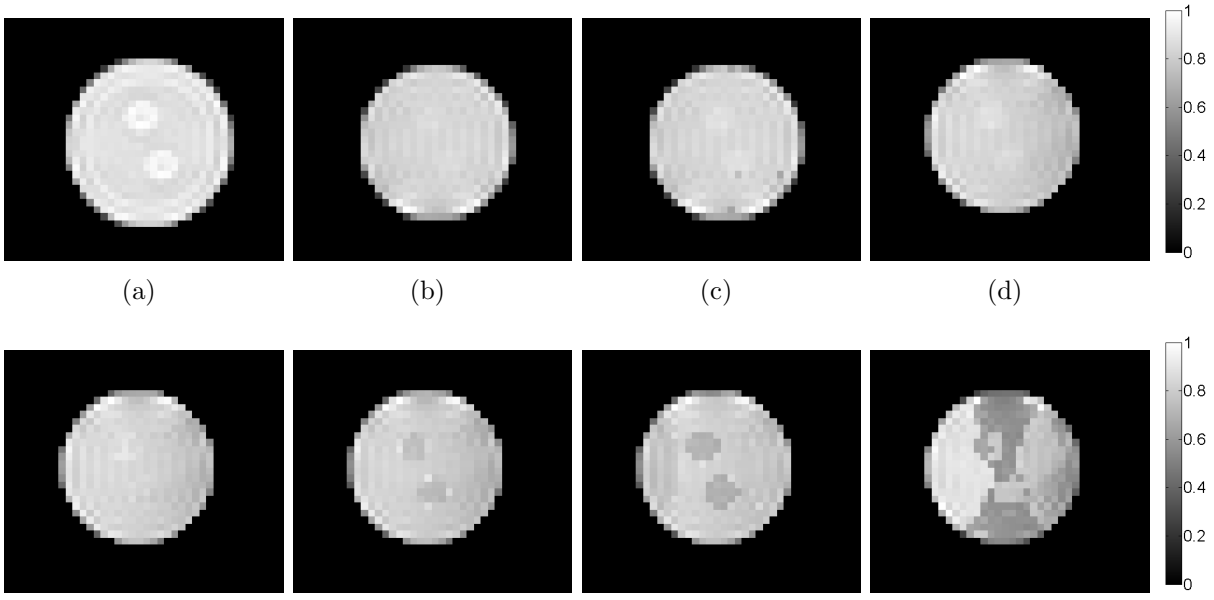

Figure A.5: M_0 maps in the agar phantom generated with different methods for an acquisition with $N_{seg} = 8$ and $\alpha = 40°$. The values are displayed in ms. (a) Reference, (b) Schmitt-approach, (c) pixel wise reconstruction, (d) reconstruction in k-space with full-sampled data, (f) 2-times under-sampled data, (g) 3-times under-sampled data, (h) 4-times under-sampled data, (i) 5-times under-sampled data.

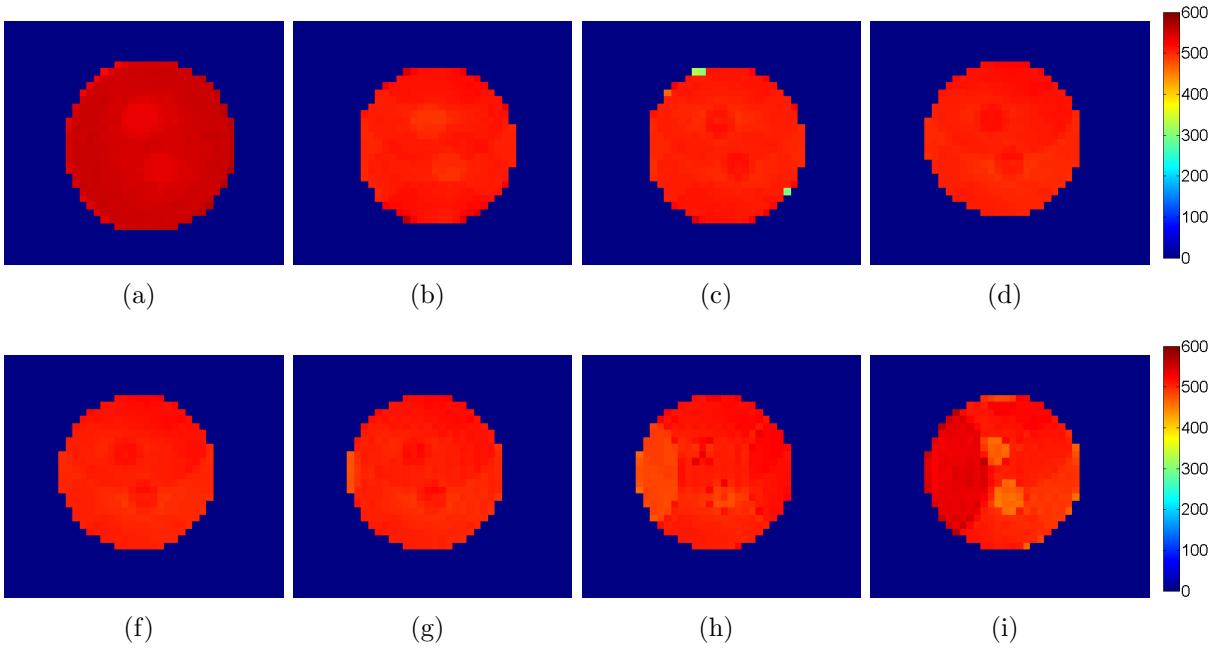

Figure A.6: T_1 maps in the agar phantom generated with different methods for an acquisition with $N_{seg} = 8$ and $\alpha = 50°$. The values are displayed in ms. (a) Reference, (b) Schmitt-approach, (c) pixel wise reconstruction, (d) reconstruction in k-space with full-sampled data, (f) 2-times under-sampled data, (g) 3-times under-sampled data, (h) 4-times under-sampled data, (i) 5-times under-sampled data.

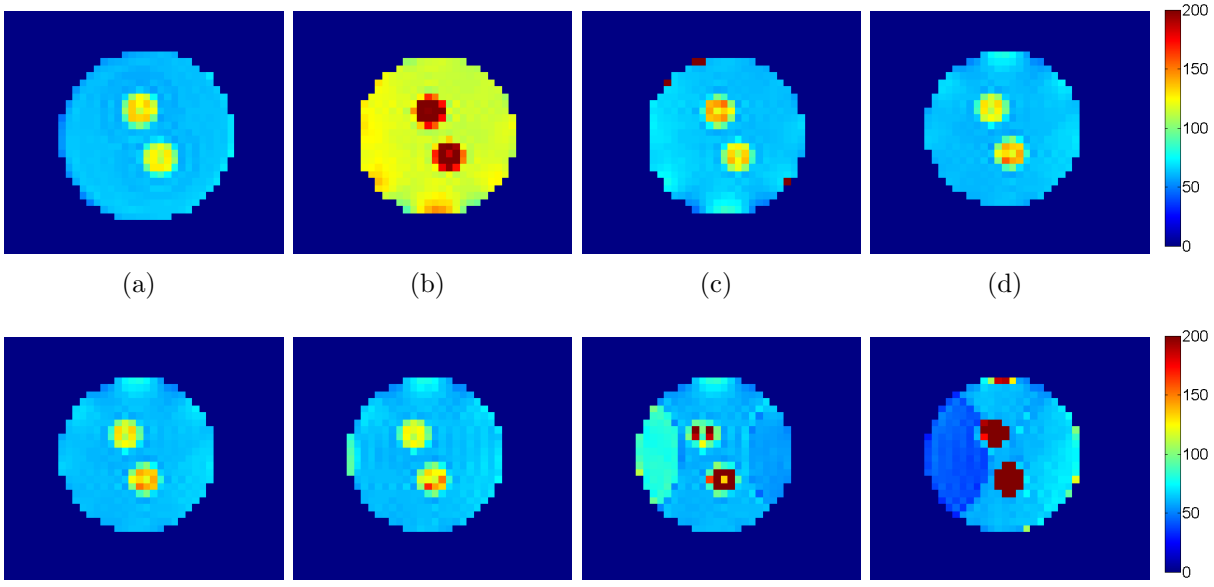

Figure A.7: T_2 maps in the agar phantom generated with different methods for an acquisition with $N_{seg} = 8$ and $\alpha = 50°$. The values are displayed in ms. (a) Reference, (b) Schmitt-approach, (c) pixel wise reconstruction, (d) reconstruction in k-space with full-sampled data, (f) 2-times under-sampled data, (g) 3-times under-sampled data, (h) 4-times under-sampled data, (i) 5-times under-sampled data.

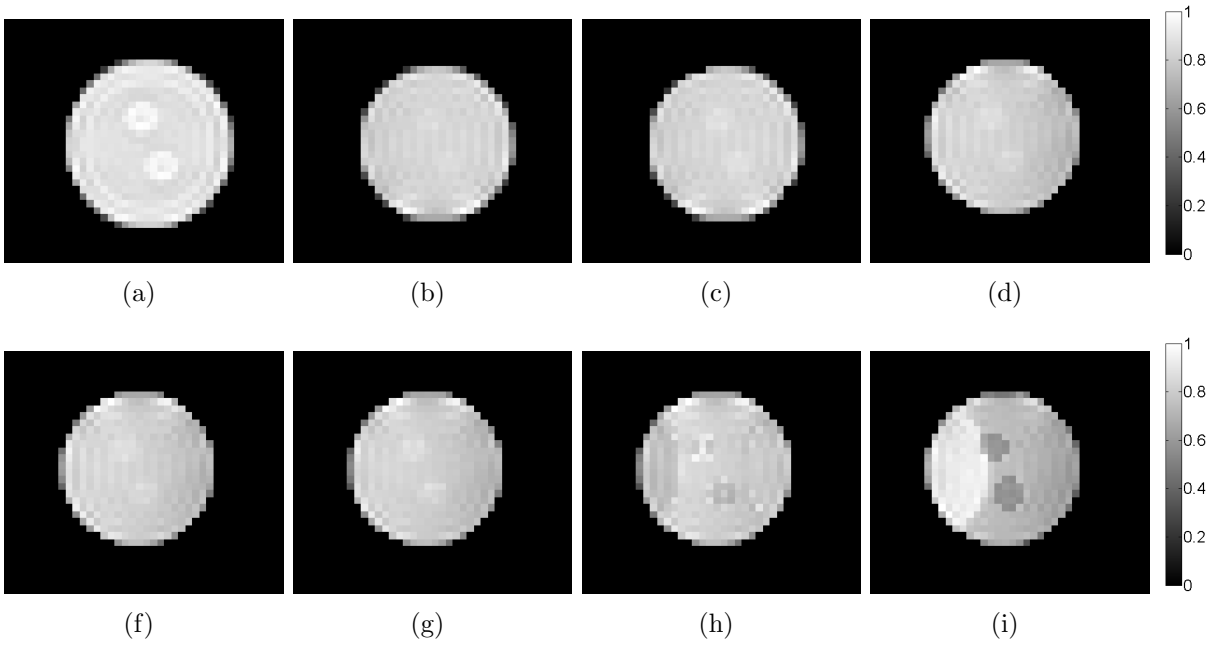

Figure A.8: M_0 maps in the agar phantom generated with different methods for an acquisition with $N_{seg} = 8$ and $\alpha = 50°$. The values are displayed in ms. (a) Reference, (b) Schmitt-approach, (c) pixel wise reconstruction, (d) reconstruction in k-space with full-sampled data, (f) 2-times under-sampled data, (g) 3-times under-sampled data, (h) 4-times under-sampled data, (i) 5-times under-sampled data.

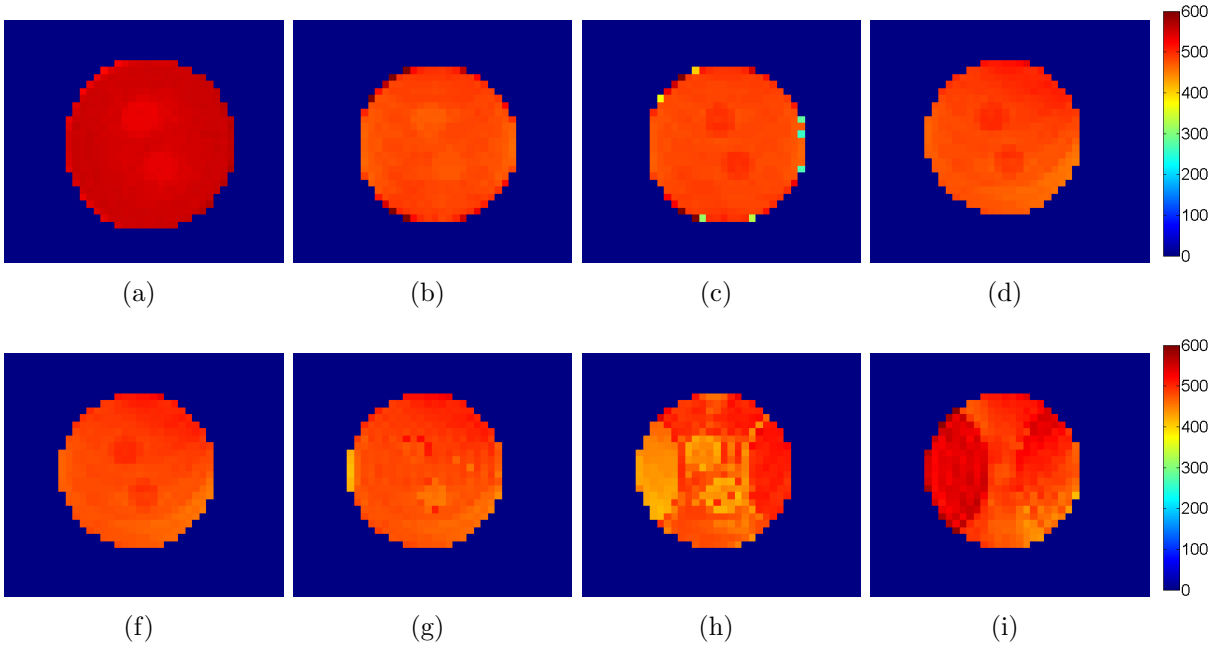

Figure A.9: T_1 maps in the agar phantom generated with different methods for an acquisition with $N_{seg} = 16$ and $\alpha = 60°$. The values are displayed in ms. (a) Reference, (b) Schmitt-approach, (c) pixel wise reconstruction, (d) reconstruction in k-space with full-sampled data, (f) 2-times under-sampled data, (g) 3-times under-sampled data, (h) 4-times under-sampled data, (i) 5-times under-sampled data.

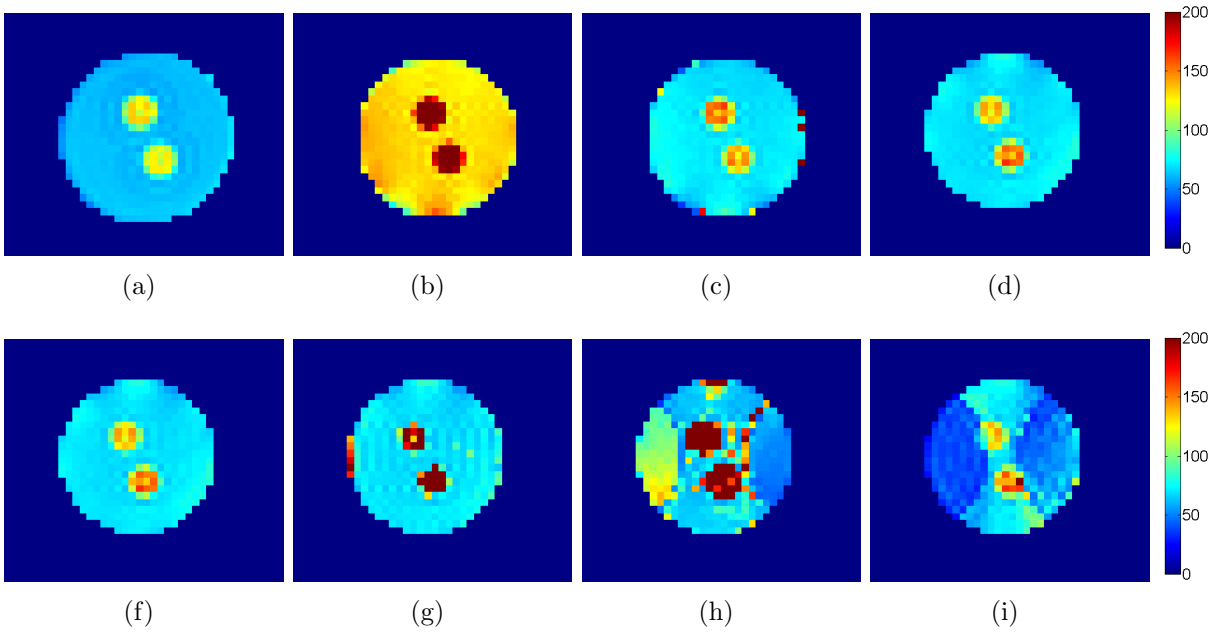

Figure A.10: T_2 maps in the agar phantom generated with different methods for an acquisition with $N_{seg} = 16$ and $\alpha = 60°$. The values are displayed in ms. (a) Reference, (b) Schmitt-approach, (c) pixel wise reconstruction, (d) reconstruction in k-space with full-sampled data, (f) 2-times under-sampled data, (g) 3-times under-sampled data, (h) 4-times under-sampled data, (i) 5-times under-sampled data.

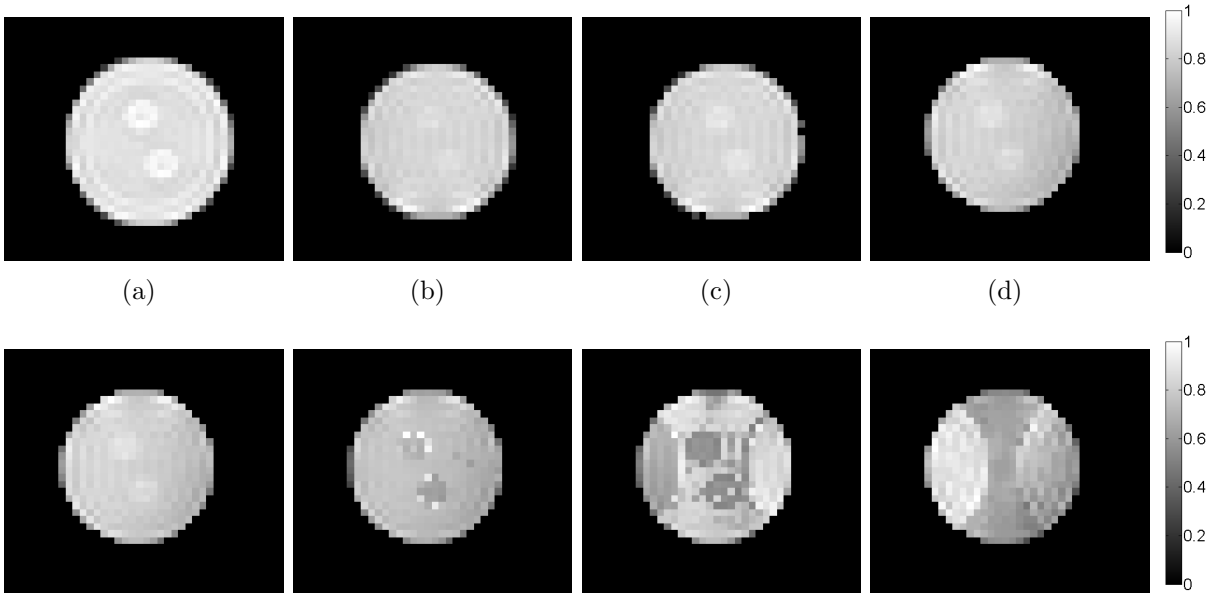

Figure A.11: M_0 maps in the agar phantom generated with different methods for an acquisition with $N_{seg} = 16$ and $\alpha = 60°$. The values are displayed in ms. (a) Reference, (b) Schmitt-approach, (c) pixel wise reconstruction, (d) reconstruction in k-space with full-sampled data, (f) 2-times under-sampled data, (g) 3-times under-sampled data, (h) 4-times under-sampled data, (i) 5-times under-sampled data.